Doctoral dissertation (Shinshu University)

Molecular Engineering of Nanostructured Organic Semiconductors for Organic Solar Cells

-March 2015-

Keisuke TAKEMOTO

Table of contents

Chapter 1

General Introduction

1-1 Inorganic Semiconductors

Inorganic semiconductors such as silicon (Si), germanium (Ge), and gallium arsenide (GaAs) are dominant materials in semiconductor electronics. Amorphous silicon (a-Si) has been widely adopted in transistor and solar cells. Polycrystalline silicon semiconductors exhibit excellent carrier mobility (over 50 $cm^2/ V^{-1} s^{-1}$).[1] Silicon based inorganic semiconductors consist of Si with a small amount of phosphorous or boron. Small quantities of P or B generate the excess electrons or holes required for charge carrier transportation (Figure 1).

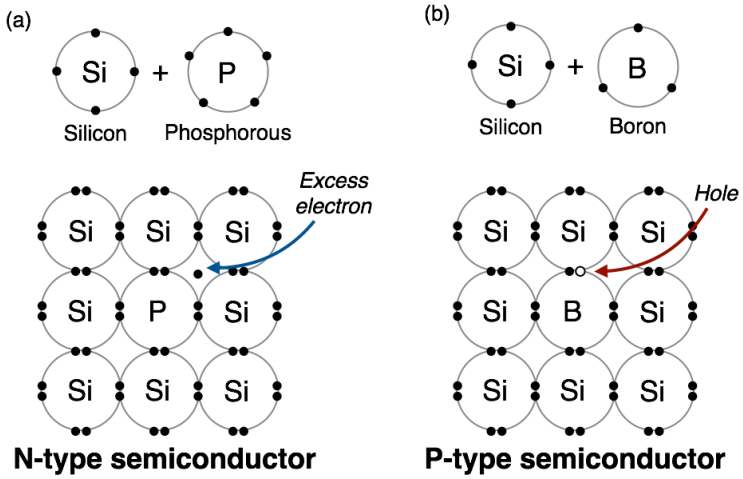

Figure 1. Two-dimensional silicon crystal structure of n-type (a) and p-type (b) semiconductors.

Silicon solar cells were first developed at the Bell Laboratory in the 1950s.[2] When light strikes semiconductor interfaces doped with n- or p-type impurities, charge separation can occur. Over the years, the efficiency of single crystalline Si solar cells has increased by more than 25% (Figure 2).[3] Besides improvement of the

device structures, the materials of inorganic solar cells from single crystalline to polycrystalline have been widely investigated. However, the large production costs of Si-based solar cells are still problematic. Therefore, next-generation materials and devices developed at a low cost with sustainable technology are required.

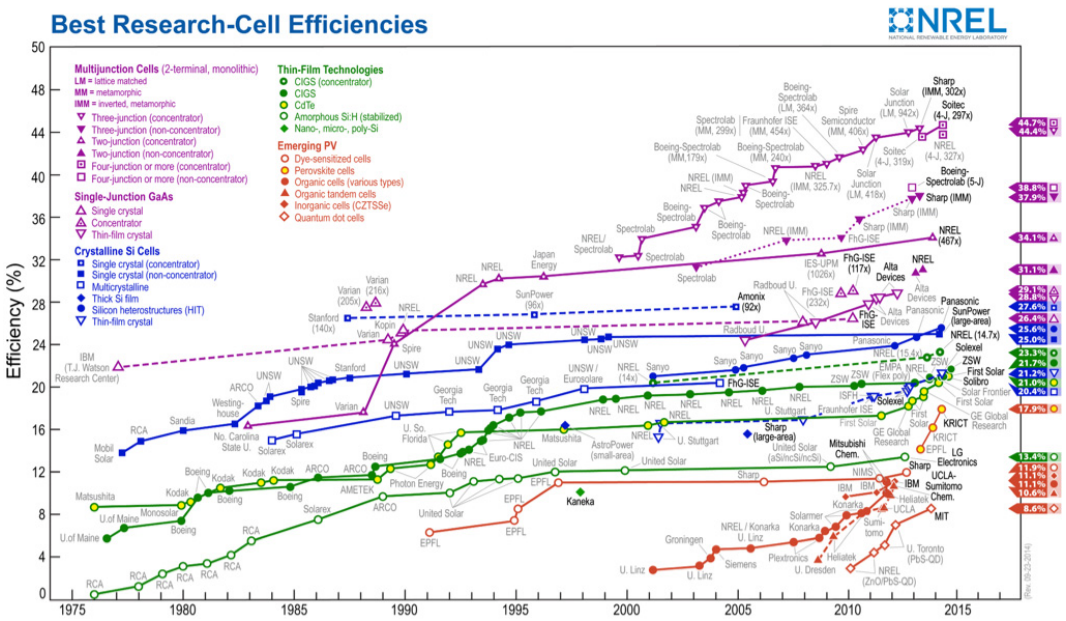

Figure 2. Maximum solar cell efficiencies reported by the National Renewable Energy Laboratory (NREL).

1-2 Organic Semiconductors

Conjugated organic semiconductors are the most recent candidates for the semiconductor electronics, as they are lightweight, easily fabricated, flexible, and low cost. By virtue these properties, which are not commonly found in inorganic materials, conjugated organics are ideal for next-generation devices. In addition, there are various types of organic semiconductors available in the market today, which makes them favorable for use in tuning devices. Organic semiconductors are based on carbon and hydrogen, but also contain nitrogen, oxygen, sulfur, fluorine, and other halogens. A combination of these elements provides the different properties of organic semiconductors. The optical and electrochemical properties of organic semiconductors can also be altered by chemical modifications. Furthermore, the

nature of molecular ordering in solid states can be controlled by manipulating the intermolecular interactions. These unique properties of organic semiconductors have been exploited in several organic devices such as organic-field transistors (OFETs), organic light-emitting diodes (OLEDs), and organic solar cells (OSCs).[4-6]

History of Organic Semiconductors

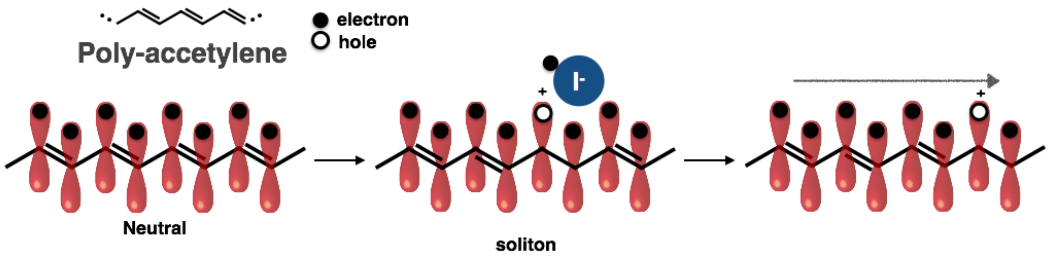

Figure 3. Chemical structure and conductivity mechanism of poly-acetylene.

Shirakawa, MacDiarmid, and Heeger were awarded the Novel Prize in Chemistry in 2000 for developing a conductive polymeric material based on doped polyacetylene (Figure 3).[7] Since then, polymereric to small molecular organic semiconductors have been widely researched. The π-orbitals are important for the charge transfer and the crystalline structure of organic semiconductors. Each functional group in an organic semiconductor is connected to another functional group by single, double, and triple covalent bonds.

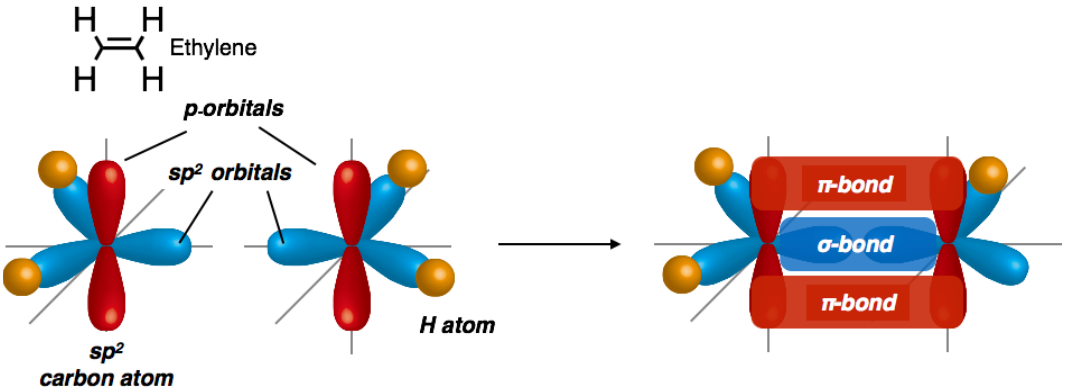

Figure 4. Molecule orbital structure of ethylene.

Molecular orbitals govern the interconnections and charge transport properties of organic materials. For example, the simplest alkene, ethylene (CH_2=CH_2), is held together by σ and π-bonds. In this molecule, the sp^2 hybridized carbon forms a double bond (Figure 4), while the σ and π-bonds establish the connection. Because the π-bond is weaker than the σ-bond, the π-electrons are easily mobilized, allowing charge carrier transport thorough the overlapped π-orbitals.

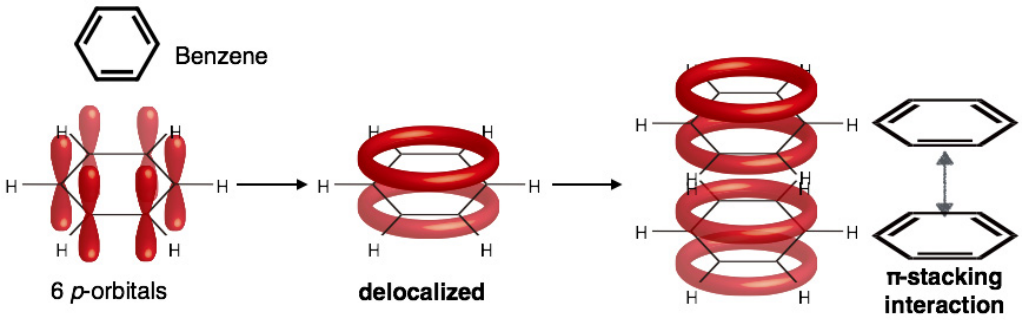

Figure 5. Schematic representation of delocalized π-electron clouds in benzene and the π-stacking interaction in a benzene dimer.

Organic semiconductors are reliant on non-covalent interactions such as hydrogen bonding and van der Waals forces. The π-stacking interaction determines the high-order structure of organic semiconductors. In aromatic compound with rigid and planar structures, the π-orbitals are delocalized into a π-electron cloud. Thus, when stacked face-to-face, aromatic compounds are stabilized by London dispersion forces (Figure 5). Such interactions influence the conformations of large molecules such as DNA and RNA.[8] The stacked structures of organic semiconductors also provide pathways for charge carrier transport. This technology is used to control self-assembly of nanostructure.

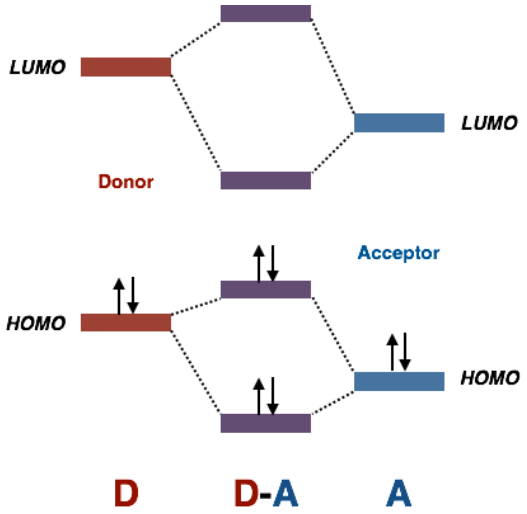

Figure 6. Energy diagrams of HOMO—LUMO interactions between donor and acceptor.

The highest occupied molecular orbital (HOMO) and the lowest unoccupied molecular orbital (LUMO) are critical in device applications. The bandgap between the HOMO and LUMO determines the light absorption, charge separation, and charge transportation properties of the material. The donor—acceptor strategy is the most common approach in organic semiconductor design. The interaction of between the electron donating and the electron accepting units destabilizes HOMO and stabilizes LUMO energy levels (Figure 6). Therefore, tuning the HOMO and LUMO energy levels by altering the donor and acceptor contents has attracted great interest in organic semiconductor research.

Organic Solar Cells (OSCs)

Devices based on organic materials, such as OLEDs, OFETs, and OSCs have been targeted for their lightweight, low cost, and flexibility. OSCs are considered as attractive candidates for next-generation green technologies. OSCs are classified into two types: bulk-heterojunction (BHJ) solar cells and dye-sensitized solar cells (DSSCs). The performances of both categories have rapidly improved over the past decade, and solar cells efficiencies have increased by more than 10%.[3] OSCs operate by 1) absorbing photons, 2) photoinduced charge separation into mobile carriers, and 3) collection of the charge carriers.

Characterization of OSCs

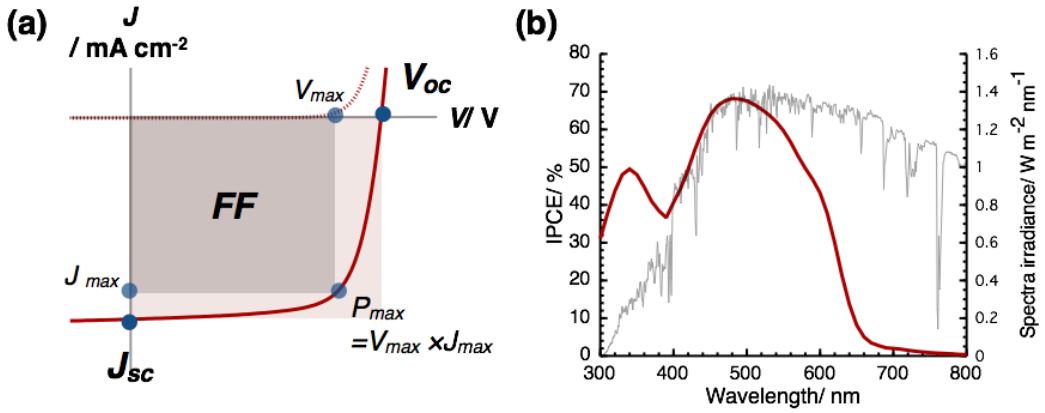

Figure 7. (a) Current density versus voltage (*J*—*V*) plot; (b) incident photon-to-current conversion efficiency spectrum (red) and spectra of sunlight irradiation (black).

The current−voltage curve of a general solar cell is shown in Figure 7a. The performance of the solar cells is assessed by the short-circuit current density (J_{sc} /mA cm^2), the open circuit voltage (V_{oc} /V) and the fill factor (FF). These three factors determine the overall power conversion efficiency (PCE), calculated as

$$PCE = \frac{V_{max}\,(V)\times I_{max}(A/cm^2)}{100\ (mW/\,cm^2)}\times 100\ (\%)$$

$$= V_{oc}\,(V)\times J_{sc}(mA/cm^2)\times FF\ (\%) \quad \text{(Equation 1)}$$

J_{sc} is influenced by the number of absorbed photons, the internal quantum efficiency, and transportation of the charge carrier in materials. V_{oc} is primarily determined the energy difference of the donor HOMO and the acceptor LUMO. The FF is ratio of the maximum power (P_{max}) to the product of J_{sc} and V_{oc}.

The incident photon-to-current conversion efficiency (IPCE) of a device (Figure 7b) is the number ratio of the generated electrons to the incident photons:

$$IPCE = \frac{number\ of\ electron\ generated}{number\ of\ incident\ photons} \times 100$$

$$= \frac{1240 \times J_{sc}\ (mA/cm^2)}{\lambda\ (nm) \times I_{inc} (mW/cm^2)} \times 100\ (\%) \quad \text{(Equation 2)}$$

J_{sc} is calculated by:

$$J_{sc} = A^{-1} \int_{\lambda=0}^{\lambda=\lambda_g} \phi_p(\lambda) \eta_{IPCE}(\lambda)\, d\lambda \quad \text{(Equation 3)}$$

where A is the cell area, λ is the wavelength of the light, λ_g is the limit of the active layer spectrum of the device, Φ_p is the photon flux, and $\eta_{IPCE}(\lambda)$ is device limit at a given wavelength. The IPCE is also depends on the absorbed photon-to-current conversion efficiency (APCE), light harvesting efficiency (LHE), and transmittance of the device (T).

$$IPCE = \frac{APCE}{LHE} = \frac{APCE}{1 - T}(\%) \quad \text{(Equation 4)}$$

1-3 Bulk-heterojunction (BHJ) Solar Cells

Because of they are efficient, low cost, and easily fabricated, BHJ solar cells have attracted much attention as renewable energy sources.[9, 10] BHJ solar cells are composed of the donor and acceptor materials. BHJ solar cells operate via three-step mechanism (Figure 8).

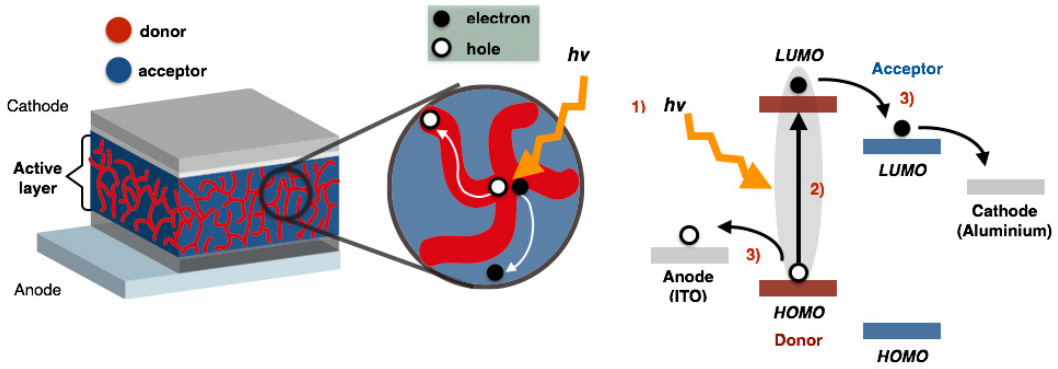

Figure 8. Structure of a BHJ solar cell and schematic of an energy diagram of its band structure of BHJ solar cells.

1) Photoactive materials harvest sunlight and generate exitons.

2) The exitons are diffused to the donor−acceptor interface, where they are separated into electrons and holes.

3) The electrons and holes are attracted to the opposite electrodes and collected.

BHJ Structure

The structure of the BHJ solar cells is an important consideration in molecular design. Since the discovery of the photoinduced charge transfer between two organic semiconductors, the development of the organic solar cells has rapidly increased. The principle of the heterojunction solar cell was reported by Tang.[11] In the planar-heterojunction architecture, the two materials are sandwiched between two electrodes (Figure 9a). Tang used copper phthalocyanine as the electron donor and perylene diimide as the electron acceptor. The donor and acceptor interface is responsible for the photoinduced charge carrier. An alternative heterojunction solar

cell structure, called bulk-heterojunction (BHJ) solar cells, was proposed by Hiramoto et al. (Figure 9b).[12] In their design, an intermediate layer containing mixed donors and acceptors is fabricated by a vacuum deposition process. The BHJ solar cell generates twice as much photocurrent as its planar-heterojunction counterpart. The photoinduced charge generation is probably enhanced by the larger donor—acceptor interface in the intermediate layer of the BHJ.

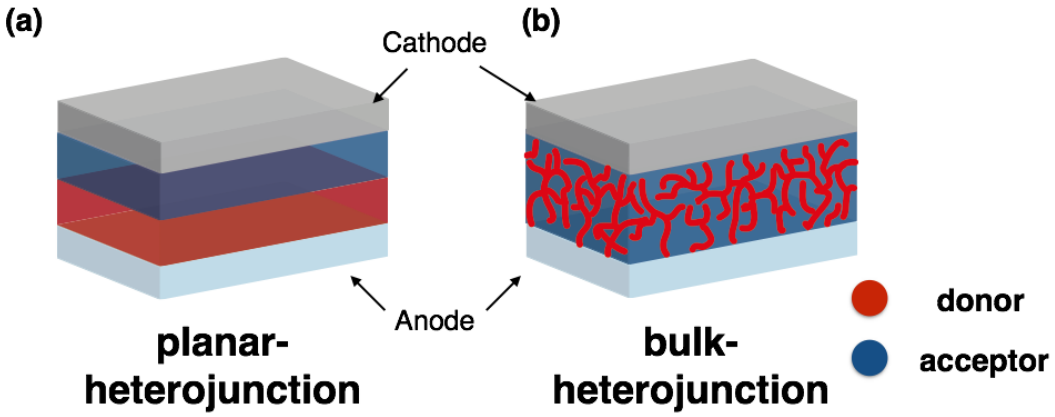

Figure 9. Structure of planar and bulk heterojunction solar cells.

The first solution-processed BHJ solar cell was reported by Heeger et al.[13] Device fabrication was enebled by selecting the soluble fullerene $PC_{61}BM$ ([6,6]-phenyl-C61-butyric acid methyl ester) as the acceptor molecule (donor molecule was polymer).[14] Fullerene possesses all the properties of an excellent electron acceptor: suitable HOMO and LUMO energy levels, high electron affinity, and electron mobility. The mixed solution of donor and acceptor in organic solvent are easily to obtain the film that well mixed and spontaneous phase separated network by spin-coating technique. Since PCBMs are recognized as strong electron acceptor, researchers have focused on designing and synthesizing donor materials for solution-processed BHJ solar cells.

Organic Semiconductors for BHJ Solar Cells

Electron donor materials for BHJ solar cells have been investigated throughout past decade. Developments have increased the power conversion efficiency of these cells from 2% to 11.1%. To ensure high PCE, the organic semiconductors in BHJ solar cells required to 1) harvest a considerable amount of the sunlight and 2) control the BHJ phase-separated structure. To this end, numerous π-conjugated organic semiconductors from polymers to small molecules have been investigated.[15-17] The electron acceptor in BHJ designs is usually a fullerene derivative, while the electron donor is either a polymer or a small molecule.

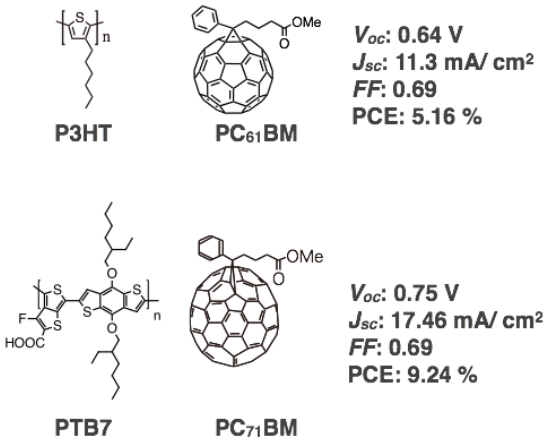

Figure 10. The chemical structure of the polymeric donors in BHJ solar cells.

Polymers are composed of repeating monomeric units connected by covalent bond. The molecular weight of typical polymer exceeds 10000. The conjugated structure of the polymer backbone can absorb a wide range of the sunlight. Moreover, the solar cell properties are enhanced by the transport of charge carriers along the chains. Thiophene polymer poly(3-hexylthiophene) (P3HT) packed in a two-dimensional self-organized structure has been lauded for its high carrier mobility.[18] P3HT is a common donor material in BHJ solar cells. The PCE of P3HT/$PC_{61}BM$-based devices can exceed 5%, [19-21] whereas that of a low bandgap polymer of PTB7 containing thieno[3,4-*b*]thiophene and benzodithiophene units exceeds 9% (Figure 10).[22] The quinoidal structure of the PBT7 polymer is highly stabilized, enabling visible light absorption from 300 nm to 700 nm. In addition, the

fluorine introduced into the polymer unit stabilizes the HOMO energy levels, increasing the V_{oc} relative to P3HT. However, the device performance is heavily compromised by the polydispersity of the molecular weights and trace impurities in the conjugated polymer.[23] To avoid this drawback, discrete and well-defined molecular donors have been designed and applied as the donor materials in BHJ solar cells.

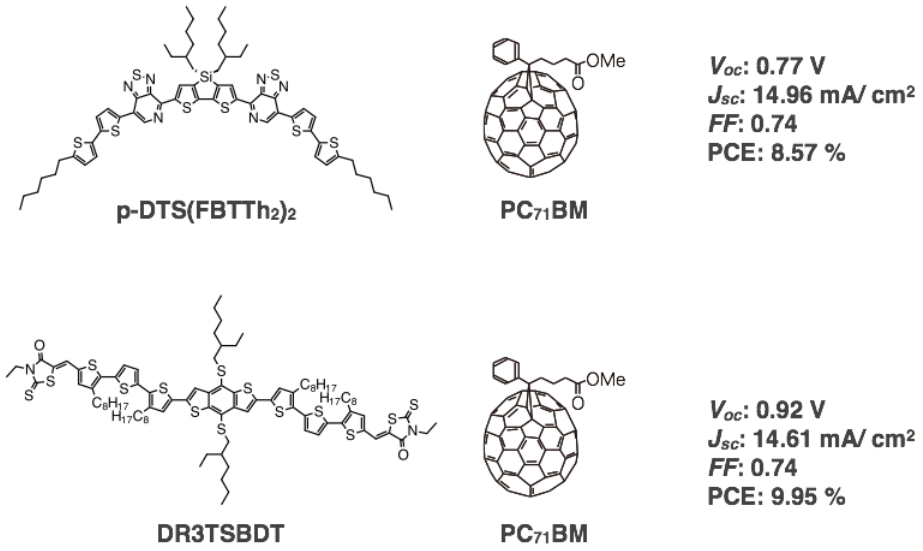

Figure 11. Chemical structures of small molecule donors used in BHJ solar cells.

The advantages of small molecular materials over polymers are greater variety in chemical structure, easier energy level tuning, mobility control, and less batch-to-batch variation. By appropriately designing the chemical structure of the small molecules, researchers have achieved PCEs approaching 10% in solution-processed BHJ solar cells. The PCE of donor–acceptor solar cells based on oligomer p-DTS($PTTh_2$)$_2$ and [6,6]-phenyl C_{70}-butylic acid methyl ester ($PC_{71}BM$) was reported as 8.57%.[24] In addition, the optical properties and energy levels of the cell are easily tuned by chemical modifications.[25] [26] The highest power conversion efficiency (PCE = 9.95%) was reported by Kan et al., who incorporated the low bandgap donor DR3TSBDT into BHJ solar cells.[27] According to Kan et al., PCE can

be further enhanced by controlling the nanoscale interpenetrating network of the donor and acceptor by thermal or solvent vapor annealing.

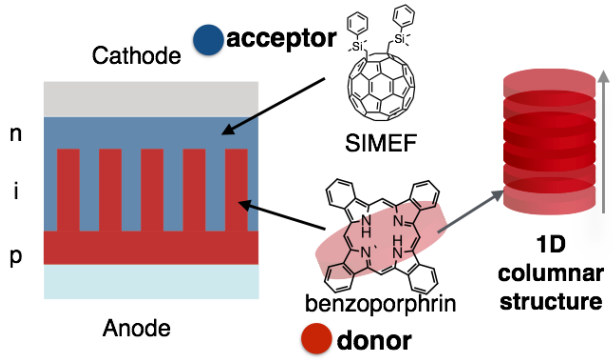

Figure 12. The chemical structure and device of the controlled BHJ solar cells.

Because the exiton diffusion length is typically ~10 nm, controlling the BHJ structure is an effective means of improving cell efficiency.[11] By thermally converting benzo-porphyrin during the preparation of the active layer, Matsuo et al. improved the PCE to 5.2% (Figure 12).[28] The stacked molecules formed a columnar structure in the intermediate layer, which optimized the phase separation in the active layer. Wong et al. reported on HBC-based BHJ solar cells with PCEs of 2.5%.[29] Disk-shaped molecules are particularly targeted as molecular components in BHJ solar cells.

Disk-shaped Molecules for BHJ Solar Cells

Polycyclic aromatic hydrocarbon (PAH) materials such as tetracene, triphenylrene, and pyrene are popularly employed in small molecule semiconductors (Figure 13). PAHs are aromatic materials that satisfy Huckel's rule. The planar structures of PAHs are rich in π-electrons, promoting the crystalline phase that allows charge carrier transportation.[30] In addition, PAH structures range from linear to disk-like, enabling the tuning of desirable properties such as high carrier mobility and fluorescence.

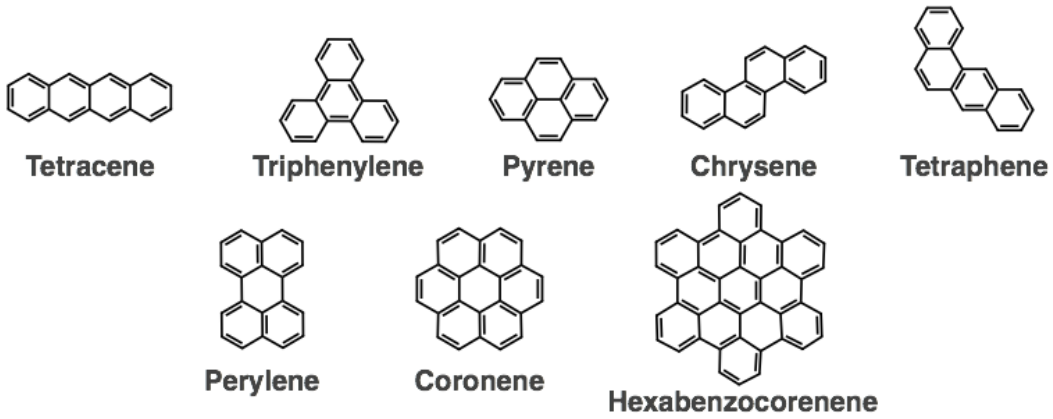

Figure 13. Chemical structures of polycyclic aromatic hydrocarbons

Disk-shaped PHAs, namely pyrene, triphenylene, and hexabenzocoronene, are attractive materials for optoelectronic devices because their planar structure and abundance of π-electrons enable self-assembly first into columns and finally into two-dimensional (2D) or three-dimensional (3D) supramolecules (Figure 14). All of the carbon atoms in disk-shaped PAHs are sp^2. The 2D or 3D nanostructures are established by interactions among the 1D columns. The columnar assemblies provide conduits for energy or charge carrier transport. A plastic crystalline of hexahexylthiotriphenyrene has demonstrated high mobility of photoinduced charge carriers (of the order of 0.1 cm^2 V^{-1} s^{-1}).[31] An HBC derivative with hydrophilic/hydrophobic side chains also delivers high mobility (0.2 cm^2 V^{-1} s^{-1}), by virtue of its helical columnar structure.[32] In addition, the modified chemical structure allows the tuning not only of the solid-state molecular ordering but also of the optical and electrochemical properties.

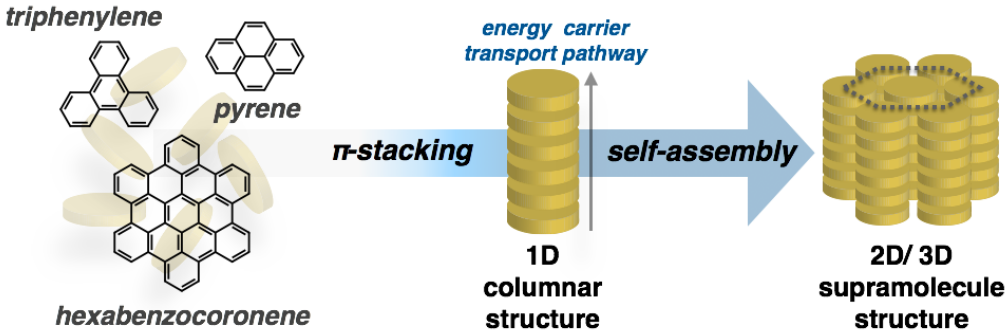

Figure 14. Self-assembly of disk-shaped PAH molecules into 1D structures and finally into 2D/3D structures.

Pyrene is a fluorescence chromosphere popular in bio-imaging and sensing research.[33] Pyrene building blocks have also been employed in organic semiconductors such as OLEDs, OFETs, and OSCs.[34-39] Pyrene consists of four fused aromatic rings, which can be chemically modified to tune the optical, electrochemical, and carrier transport properties (Figure 15).[33] Control of the molecular ordering and tuning of the optical and electrochemical properties are required in organic devices. From this viewpoint, pyrene presents as a promising building block of the donor component in BHJ solar cells.

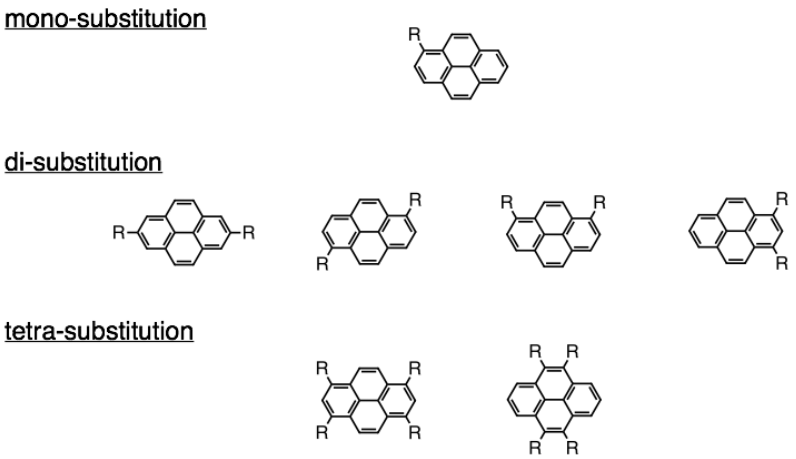

Figure 15. Chemical structures of substitution-modified pyrene molecules.

1-5 Dye-sensitized Solar Cells

Dye-sensitized solar cells (DSSCs) based on nanocrystalline titanium oxide (TiO_2) have been investigated as low-cost alternatives to silicon-based photovoltaic cells. The DSSC was first conceptualized by Grätzel et al. in 1991.[40]

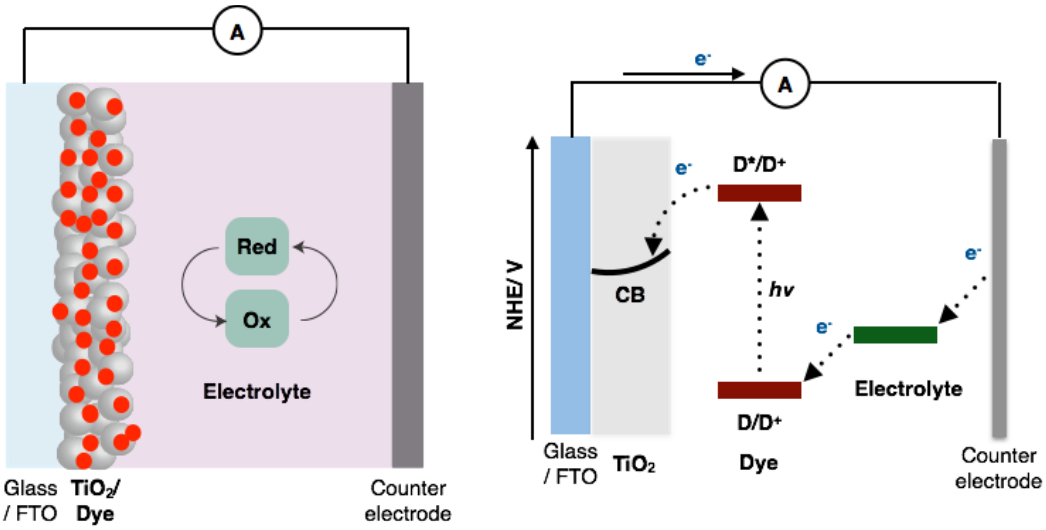

Figure 16. (a) Device structure of conventional DSSCs. (b) Energy levels diagrams of DSSCs.

The device structure and energy level diagrams of DSSCs are shown in Figure 16. A conventional DSSC contains a dye/nanocrystalline TiO_2 compound, a redox couple, and a counter electrode. The DSSC operates by a three-step mechanism.

1) Sunlight is absorbed by the dye.

2) Charge separation occurs, and the photoinduced electrons are ejected from the exited dye to the conduction band (CB) of TiO_2.

3) The dye cation is reduced by the redox couple.

Organic Semiconductors for Dye-sensitized Solar Cells

When the dye absorbs sunlight, the generated electrons are injected into the conduction band of the working electrodes. The dyes used in DSSCs are classified into two types: metal-complex dyes and organic dyes.

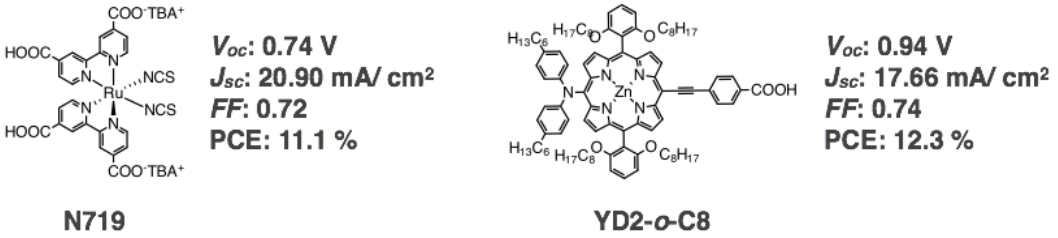

Figure 17. Chemical structures of metal-complex dyes used in DSSCs.

The PCEs of state-of-the-art DSSCs based on ruthenium complexes, such as N719, N3, Z907, and black dye, have exceeded 11% (Figure 17).[41] Because ruthenium complexes absorb over a wide range of the visible spectrum, they are effective sunlight harvesters. Zinc-porphyrin dyes with a cobalt (II/ III) redox mediator have demonstrated even higher PCE (over 12%).[42] However, metal-complex dyes are disadvantaged by the low absorption coefficient and high cost. Because of these drawbacks, researchers have concentrated on metal-free organic dyes.

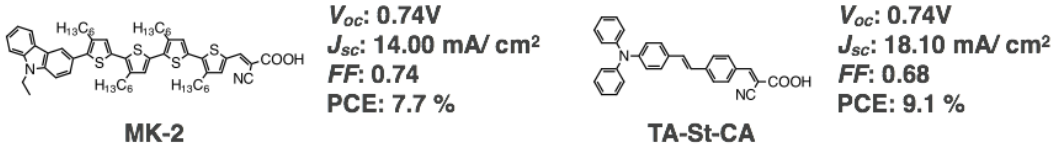

Figure 18. Chemical structure of organic dyes used in DSSCs.

Metal-free organic dyes are promising candidates for high-performance DSSCs. The use of metal-free organic dyes was first reported by Hara et al. They used carbazole and cyanoacrylic acid as donor and acceptor, respectively, and achieved 6.8% of PCE.[43] Since then, a wide variety of organic dyes has been reported (Figure 18).[44] The advantages of organic dyes are high molar coefficient and low cost. Typically, an organic dye consists of a donor, a π-bridge, and an acceptor (Figure 19). The electron-donating units in the donor parts are usually triphenyamine or carbazoles.

The π-bridges are repeating units such as oligothiophene or vinylene. The acceptor groups contain an electron-withdrawing unit with an anchoring group (carboxylic acid or pyridine). The expanded π-conjugated structure of organic dyes broadens their absorption range, thereby increasing the PCE. The donor, π-bridge, and acceptor units can be recombined for tuning the optical and electrochemical properties.

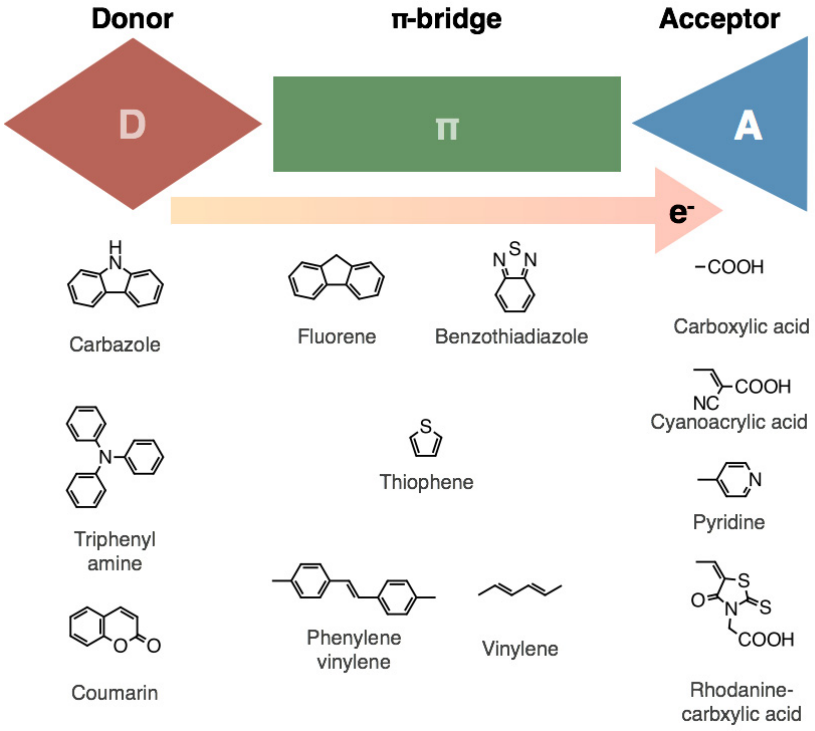

Figure 19. Chemical constituents of organic D-π-A dyes.

1-6 Study Objectives

Because of their unique structural and optical properties, small molecule-based organic semiconductors are promising candidates for optoelectronic devices. The optical and electrochemical properties of small molecules can be precisely tuned by chemical modifications. Controlling the nanostructure of small molecules is also important for improving device performance. For example, the structures of BHJ solar cells containing mixed donor and acceptor materials must allow phase separation. Given that the carrier photoexcitation recombination lengths are typically 10 nm, the scale of the donor–acceptor separated structure must be 10–20 nm.[10] To satisfy this requirement, the separated structure must be controlled by molecular interactions. The π-stacking interaction is essential for self-assembly into a 1D nanostructure. The favorable overlap of π-orbitals in adjacent molecules enhances the charge carrier mobility. In OSCs, the organic semiconductors require tuning to optimize their absorption properties and the HOMO and LUMO energy levels. These properties are most commonly controlled by the donor–acceptor strategy. The co-polymer of the donor–acceptor mix increases the absorption range of visible light. In addition, the HOMO and LUMO energy levels can be tuned by selecting appropriate donor and acceptor components. DSSCs typically employ organic dyes composed of three units: a donor, a π-bridge, and an acceptor. The D-π-A structures of organic dyes promote the intramolecular charge transfer of the electrons to TiO_2.

In this thesis, small-molecule organic semiconductors were developed and applied to OSCs. To control the nanostructure and the optical and electrochemical properties of the device, a series of organic semiconductors with different functional groups were synthesized, and the structure–property relationships of the synthesized products were investigated.

Chapter 2 describes the disk-shaped molecules used as the electron donor component in the BHJ solar cells. To ensure the high performance of the BHJ solar cells, the phase-separated structure must be controlled. To this end, pyrene molecules were self-assembled into a 1D columnar structure via π-stacking interactions. To

improve sunlight harvesting, oligothiophene side chains of different lengths were introduced to the pyrene core. The self-assembled structures of the pyrene derivatives were investigated by XRD and POM. The structure–performance relationships of the modified pyrenes in BHJ solar cells were also investigated.

Chapter 3 describes how the light-harvesting range is improved in the disk-shaped donors. The wider the absorption range of sunlight becomes the higher performance of the BHJ solar cell are given. For this purpose, the acceptor unit of rhodanine was introduced to the terminal position of the disk-shaped donors. The optical properties and the HOMO and LUMO energy levels of these molecules were investigated. The nanostructure of the solid state and the hole mobilities of the synthesized donors were also investigated. BHJ solar cells containing the rhodanine-terminated donors were fabricated, and their properties were investigated.

Chapter 4 describes the development of non-fullerene BHJ solar cells. Replacing the fullerene derivatives in BHJ solar cells by appropriate alternatives is expected to further boost cell performance. Perylene diimide (PDI) derivatives are widely used as acceptor building blocks. Therefore, in this chapter, PDI derivatives having thiophene substituents were synthesized, and their optical and electrochemical properties were investigated. Non-fullerene BHJ solar cells composed of disk-shaped molecules as an electron donor and PDI derivatives as an acceptors were fabricated, and their properties were investigated. To optimize the phase-separated structure in non-fullerene BHJ solar cells, the effect of solvent additives was also investigated.

Chapter 5 describes the development of D-π-A organic dyes for DSSCs. A fluorene-benzothiadiazole unit was used as an electron-transporting unit in organic semiconductors. An appropriate combination of donor, π-bridge, and acceptor is important for ensuring excellent DSSCs properties. In this chapter, the fluorene-benzothiadiazole unit was employed as the π-bridge of the organic dye. The DSSC properties were then investigated for different donor and acceptor units.

1-7 Abbreviations

For clarity, the author has used abbreviations that are most common in the field and summarized in Table 1.

Table 1. List of most common abbreviations used throughout the thesis.

AM1.5	Air mass 1.5
AFM	Atomic force microscope
BHJ	Bulk-heterojunction
DSC	Differential scanning calorimetry
FF	Fill factor
HOMO	Highest occupied molecular orbital
HPLC	High performance liquid chromatography
ITO	Indium-tinoxide
IPCE	Incident photon-to-current conversion efficiency
J_{sc}	Short-circuit current density
LUMO	Lowest unoccupied molecular orbital
MALDI-TOF-MS	Matrix assisted laser deposition/ionization time of flight mass spectrometry
NMR	Nuclear magnetic resonance
$PC_{61}BM$	Phenyl-C_{61}-butylic acid methyl ester
$PC_{71}BM$	Phenyl-C_{71}-butylic acid methyl ester
P3HT	Poly(3-hexylthiophene)
PEDOT:PSS	Polyethylenedioxythiophene:polystyrenesulfonate
PCE	Power conversion efficiency
SCLC	Space charge limited current
TPOM	Temperature-controlled polarized microscope
TGA	Thermo gravimetric analysis
V_{oc}	Open-circuit voltage
XRD	X-ray diffraction

1-8 References

1. Y. Sun, J. A. Rogers, *Adv. Mater*., **2007**, 19, 1897.
2. D. M. Chapin, C. S. Fuller, G. L. Pearson, *J. Appl. Phys*., **1954**, 25, 676.
3. http://www.nrel.gov/ncpv/images/efficiency_chart.jpg
4. G. Horowitz, *Adv. Mater*., **1998**, 10, 365.
5. J. Roncali, *Chem. Rev*., **1997**, 97, 173.
6. T. Ameri, P. Khoram, J. Min, C. J. Brabec, *Adv. Mater*. **2013**, 25, 4245.
7. H. Shirakawa, E. J. Louis, A. G. MacDiarmid, C. K. Chiang, A. J. Heeger, *J. Chem. Soc. Chem. Comm*., **1977**, 578.
8. D. B. Hall, E. Holmlin, J. K. Barton, *Nature*, 1996, **382**, 731
9. S. Günes, H. Neugebauer, N. S. Sariciftci, *Chem. Rev.*, 2007, **107**, 1324.
10. A. J. Heeger, *Adv. Mater.*, **2014**, 26, 10.
11. C. Tang, *Appl. Phys. Lett*., 1**986**, 48, 183.
12. M. Hiramoto, H. Fujikawa, M. Yokoyama, *Appl. Phys. Lett*., **1991**, 58, 1062.
13. G. Yu, J. Gao, J. C. Hummelen, F. Wudl, A. J. Heeger, *Science*, **1995**, 270, 1789.
14. J. C. Hummelen, B. W. Knight. F. LePeq, F. Wuld, *J. Org. Chem*., **1995**, 60, 532.
15. A. Mishra, P. Bäuerle, *Angew. Chem. Int. Ed.*, 2012, **51**, 2020.
16. G. Dennler, M. C. Scharber, C. J. Brabec, *Adv Mater*., **2009**, 21, 1323.
17. P. M. Beaujuge, J. M. Fréchet, *J. Am. Chem. Soc.*, **2011**, 133, 20009.
18. H. Srringhaus, P. J. Brown, R. H. Friend, M. M. Nielsen, K. Bechgaard, B. M. W. Langeveld-Voss, A. J. H. Spiering, R. A. J. Janssen, E. W. Meijer, P. Herwig, D. M. de Leeuw, *Nature*, **1999**, 401, 685.
19. M. R. Reyes, K. Kim, D. L. Carroll. *J. Phys. Lett*., **2005**, 87, 083506.
20. J. Y. Kim, S. H. Kim, H-H. Lee, K. Lee, W. Ma, X. Gong, A. J. Heeger, *Adv. Mater*., **2006**, 18, 572.
21. M. D. Irwin, D. B. Buchholz, A. W. Hanis, R. P. H. Chang, T. J. Marks, *Proc. Natl. Acad. Sci. U.S.A.*, **2008**, 106, 2783.
22. Z. He, C. Zhong, S. Su, M. Xu, H. Wu, Y. Cao, *Nat. Photon*., **2012**, 6, 591.
23. R. C. Coffin, J. Peet, J. Rogers, G. C. Bazan, *Nat. Chem.*, **2009**, 1, 657.
24. V. Gupta, A. K. K. Kyaw, D. H. Wang, S. Chand, G. C. Bazan, A. J. Heeger, *Sci. Rep*., **2013**, 3, 1965.
25. X. Liu, Y. Sun, B. B. Y. Hsu, A. Lorbach, L. Qi, A. J. Heeger, G. C. Bazan, *J. Am.*

Chem. Soc., **2014**, 136, 5697.

26. X. Liu, Y. Sun, L. A. Perez, W. Wen, M. F. Toney, A. J. Heeger, G. C. Bazan, *J. Am. Chem. Soc*., **2012**, 134, 20609.
27. B. Kan, Q. Zhang, M. Li, X. Wan, W. Ni, G. Long, Y. Wang, X. Yang, H. Feng, Y. Chen, *J. Am. Chem. Soc*., **2014**, 136, 15529.
28. Y. Matsuo, Y. Sato, T. Niinomi, I. Soga, H. Tanaka, E. Nakamura, *J. Am. Chem. Soc*., **2009**, 131, 16048.
29. W. W. H. Wong, C-Q. Ma, W. Pisula, C. Yan, X. Feng, D. J. Jones, K. Müllen, R. A. Janssen, P. Bäuerle, A. B. holmes, *Chem. Mater*., **2009**, 22, 457.
30. J. E. Anthony, *Chem, Rev*., **2006**, 106, 5028
31. X. Feng, V. Marcon, W. Pisula, M. T. Hansen, J. Kirkpatrick, F. Grozema, D. Andrienko, K. Kremer, K. Müllen, *Nat. Mater*, **2009**, 8, 421.
32. D. Adam, P. Schuhmacher, J. Simmerer, L. Laussling, K. Simensmeyer, K. H. Etzbachi, H. Ringsdorf, D. Haarer, *Nature*, **1994**, 371, 141.
33. T. M. Figueira-Durate, K. Müllen , *Chem. rev*., **2011**, 111, 7260.
34. K. Suzuki, A. Seno, H. Tanabe, K. Ueno, *Synth. Met*. **2004**, 143, 89.
35. F. Liu, C. Tang, Q-Q. Chen, F-F. Shi, H-Bin Wu, L-H. Xie, B. Peng, W. Wei, Y. Cao, W. Huang, *J. Phys. Chem. C,* **2009**, 113, 4641.
36. S. Diring, F. Camerel, B. Donnio, T. Dintzer, S. Toffanin, R. Capelli, M. Muccini, R. Ziessel, *J. Am. Chem. Soc.,* **2009**, 131, 18177.
37. F. Moggia, C. Videlot-Ackermann, J. Ackermann, P. Raynal, H. Brisset, F. Fages, *J. Mater. Chem*., **2006**, 16, 2380.
38. M. Ashizawa, K. Yamada, A. Fukaya, R. Kato, K. Hara, J. Takeya, *Chem. Mater*. **2008**, 20, 4883.
39. O. P. Lee, A. T. Yiu, P. M. Beaujuge, C. H. Woo, T. W. Holcombe, J. E. Millstone, J. D. Douglas, M. S. Chen, J. M. J. Fréchet, Adv. Mater., **2011**, 23, 5359.
40. B. O'Regan, M. Grätzel, *Nature*, **1991**, 353, 737.
41. Y. Chiba, A. Islam, Y. Watanabe, R. Komiya, N. Koide, L. Han, *Jpn. J. Appl. Phys*., **2006**, 45, L638.
42. A. Yella, H.-W. Lee, H. N. Tsao, C. Yi, A. K. Chandiran, Md. K. Nazeeruddin, E. W.-G. Diau, C.-Y. Yeh, S. M. Zakeeruddin, M. Grätzel, *Science*, **2011**, 334, 629.
43. Z-S, Wang, N. Koumura, Y. Cui, M. Takahashi, H. Sekiguchi, A. Mori, T. Kubo, A. Furube, K. Hara, *Chem. Mater*., **2008**, 20, 3993.

44. A. Mishra, M. K. R. Fischer, P. Bäuerle, *Angew. Chem. Int. Ed.*, **2009**, 48, 2474.

Chapter 2

Solution-Processed Bulk-Heterojunction Solar Cells Containing Self-Organized Disk-Shaped Donors

Abstract

Two molecular disks **1** and **2** composed of a central pyrene core, four oligothiopenes, and peripheral alkyl chains were synthesized and characterized with respect to optical and redox properties in solution and in solid films. It was found that the lowest unoccupied molecular orbital (LUMO) energy levels of **1** and **2** were ideal for achieving efficient electron transfer to fullerene derivatives $PC_{61}BM$ and $PC_{71}BM$, and that **1** and **2** can function as electron donor components in solution-processed bulk-heterojunction (BHJ) solar cells. Disk-shaped molecules **1** and **2** organized ordered structures through intermolecular π-π interactions as monitored by temperature-controlled polarized optical microscope (TPOM), differential scanning calorimetry (DSC), and powder X-ray diffraction (XRD). Solution-processed BHJ solar cells using **1** or **2** as electron donor materials and fullerene derivatives as acceptor materials were fabricated and investigated. The oligothiophene lengths were reflected in the performance characteristics of solar cell devices fabricated using disk-shaped donors **1** and **2**. Power conversion efficiency (PCE) of 2.6% was achieved for small-molecule BHJ solar cells containing self-organized crystals of **2** in the active layer under one sun condition.

2-1 Introduction

Organic photovoltaic devices have been intensely investigated as a promising candidate for achieving low-cost, flexible, and scalable solar cells. Among the organic photovoltaic devices, power conversion efficiency (PCE) of solution-processed bulk heterojunction (BHJ) solar cells has been rapidly increased through the precise molecular tuning of organic semiconductors, the control of nanostructures within the active layers, and the optimization of device structures.[1,2] To date, PCE has reached 8% for state-of-the-art BHJ solar cells based on conjugated polymer/fullerene blends as reported in scientific literature.[3] Despite the high PCE levels that have been obtained, the device performance of polymer-based BHJ solar cells is strongly affected by the polydispersity of molecular weights and the contamination of trace impurities in the conjugated polymers. To avoid this drawback, discrete and well-defined molecular donors have been designed and applied as the molecular components of active layers in small-molecule BHJ (SM BHJ) solar cells.[4–9] Sun et al. reported on a high conversion efficiency (PCE = 6.7%) for SM BHJ solar cells by using the low-band gap organic donor DTS($PTTh_2$)$_2$ and [6,6]-phenyl C_{70}-buthyric acid methyl ester ($PC_{71}BM$).[10] They also found that the addition of solvent additives resulted in the enhancement of PCE due to the reduction of domain sizes in the active layer of SM BHJ solar cells. The control of bicontinuous network structure in the active layers allows a high interfacial area to optimize the exciton dissociation and the efficient transport of the generated charges to the electrodes.[11] Further improvement in device performance requires the enhancement of charge mobility in the phase-segregated active layers. π-Conjugated disk-shaped molecules such as pyrene, triphenylene, and hexa-peri-hexabenzocoronene are attractive molecular units for forming highly ordered one-dimensional stacks through intermolecular π-π interaction.[12] The large π-π overlap within self-organized stacks of disk-shaped molecules provides a transport pathway for charge or energy. A threedimensionally ordered helical liquid crystalline phase of hexahexylthiotriphenylene exhibited a high mobility for photoinduced charge carriers of the order of 0.1 $cm^2\ V^{-1}\ s^{-1}$,[13] and this

mobility in the liquid crystalline phase is comparable to that in organic single crystals.[14] High charge mobility of the stacks would be effective for enhancing BHJ solar cell performance. [15–17] Wong et al. reported that hexa-peri-hexabenzocorones functionalized with a series of thiophene dendrons exhibited good PCE in SM BHJ solar cells.[15] Lee et al. successfully enhanced PCE in SM BHJ solar cells by using π-stacking of pyrenes in organic donors.[16]

In this chapter, a disk-shaped pyrene with linear oligothiophenes attached to its periphery was investigated as a self-organizing electron donor component in combination with fullerene derivatives in SM BHJ solar cells. Well-defined oligothiophenes have been synthesized as donor components for SM BHJ solar cells.[18–20] While these oligothiophenes functioned as donor components in SM BHJ solar cells, the cells displayed low PCE values due to their narrow absorption range and poor phase separation. The synthesized disk-shaped oligothiophenes **1** and **2** bearing a planar pyrene core were organized into ordered structures in the solid phase and PCE of 2.6% was achieved for a device containing a disk-shaped donor **2** with $PC_{71}BM$ as the acceptor material.

2-2 Results and Discussion

2-2-1 Synthesis of Disk-shaped Molecules

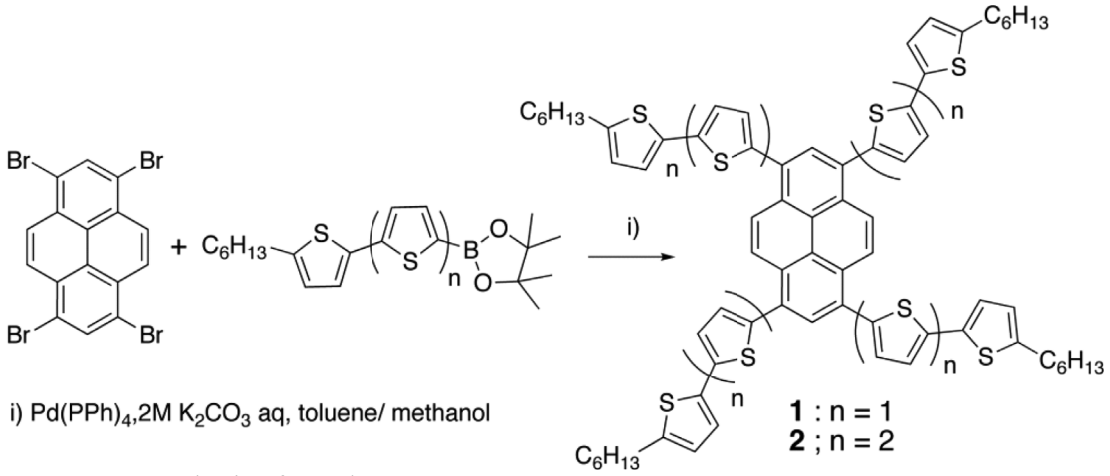

Scheme 1. Synthesis of **1** and **2**.

We have designed two molecular disks **1** and **2**, in which four oligothiophenes were attached at the 1, 3, 6, and 8 positions of a pyrene core (Scheme 1). Disk-shaped donor **1** and **2**, having oligothiophenes of different lengths, were synthesized by the Suzuki-Miyaura coupling reaction between 1, 3, 6, 8-tetrabromopyrene and boronate ester-terminated oligothiophenes in the presence of a palladium catalyst. Purification of **1** and **2** was accomplished by column chromatography followed by recycling preparative HPLC and were unambiguously characterized by means of matrix-assisted laser desorption/ionization time-of-flight mass spectra (MALDI-TOF-MS), analytical HPLC, and ^{1}H and ^{13}C NMR. Analysis of **1** and **2** by MALDI-TOF-MS and HPLC showed no signs of products with defects and confirmed that the coupling of the four oligothiophenes with the focal pyrene core was complete. The peripheral alkyl chains in **1** and **2** provide good solubility in organic solvents such as $CHCl_3$, toluene, n-hexane, and chlorobenzene, and the solubility in $CHCl_3$ is above 0.1 g/ mL at 20 °C. Furthermore, the spin-coating process on the glass and quartz substrates resulted in good film forming properties for the synthesized compounds. Good solubility and film forming properties are essential in the fabrication of devices using solution processes.

2-2-2 Optical and Electrochemical Properties

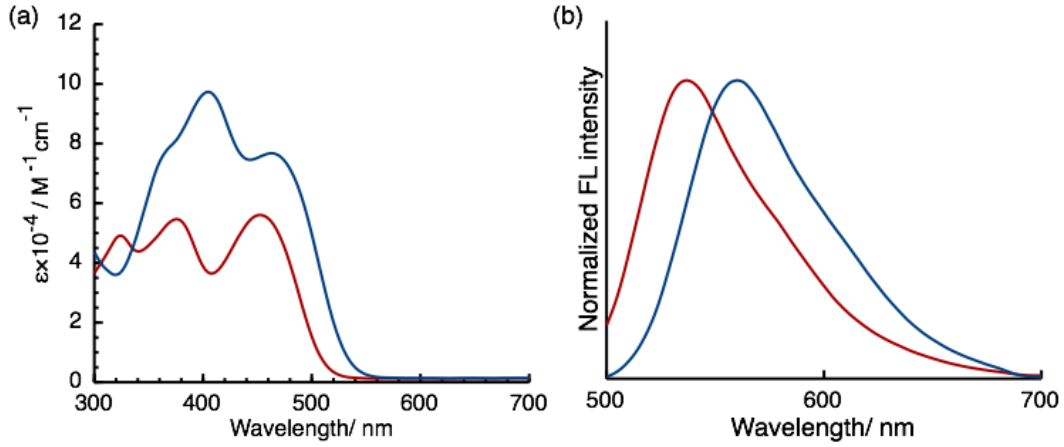

Figure 1. Absorption (a) and Fluorescence (b) spectra of **1** (red) and **2** (blue) in $CHCl_3$.

Figure 1 shows absorption and fluorescence spectra of **1** and **2** in $CHCl_3$ (ca.10^{-5} M), and absorption maxima (λ_{max}), absorption extinction coefficients (ε), and emission maxima (λ_{em}) are listed in Table 1. The positions of absorption and fluorescence peaks shifted to longer wavelengths with increased oligothiophene length, suggesting the formation of a larger π-conjugation system through the pyrene core.[21] Moreover, **2** displayed almost double ε values compared with **1**. The wide absorption range and high ε value of **2** is anticipated to efficient capturing of photon in solar cell devices.

The energy gap between the highest occupied molecular orbital (HOMO) of the donor and the lowest unoccupied molecular orbital (LUMO) of the acceptor correlate with the potential output of the devices. The HOMO/LUMO energy levels and corresponding band gaps of **1** and **2** were determined by cyclic voltammetry in combination with differential pulse voltammetry in CH_2Cl_2 solution. To determine the first oxidation potentials (E_{ox}) of **1** and **2** in solutions, cyclic voltammetry measurements were performed in CH_2Cl_2 containing 0.1 M tetrabutylammonium hexafluorophosphate ($TBAPF_6$) as a supporting electrolyte. The cyclic voltammograms of **1** and **2** reveal a reversible one-electron oxidation at 0.64 and 0.46 V vs ferrocene/ferricenium redox couple (Fc/Fc^+), respectively (Table 1). The observed oxidations of **1** and **2** are attributable to the oxidation of oligothiophene units.[21] The HOMO energy levels of **1** and **2** were estimated to be −5.21 and −5.07 eV from the onset oxidation potential values calibrated by the Fc/Fc^+ redox potential vs vacuum. The LUMO energy levels for 1 and 2, estimated from the HOMO energy levels and the onset of the optical energy gap (E_{0-0}), are evaluated to be −2.73 and −2.71 eV. The HOMO energy level of **2** is higher than that of **1**, whereas the LUMO energy level of **2** is almost the same as that of **1**. The LUMO energy levels of **1** and **2** are higher than those of $PC_{61}BM$ and $PC_{71}BM$, revealing sufficient driving force for efficient charge separation after photoexcitation. The disk-shaped molecules **1** and **2** having oligothiophenes are expected to be a suitable candidate for electron donor components in BHJ solar cells with $PC_{61}BM$ or $PC_{71}BM$.

Table 1. Absorption and electrochemical properties of **1** and **2**.

Compound	Solution		Film		$E_{1/2}$ / V (vs Fc/Fc^+)[d]
	λ_{max} /nm ($\varepsilon \times 10^4$ /M^{-1} cm^{-1})[a]	λ_{abs}^{max} (nm)[b]	λ_{abs}^{max} (nm)[c]	λ_{abs}^{max} (nm)[c]	
1	376 (5.24), 453 (5.37)	537	390, 472	624	5.21
2	405 (9.54), 463 (7.41)	560	438, 501	635	5.07

[a] In $CHCl_3$, [b] In degassed $CHCl_3$. [c] Deposited onto quartz substrate by spin-coating technique from $CHCl_3$ solution. [d] Measured in degassed CH_2Cl_2 containing 0.1 M $TBAPF_6$ at 295 K, scan rate = 100 mV/s.

2-2-3 Self-assembled Properties

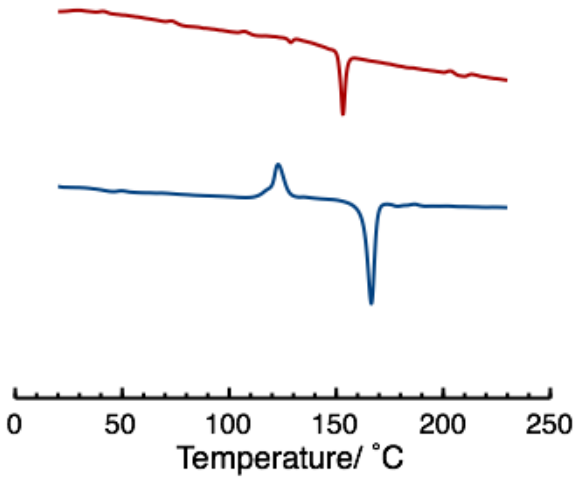

Figure 2. DSC diagrams for second heating of 1 (red) and 2 (blue) at 10˚C/ min.

Pyrene-containing molecules can organize into highly anisotropic and ordered structures through intermolecular π–π stacking.[22–24] The self-organizing materials tend to eliminate structural and electronic defects by self-healing, and their fluidity allows for easy preparation of thin films. The absorption and fluorescence spectra of thin films were broadened and red-shifted compared to those in solution (Table 1). These spectral changes can be ascribed to the formation of molecular

aggregates in the thin film.[25,26] The thermotropic behaviours of **1** and **2** have been investigated by means of differential scanning calorimetry (DSC), thermogravimetric analysis (TGA), and temperaturecontrolled polarizing optical microscopy (TPOM). Additional characterization of the organized structures was performed by powder X-ray diffraction (XRD). The DSC traces of **1** and **2** showed one endothermic peak at 155 and 172 °C (Figure 2).

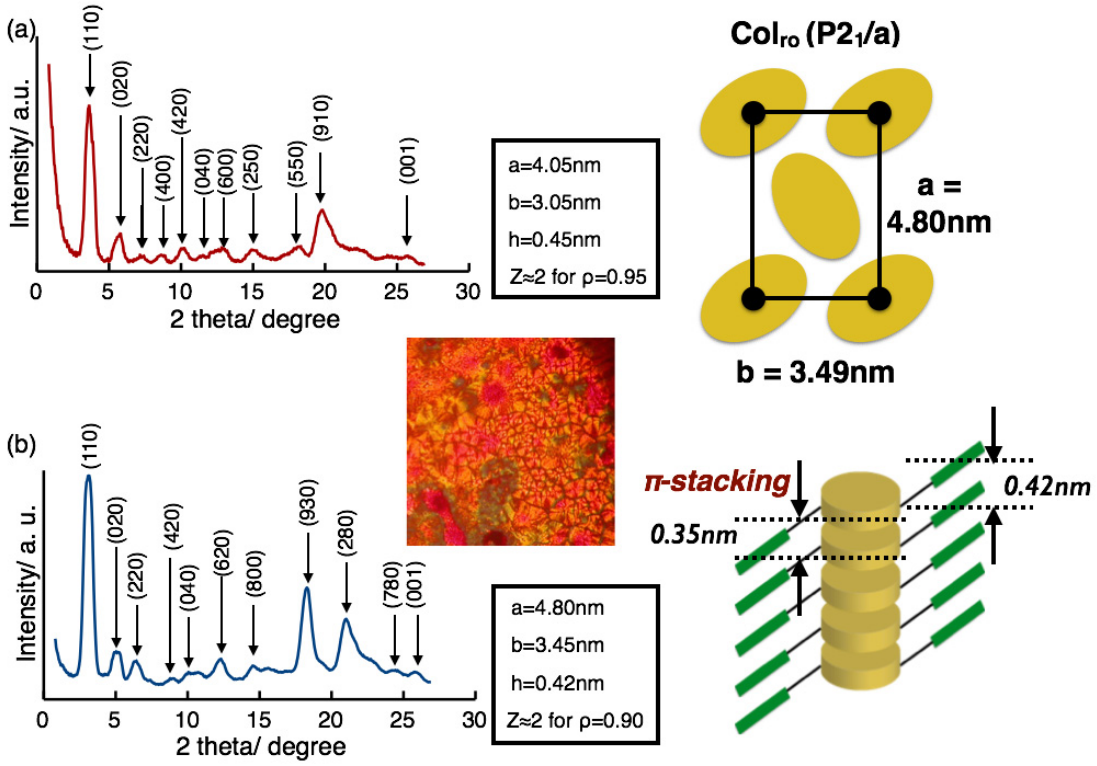

Figure 3. Temperature-controlled XRD pattern of **1** (a) and **2** (b) at 100 ˚C and 170 °C. Polarized optical micrograph of **2** at 150 °C after cooling form the isotropic phase (inset).

The XRD patterns of **1** and **2** displayed many reflections in the wide angle region. Weight losses in the TGA analysis of **1** and **2** started at 304 °C. On the basis of these results, we attribute the transition in the DSC measurements to the melting point. When **1** and **2** are slowly cooled down from the melting points, they form liquid-crystalline domains as shown in Figure 3a. The XRD pattern of **2** at 150 °C

attributed to rectangular columnar liquid crystalline Col_{ro} ($P2_1/a$). The distance of 0.34 nm is consistent with the stacking distance among pyrene units of the liquid-crystalline hexagonal columnar phase of pyrene-based molecules reported by Hayer et al.[27]

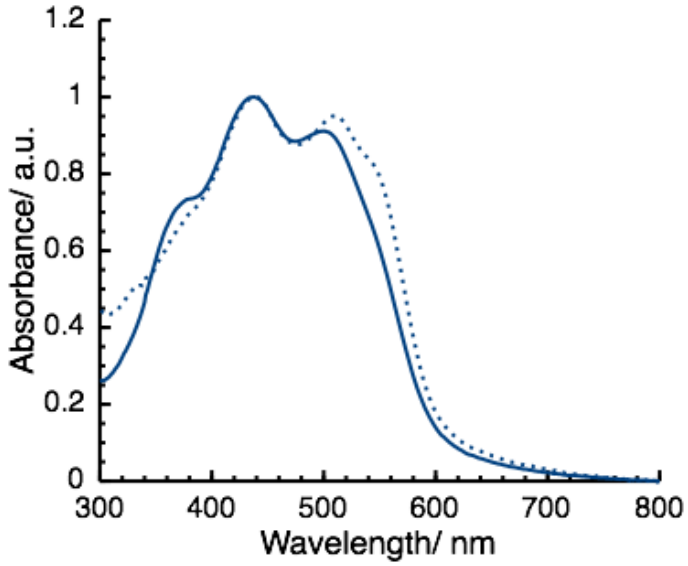

Figure 4. Absorption spectra of a thin film of **2** before (solid line) and after annealing at 150 °C for 10 min (dotted line).

The absorption spectrum of the thin film of **2** after annealing at 150 °C showed a new shoulder peak at 560 nm, which is indicative of intermolecular aggregation of the oligothiophene units in **2** (Figure 4).[25,26] In contrast, the spectrum of the thin film of **1** remained unaltered after the annealing. From these results, we concluded that the pyrene-cored compounds **1** and **2** having oligothiophene units can organize into ordered structures through π-orbital associations in the solid state.

2-2-4 Photovoltaic Properties

The active layers in the BHJ solar cells compose the interpenetrating bicontinuous network structures of an electron donating molecules and an electron

accepting fullerene derivatives.[1, 2] Control of the phase-segregation structure in the blended active layers is an important factor in enhancing the PCE of BHJ solar cells.

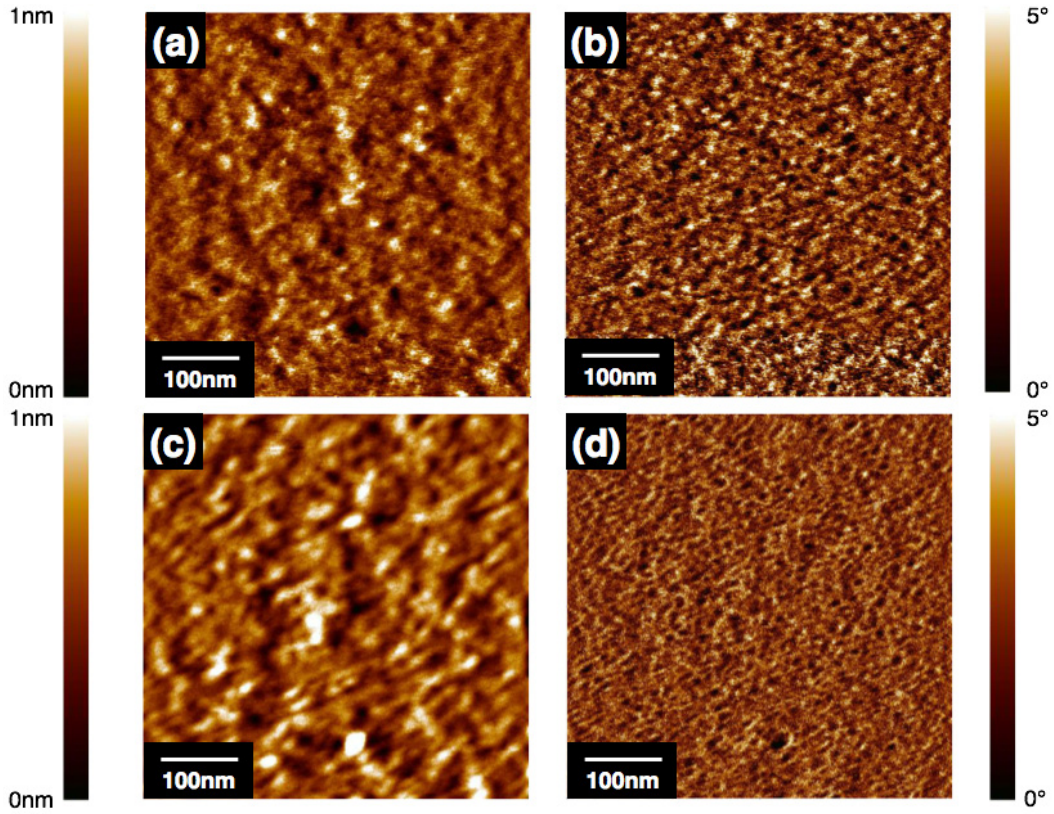

Figure 5. Tapping-mode AFM height and phase images (500×500 nm^2) of **1**/ $PC_{71}BM$ (1:5) (a, b) and **2**/$PC_{71}BM$ (1:4) (c, d) blended film.

The surface morphology of blended films was examined by tapping mode atomic force microscopy (AFM). The topographic and phase AFM images of a thin blended film composed of **2** and $PC_{71}BM$ (**2**:$PC_{71}BM$ = 1:4 w/w) are shown in Figure 5. The samples were prepared by spin coating of $CHCl_3$ solution of **2** and $PC_{71}BM$ on a glass substrate and the resulting thin films were annealed at 150 °C for 10 min under an Ar atmosphere. The surface morphology of the annealed film is very smooth with an average surface roughness of 1.2 nm. Phase images provide information about donor and acceptor distribution in active layers.[28] The phase image in Figure 3b reveals the presence of two domains having different material stiffness. The two domains can be assigned to the acceptor-rich domain and donor-rich domain. The

AFM image indicates that **2** has a good miscibility with $PC_{71}BM$ in the blended films, and that the spontaneous phase-segregation process in the mixed layer can form a bicontinuous network structure, which acts as percolation channels for the efficient carrier collection within the active layer of BHJ solar cells. The XRD pattern of blended films stayed unchanged as compared with those of **2**, and additional broad diffractions corresponding to neat C_{60} samples appeared around 0.8 nm.[29] Pyrene-cored compounds retain ordered structures within the phasesegregated films. The blending with fullerene derivatives does not affect the ordered structures in the donor domains composed of **1** or **2**, and phase segregation between the organic donors and the fullerene derivatives has occurred in the thin films.

SM BHJ solar cells were fabricated using **1** and **2** as the electron donor materials and fullerene derivatives as the electron acceptor materials through the conventional spincoating process. The cleaned tin-doped indium oxide (ITO)- coated glass anode was modified by spin-coating on poly(3,4-ethylenedioxythiophene):polystylenesulfonate (PEDOT:PSS) as a hole-extraction/electron-blocking layer with 40 nm thickness. The active layer was deposited from the mixed $CHCl_3$ solutions onto the PEDOT:PSS modified ITO anodes in the argon-filled glovebox ($[O_2] < 0.1$ ppm and $[H_2O] < 0.1$ ppm), and the thickness was typically 50 nm. After spincoating, the resulting active layer was annealed at 150 °C for 10 min. TiOx on the blended active layer has been used as an electron collection layer in the BHJ solar cells.[30] Finally, aluminum cathode was deposited through a shadow mask by thermal evaporation under vacuum.

The effect of different compositions between **2** and $PC_{61}BM$ was investigated and device performance parameters are summarized in Table 2. The device fabricated from the mixed solution with **2**: $PC_{61}BM$ composition of 1: 3 w/w showed a PCE of 1.1%, with a shortcircuit current (J_{sc}) of 4.0 mA cm^{-2}, an open circuit voltage (V_{oc}) of 0.78 V and a fill factor of 36%. After increasing the **2**: $PC_{61}BM$ composition ratio to 1:4, the PCE increased to 1.7%. The device shows a drop in PCE value as the fullerene loading is further increased. Our optimized devices based on **1** and **2** require the high content of n-type fullerenes.

Table 2. Summary of device parameters of SM BHJ solar cells based on mixed active layers composed of self-organized diskshaped donors **1** and **2** and PCBMs with different composition ratios.

Active layer (weight ratio)	Thickness (nm)	J_{sc}/mA cm^{-2}	V_{oc} /V	*FF*	PCE /%	IPCE$_{max}$ /%
1/ $PC_{61}BM$ (1:4)	50	3.19	0.76	0.3	0.7	43
1/ $PC_{61}BM$ (1:5)	50	3.81	0.88	0.35	1.2	50
1/ $PC_{61}BM$ (1:6)	50	3.27	0.78	0.32	0.8	48
2/ $PC_{61}BM$ (1:3)	50	3.99	0.78	0.36	1.1	43
2/ $PC_{61}BM$ (1:4)	50	5.7	0.8	0.38	1.7	63
2/$PC_{61}BM$ (1:5)	50	4.01	0.82	0.36	1.2	43
1/ $PC_{71}BM$ (1:5)	50	6.90	0.83	0.36	2.2	62
2/ $PC_{71}BM$ (1:4)	50	8.84	0.83	0.35	2.6	84
P3HT/ $PC_{61}BM$ (2:1)	70	7.50	0.61	0.61	2.8	67

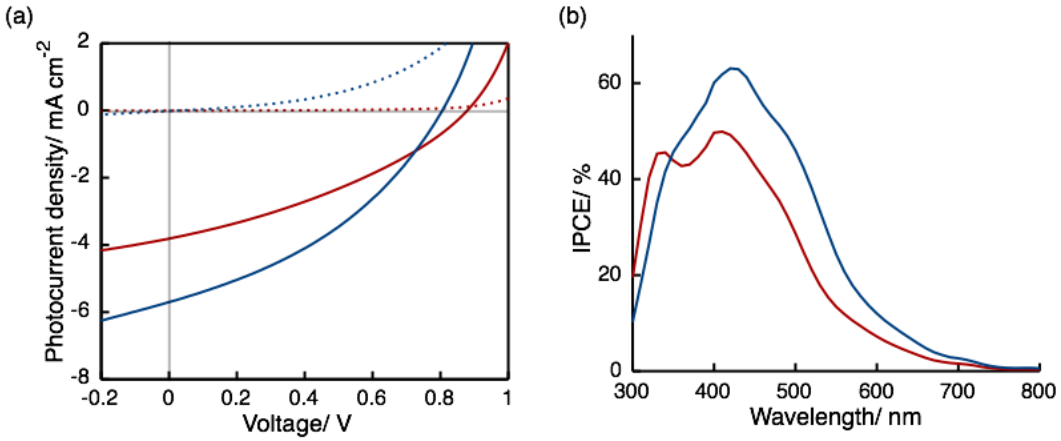

Figure 6. (a) Photocurrent voltage curve obtained with SM BHJ solar cells based on **1**/$PC_{61}BM$ (1:5 w/w, red line) and **2**/$PC_{61}BM$ (1:4 w/ w, blue line) blended active layers under a standard global AM 1.5 solar condition (solid line) and dark current (dotted line). (b)Incident photon-to-current conversion efficiency spectrum based on SM BHJ solar cells based on **1**/$PC_{61}BM$ (1:5 w/w, red line) and **2**/$PC_{61}BM$ (1:4 w/w, blue line) blended active layers.

Figure 6a shows the *J*−*V* curves of BHJ solar cells fabricated using **1** and **2** with $PC_{61}BM$. The J_{sc} value of the **2**/$PC_{61}BM$ device is higher than that of the **1**/$PC_{61}BM$. The incidentphoton to current conversion efficiency (IPCE) spectra followed the absorption feature of oligothiophene-substituted pyrene and $PC_{61}BM$, as shown in Figure 6b. The IPCE values of the **2**/$PC_{61}BM$ device are higher than those of **1**/$PC_{61}BM$ in all visible light regions. The IPCE difference between **1** and **2** is due to the wider absorption spectral range and the higher ε value of **2** relative to **1**. The V_{oc} value of the **2**/$PC_{61}BM$-based device is slightly lower than that of the **1**/$PC_{61}BM$. The V_{oc} of BHJ solar cells depends on the energy gap between the donor HOMO level and the acceptor LUMO level.[31] The energy gaps of 1.1 and 1.0 eV for **1**/$PC_{61}BM$ and **2**/$PC_{61}BM$ agreed with the difference in V_{oc} values for the devices.

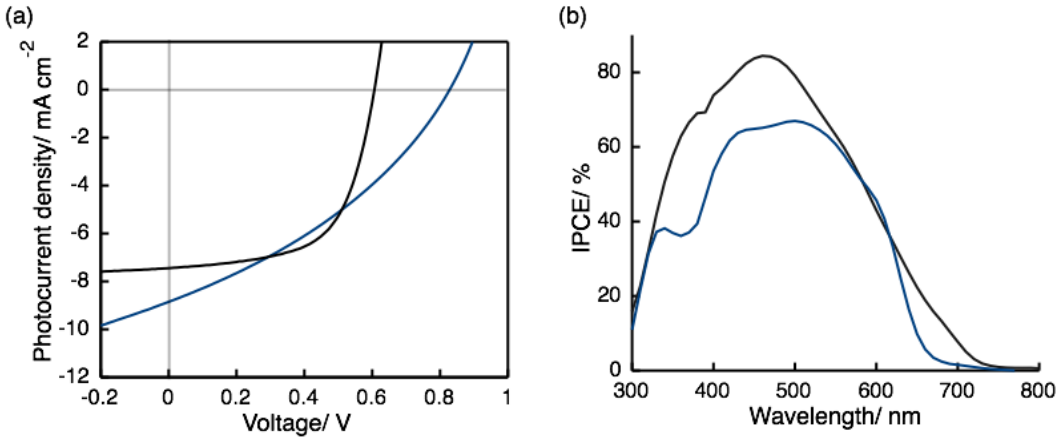

Figure 7. (a) Photocurrent voltage curve obtained with SM BHJ solar cells based on **2**/$PC_{71}BM$ (1:4 w/w, blue line) and P3HT/$PC_{61}BM$ (2:1 w/w, red line) blended active layers under a standard global AM 1.5 solar condition. (b) Incident photon-to-current conversion efficiency spectrum based on SM BHJ solar cells based on **2**/ $PC_{71}BM$ (1:4 w/w, blue line) and P3HT/$PC_{61}BM$ (2:1 w/w, red line) blended active layers.

Figure 7 shows the *J*−*V* and IPCE characteristics of a **2**/ $PC_{71}BM$ device (**2**: $PC_{71}BM$ composition ratio =1: 4 w/w). The J_{sc} value was improved significantly by changing from $PC_{61}BM$ to $PC_{71}BM$. The PCE of the **2**/$PC_{71}BM$ device was 2.6% under one sun condition, and the device exhibited a maximum IPCE value of 84% at 480 nm (Table 2). The wider absorption range of $PC_{71}BM$ compared to $PC_{61}BM$ can

improve light harvesting in the solar cells. The PCE of the **2**/$PC_{71}BM$ device is slightly lower than that of a poly(3- hexylthiophene) (P3HT)/$PC_{61}BM$ device. While the HOMO level of P3HT (−5.06 eV) is almost the same as that of **2**, the V_{oc} value of the **2**/$PC_{71}BM$ device (V_{oc} = 0.83 V) is higher than that of the P3HT/$PC_{61}BM$ device (V_{oc} = 0.61 V). Several organic donor materials for SM BHJ solar cells also showed higher V_{oc} values than the P3HT/$PC_{61}BM$ device.[4–9] The lower fill factor (FF) value in the **2**/$PC_{71}BM$ device indicates the poor balance of charge carrier mobilities in the phase segregated active layer.

2-3 Conclusions

In summary, we have presented simple molecular disks functionalized with lengthy oligothiophene units for the molecular component of SM BHJ solar cells. The optical and electronic properties of molecular disks can be tuned by changing the length of oligothiophenes. Molecular disks possessing peripheral alkyl chains can organize into organized structures through intermolecular π−π interactions, as we are able to conclude from absorption spectral changes in thin films, DSC, TPOM, and XRD. The pyrene core within the molecular disks was employed as the scaffold for molecular organization. A spontaneous phase-segregation process between molecular disks and fullerene derivatives formed bicontinuous network structures confirmed by AFM measurement. The formation of these structures is favorable for achieving efficient charge transport after photoexcitation. The SM BHJ solar cells fabricated with the molecular disks as electron donor components exhibited a good performance achieving PCE of 2.6%. The high IPCE value above 80% at the absorption maximum of 2 indicated an almost complete conversion of photon at this wavelength into electron. The further molecular designing of molecular disks can enhance the PCE values of solution-processed BHJ solar cells by optimizing the organized structures of donors for efficient charge mobility in the active layers, as well as expanding absorption ranges of organic donors to enhance their light-harvesting properties.

2-4 Experimental Section

2-4-1 General

NMR spectra were recorded on a Bruker AVANCE 400 FT NMR spectrometer at 399.65 and 100.62 MHz for ^{1}H and ^{13}C in $CDCl_3$ solution. Chemical shifts are reported relative to internal TMS. UV−Vis spectra were measured on a JASCO V-650. MALDI-TOF mass spectra were obtained on a Bruker autoflex with dithranol as matrix. The optical textures were studies a Nikon polarizing microscope equipped with a Mettler Toledo FP82 hot stage. The transition temperatures were measured by differential scanning calorimetry with a SII DSC 6200 operated at a scanning rate of 10 °C min^{-1} on heating and cooling. The apparatus was calibrated with indium as standard. The XRD patterns were obtained with a Rigaku XRD-DSC with Cu Kα radiation. Atomic force microscopy images were acquired in noncontact mode by a JEOL JSPM-5400 system. The samples for AFM were prepared by the spin-coating of $CHCl_3$ solutions on quartz substrate. Cyclic voltammetric measurements were recorded on an ALS 700 potentiostat using a three cell electrode system with a Pt working electrode, a Pt counter electrode, and an Ag/AgCl reference electrode. $TBAPF_6$ was used as the electrolyte.

2-4-2 Materials

All chemicals were purchased from commercial suppliers and used without purification. P3HT was purchase from Aldrich (electronic grade) and used without any purification. 1,3,6,8-Tetrabromopyrene,[23, 32] 5′-hexyl-2,2′-bithiophene-5-boronic acid pinacol ester, and 5″-hexyl-2′,2″:5″,2′-terthiophene-5-boronic acid pinacol ester were synthesized by standard procedures. Column chromatography was performed with silica gel (Wakogel C-200). Recycling preparative gel permeation chromatography was carried out by a JAI recycling preparative HPLC using $CHCl_3$ as an eluent. Analytical thin layer chromatography was performed with commercial Merck plates coated with silica gel 60 F254 or aluminum oxide 60 F254. The purities

of target compounds were confirmed by NMR, MALDI-TOF-Ms and analytical HPLC (column: Inertsil C18 (GL Science Inc.), eluent: $CHCl_3$, purity was determined by the ratio between the peak area of compound and the total peak area).

1: A solution of 1, 3, 6, 8-tetrabromopyrene (0.1 g, 0.19 mmol), 5′-hexyl-2,2′-bithiophene-5-boronic acid pinacol ester (0.57 g, 1.54 mmol) and $Pd(PPh_3)_4$ (57 mg, 49 μmol) in toluene (12.5 mL), ethanol (4.0 mL) and 2.0 M K_2CO_3 aqueous solution (2.5 mL) was stirred at 120 °C for 48 h under nitrogen. After cooling to room temperature, the reaction mixture was poured into water, extracted with CH_2Cl_2. The organic layer was dried over magnesium sulfate and the solvent was evaporated. The residue was purified by column chromatography on silica gel by eluting with CH_2Cl_2 and recycling preparative HPLC to give **1** as orange solid (0.23 g, yield 84%). ^{1}H NMR (400.13 MHz, $CDCl_3$): δ (ppm) = 8.58 (s, 4H, Ar*H*), 8.23 (s, 2H, Ar*H*), 7.28 (d, *J* = 3.6 Hz, 4H, Ar*H*), 7.22 (d, *J* = 3.6 Hz, 4H, Ar*H*), 7.06 (d, *J* = 3.6 Hz, 4H, Ar*H*), 6.72 (d, *J* = 3.6 Hz, 4H, Ar*H*), 2.82 (t, *J* = 7.6 Hz, 8H, -CH_2-), 1.71 (m, 8H, -CH_2-), 1.37 (m, 24H, -CH_2-), 0.91 (t, *J* = 6.6 Hz, 12H, -CH_3); ^{13}C NMR ($CDCl_3$, 100.61 MHz): δ (ppm) = 145.7, 140.0, 139.3, 134.6, 129.6, 129.0, 128.9, 125.7, 124.9, 123.6, 123.5, 31.6, 30.2, 28.8, 22.6, 14.1. MALDI-TOFMs: m/z = 1194 (M+H, 100%), Calcd for $C_{72}H_{74}S_8$. Anal. Calcd for $C_{72}H_{74}S_8$: C, 72.31; H, 6.24. Found: C, 72.4; H, 6.3. Purity (HPLC) > 99%.

2: Compound 2 was synthesized from 1,3,6,8-tetrabromopyrene and 5″-hexyl-2′,2″:5″,2′-terthiophene-5-boronic acid pinacol ester according to the same procedure of 1. Yield 73%. ^{1}H NMR (400.13 MHz, $CDCl_3$): δ (ppm) =8.49(s, 4H, Ar*H*), 8.21(s, 2H, Ar*H*), 7.26(m, 8H, Ar*H*), 7.12(m, 4H, Ar*H*), 7.02(m, 8H, Ar*H*), 6.71(d, *J* = 3.6 Hz, 4H, Ar*H*), 2.83(t, *J* = 7.6 Hz, 8H, -CH_2-), 1.72(m, 8H, -CH_2-), 1.39(m, 24H, -CH_2-), 0.93(t, *J* = 7.2 Hz, 12H, -CH_3); ^{13}C NMR ($CDCl_3$, 100.61 MHz): δ (ppm) = 145.6, 140.6, 138.5, 137.0, 135.3, 134.5, 129.1, 128.5, 124.8, 124.4, 123.9, 123.6, 123.4, 31.6, 30.2, 28.8, 22.6, 14.1. MALDI-TOF-Ms: m/z = 1522 (M+H, 100%), Calcd for $C_{88}H_{82}S_{12}$. Anal. Calcd for $C_{88}H_{88}S_{12}$: C, 69.34; H, 5.42. Found: C, 69.2; H, 5.4. Purity (HPLC) > 99%.

2-4-3 Device Fabrications

Indium tin oxide (ITO) patterned glass substrates were cleaning with sonication in neutral detergent, distilled water, acetone and 2-propanol. The substrates were dried and apply UV−O3 treatment for 30 min. Electron blocking layer were prepared by spin-coated the PEDOT:PSS (H. C. Starck) with a thickness of 40 nm. The substrates were baked at 200 °C for 30 min. A solution containing a mixture of pyrene-cored donors and fullerene derivatives in chloroform were spin-coated onto the PEDOT: PSS layer and apply thermal annealing treatment at 150 °C for 10 min in the argon filled globe box. Titanium oxide solution was spin-coated onto the active layer then place in air for 30 min.28 The counter electrode of aluminum was prepared by thermal deposition with a thickness of 100 nm. Current density−voltage (J−V) characteristics were measured using a Keithley 2400 Source Measure Unit. Performance of BHJ solar cells devices was measured under one-sun conditions (AM 1.5, 100 mW cm−2) by a solar simulator (XES-151S, Sanei electric Inc.).

2-5 References

1. S. Günes, H. Neugebauer, N. S. Sariciftci, *Chem. Rev*., **2007**, 107, 1324.
2. B. C. Thompson, J. M. J. Fréchet, *Angew. Chem., Int. Ed*., **2008**, 47, 58.
3. L. Dou, J. You, J. Yang, C-C. Chen, Y. He, S. Murase, T. Moriarty, K. Emery, Y. Yang, *Nat. Photonics*, **2012**, 6, 180.
4. P-L. T. Boudreault, A. Najari, M. Leclerc, *Chem. Mater*., **2011**, 23, 456.
5. B. Walker, C. Kim, T-Q. Nguyen, *Chem. Mater*., **2011**, 23, 470.
6. A. Mishra, P. Bäuerle, *Angew. Chem., Int. Ed*., **2012**, 51, 2020.
7. F. Silvestri, M. D. Irwin, L. Beverina, A. Facchetti, G. A. Pagani, T. J. Marks, *J. Am. Chem. Soc*., **2008**, 130, 17640.
8. Y. Matsuo, Y. Sato, T. Niinomi, I. Soga, H. Tanaka, E. Nakamura, *J. Am. Chem. Soc*., **2009**, 131, 16048.
9. B. Walker, A. B. Tamayo, X-D. Dang, P. Zalar, J. H. Seo, M. Tantiwiwat, T-Q. Nguyen, *Adv. Funct. Mater*., **2009**, 19, 3063.
10. Y. Sun, G. C. Welch, W. L. Leong, C. J. Takacs, G. C. Bazan, A. J. Heeger, *Nat. Mater*., **2012**, 11, 44.

11. W. Ma, C. Yang, X. Gong, K. Lee, A. J. Heeger, *Adv. Funct. Mater*., **2005**, 15, 1617.
12. B. R. Kaafarani, *Chem. Mater*., **2011**, 23, 378.
13. D. Adam, P. Schuhmacher, J. Simmerer, L. Haussling, K. Siemensmeyer, K. H. Etzbachi, H. Ringsdorf, D. Haarer, *Nature*, **1994**, 371, 141.
14. A. M. van de Craats, J. M. Warman, *Adv. Mater*., **2001**, 13, 130.
15. W. W. H. Wong, C.-Q. Ma, W. Pisula, C. Yan, X. Feng, D. J. Jones, K. Müllen, R. A. J. Janssen, P. Bäuerle, A. B. Holms, *Chem. Mater*., **2010**, 22, 457.
16. O. P. Lee, P. M. Beaujuge, C. H. Woo, T. W. Holcombe, J. E. Millstone, J. D. Douglas, M. S. Chen, J. M. J. Fréchet, *Adv. Mater*., **2011**, 23, 5359.
17. S. J. Kang, J. B. Kim, C. −Y. Chiu, S. Ahn, T. Schiros, S. S. Lee, K. G. Yager, M. F. Toney, Y.-L. Loo, C. Nuckolls, *Angew. Chem., Int. Ed*., **2012**, 51, 8594.
18. C.-Q. Ma, E. Mena-Osteritz, T. Debaerdemaeker, M. M. Wienk, R. A. J. Janssem, P. Bäuerle, *Angew. Chem., Int. Ed*., **2007**, 46, 1679.
19. C.-Q. Ma, M. Fonrodona, M. C. Schikora, M. M. Wienk, R. A. J. Janssen, P. Bäuerle, *Adv. Funct. Mater*., **2008**, 18, 3323.
20. Y. Liu, X. Wan, F. Wang, J. Zhou, G. Long, J. Tian, J. You, Y. Yang, Y. Chen, *Adv. Energy Mater.,* **2011**, 1, 771.
21. P. Bäuerle, *Adv. Mater*., **1992**, 2, 102.
22. T. M. Figueira-Duarte, K. Müllen, *Chem. Rev.*, **2011**, 111, 7260.
23. M. Uchiyama, Y. Watanabe, F. Araoka, J. Watanabe, H. Takezoe, G. Konishi, *Adv. Mater*., **2010**, 22, 4473.
24. J. N. Moorthy, P. Natarajan, P. Venkatakrishnan, D.-F. Huang, T. J. Chow, *Org. Lett*., **2007**, 9, 5215.
25. A. R. Murphy, P. C. Chang, P. VanDyke, J. Liu, J. M. J. Fréchet, V. Subramanian, D. M. DeLongchamp, S. Sambasivan, D. A. Fisher, E. K. Lin, *Chem. Mater*., **2005**, 17, 6033.
26. S. Samitsu, T. Shimomura, S. Heike, T. Hashizume, K. Ito, *Macromolecules,* **2008**, 41, 8000.
27. A. Hayer, V. de Halleux, A. Köhler, A. El-Garoughy, E. W. Meijer, J. Barberá, J. Tant, J. Levin, M. Lehmann, J. Gierschner, J. Cornil, Y. H. J. Geerts, *Phys. Chem. B*, **2006**, 110, 7653.
28. J. E. Slota, X. He, W. T. S. Huch, *Nano Today*, **2010**, 5, 231.

29. J. Guo, Y. Liang, J. Szarko, B. Lee, H. J. Son, B. S. Rolczynski, L. Yu, L. X. Chen, *J. Phys. Chem. B*, **2010**, 114, 742.
30. A. Hayakawa, O. Yoshiokawa, T. Fujieda, K. Uehara, S. Yoshikawa, *Appl. Phys. Lett*., **2007**, 90, 163517.
31. M. C. Scharber, D. Mühlbacher, M. Koppe, P. Denk, C. Waldauf, A. J. Heeger, C. J. Brabec, *Adv. Mater*. **2006**, 18, 789.
32. K. C. Stylianou, R. Heck, S. Y. Chong, J. Bacsa, J. T. A. Jones, Y. Z. Khimyak, D. Bradshaw, J. M. Rosseinsky, *J. Am. Chem. Soc*., **2010**, 132, 4119.

Chapter 3

Low Band Gap Disk-shaped Donors for Solution-Processed Organic Solar Cells

Abstract

Disk-shaped donors composed of a pyrene core, dithiophene linkers and rhodanine terminates were synthesized and their optical and electrochemical properties were investigated. The introduction of rhodanine terminal units into the pyrene-cored donors could effectively broaden the absorption spectrum and improve the molar absorption coefficient. The positions of dithiophene linkers in the pyrene core affected to their optical and electrochemical properties as well as the molecular ordering and carrier transport properties in solid state. In addition, length of peripheral alkyl chains in dithiophene linkers changed molecular ordering and carrier transport properties in solid state. The HOMO and LUMO energy levels of these materials were suitable for the donor component in BHJ solar cells with fullerene acceptor. The BHJ solar cells were fabricated by the solution process using mixed solutions of pyrene-cored donors with fullerene acceptors. The PCE values strongly depended on the structure of the donor. In addition, the shortening of the peripheral alkyl chain length in the dithiophene linkers improved the PCE due to its better hole-mobility in the film. A highest PCE was achieved an overall power conversion efficiency of 3.7% with a short-current density of 8.4mA/cm^2, open-circuit voltage of 1.09V, and fill factor of 41% under one sun condition.

3-1 Introduction

Organic photovoltaic devices (OPVs) based on thin films of organic semiconductors have been intensely investigated as a promising alternative of conventional silicon-based solar cells because of their potential for low-cost and scalable manufacturing through solution-based printable technologies on flexible substrates.[1,2] The performance of OPVs has been greatly improved by using bulk heterojunction (BHJ) architecture, which is an interpenetrating network with a large donor-acceptor interfacial area organized through a spontaneous phase-separation of donor and acceptor materials.[3,4] Controlling BHJ structure in the active layers allows a high interfacial area that optimizes the exciton dissociation as well as the efficient transport of generated charge carriers to the respective electrodes.[5]

A wide variety of π-conjugated oligomers and polymers have been designed and synthesized as light-harvesting donor materials for the solution-processed BHJ solar cells.[6-10] Compared to π-conjugated polymers, discrete and well-defined π-conjugated oligomers are advantageous because the nanostructures in the active layers of the BHJ solar cells can be precisely controlled. [11-20] Moreover, the optoelectronic properties of π-conjugated oligomers such as optical properties, charge carrier mobility, and energy levels can be tuned systematically by chemical functionalizations. To date, an overall power conversion efficiency (PCE) of around 8% has been achieved in solution-processed BHJ solar cells by blending active layers of low band gap donor oligomers with the fullerene derivative [6,6]-phenyl-C_{71}-butylic acid methyl ester ($PC_{71}BM$).[21] Recently, we reported on the performance of BHJ solar cells containing self-organized stacks of pyrene-cored donors.[22] Pyrene has been used as a molecular component of organic semiconductors for organic electronics.[23-25] Pyrene-cored donors with linear oligothiophenes were organized into one-dimensional stacks through intermolecular π-π interaction, and the π-π overlap within the stacks provided an efficient transport pathway for charge or energy.[22] However, PCEs of pyrene-cored donors with $PC_{71}BM$ was less than 3% due

to the limitation of light-harvesting area of active layers. Moreover, low fill factor of pyrene-cored donors are indicated that low crystalline nature in the active layer.[9, 10, 26]

The introduction of acceptor units in the donors gives strong absorption at a long wavelength owing to intramolecular charge transfer.[27,28] To expand the light-harvesting area of pyrene-cored donors for the solution-processed BHJ solar cells, we designed four pyrene-cored donors **1-4** terminated with rhodanine acceptor units, in which the pyrene core and rhodanine terminal units were linked with alkyl-substituted dithiophene π-conjugated linkers to form a conjugated backbone structure with strong charge transfer and broad absorption. The FF in BHJ solar cells can be influenced by a variety of factors including choice of electrodes, geminate recombination, and the competition between nongeminate recombination and charge collection.[29-31] Enhancement of the hole mobility of disk-shaped donors are one promising way to improve FF. The modification by varying the substitution at different positions of the pyrene ring allows the tuning of optical and electronic properties, and the molecular shape of pyrene derivatives affects the molecular packing in the solid state. We have investigated the relationship of the hole-mobility and BHJ solar cells properties using pyrene-cored donors. A PCE of 3.7% with an open-circuit voltage (V_{oc}) above 1.0 V was achieved for solution-processed BHJ solar cells using **4** with $PC_{71}BM$ under one-sun condition.

3-2 Results and Discussion

3-2-1 Synthesis of Pyrene-cored Donors

Four pyrene-cored donors **1-4** based on different substitution patterns of pyrene were synthesized through stepwise reactions from di- or tetrasubstituted pyrenes (Scheme 1). Linear 2,7-disubstituted donor **1** was synthesized by Suzuki-Miyaura coupling reaction of dithiophene derivative **6** with 2,7-bis(4,4,5,5-tetramethyl-1,3,2-dioxaborolan-2-yl) pyrene and the following Knoevenagel reaction with 3-ethylrhodanine. The other three donors **2-4** were prepared from 1,3-dibromo-7-*tert*-butylpyrene or 1,3,6,8-tetrabromopyrene. After the

formylation of terminal positions through a Vilsmeir-Hacck reaction, 3-ethylrhodanine units were introduced at the aldehyde terminates to give **2-4**. The rhodanine units have been used as an electron-deficient group in the low band gap organic semiconductors for BHJ solar cells.[20,21,32] The purity of the targeted compounds **1-4** for device fabrication was guaranteed by repeated column purifications, and checked by analytical HPLC and MALDI-TOF-Ms. All pyrene-cored donors exhibit a good solubility in organic solvents such as $CHCl_3$, toluene and chlorobenzene. The solubility of **1-4** in $CHCl_3$ or chlorobenzene is above 20mg/ml at 20^{o}C. Uniform thin films were formed by spin-coating of donor solutions on quartz substrates. Good solubility and film forming property of pyrene-cored donors are a prerequisite for solution-processed BHJ solar cells.

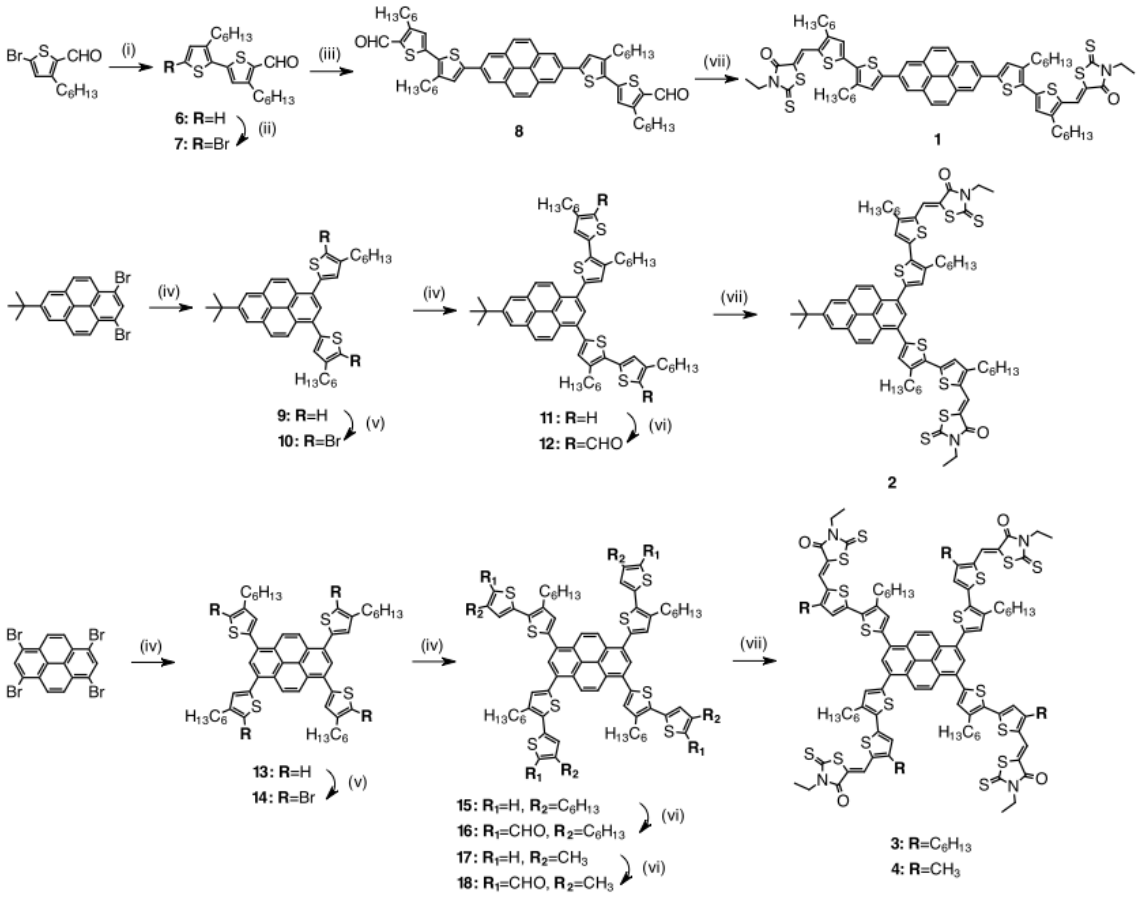

Scheme 1. Synthesis of pyrene-cored donors **1-4**. Reaction conditions: (i) 3-hexylthiophene-2-boronic acid pinacol ester, $Pd(PPh_3)_4$, THF/ K_2CO_3; (ii) NBS, $CHCl_3$/ AcOH; (iii) 2,7-Bis(4,4,5,5-tetramethyl-1,3,2-dioxaborolan-2-yl)pyrene, $Pd(PPh_3)_4$, toluene/ ethanol/ K_2CO_3; (iv) 4-hexylthiophene-2-boronic acid pinacol ester or 4-methylthiophene-2-boronic acid pinacol ester, $Pd(PPh_3)_4$, toluene/ ethanol/ K_2CO_3; (v) NBS, $CHCl_3$; (vi) $POCl_3$, 1,2-dichloroethane/ DMF; (vii) 3-ethylrhodanine, piperizine/ $CHCl_3$.

3-2-2 Optical and Electrochemical Properties

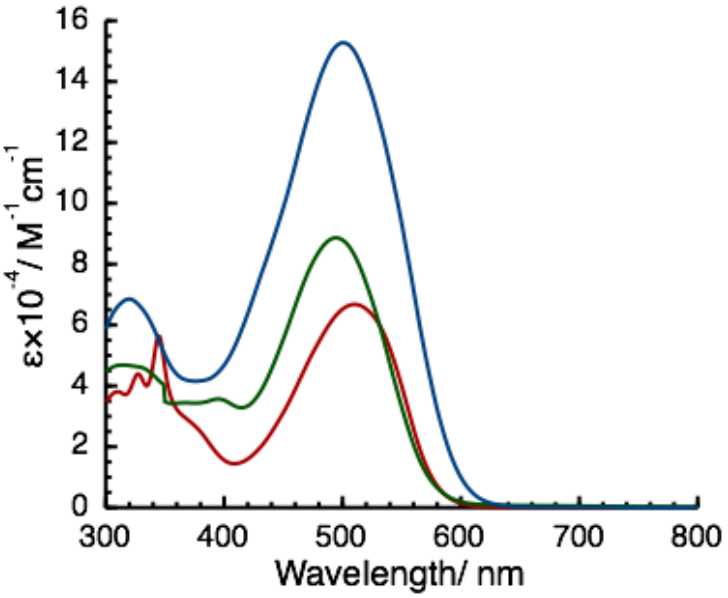

Figure 1. UV-Vis absorption spectra of **1** (red), **2** (green) and **3** (blue) in chloroform.

Table 1. Absorption, electrochemical, thermal, and hole-mobility data of **1-4**.

	Solution		Film	E_{ox} [c]	m.p.[d]	μ_h [e]
	λ_{max} /nm[a]	$\varepsilon\times10^{-4}$ /M^{-1} cm^{-1}	λ_{max} / nm[b]	/ V *vs.* Fc/Fc^+	/ °C	/ cm^2 V^{-1} s^{-1}
1	327, 345, 510	4.4, 5.6, 6.7	349, 534	0.71	286	1×10^{-4}
2	314, 395, 494	4.7, 3.5, 8.9	321, 502	0.76	160	1×10^{-4}
3	320, 501	6.9, 15.3	331, 526	0.56	181	1×10^{-5}
4	321, 502	6.0, 14.5	334, 530	0.57	234	6×10^{-5}

[a] Maximum of the absorption in $CHCl_3$. [b] Deposited onto quartz substrate by spin-coating technique from $CHCl_3$ solution. [c] Measured in degassed $CHCl_2$ containing 0.1M $TBAPF_6$ at 295K, scan rate =100mV/s. [d] Determined by DSC operated at a scanning rate of 10°C/min. [e] Determined from SCLC method using hole-only device with **1-4** films prepared by spin-coating from $CHCl_3$ or chlorobenzene solution.

Figure 1 shows the UV-Vis spectra of **1-3** in $CHCl_3$, and the absorption maxima (λ_{max}) and molar absorption coefficients (ε) of **1-4** are collected in Table 1. Compound **3** decorated with four 3-ethylrhodanine-terminated dithiophenes exhibits an absorption peak at 501 nm with ε value of 1.5 x $10^5 M^{-1}$ cm^{-1}. The absorption maxima of **3** exhibits a 48 nm red-shift compared to the pyrene-cored donor lacking rhodanine terminal units **5** (λ_{max}=453nm), and the e value of **3** was almost three times higher than that of **5**.[22] The introduction of electron accepting terminal units into the pyrene-cored donors could effectively broaden the absorption spectrum and improve the ε value. Furthermore, the position and number of side chains also affected the λ_{max} and ε values. The band gap of organic semiconductors can be compressed by applying the intramolecular charge transfer between electron-rich donors and electron-deficient acceptors.[27,28,33] The interaction between donor and acceptor units gives rise to an increased double bond character between these two units.

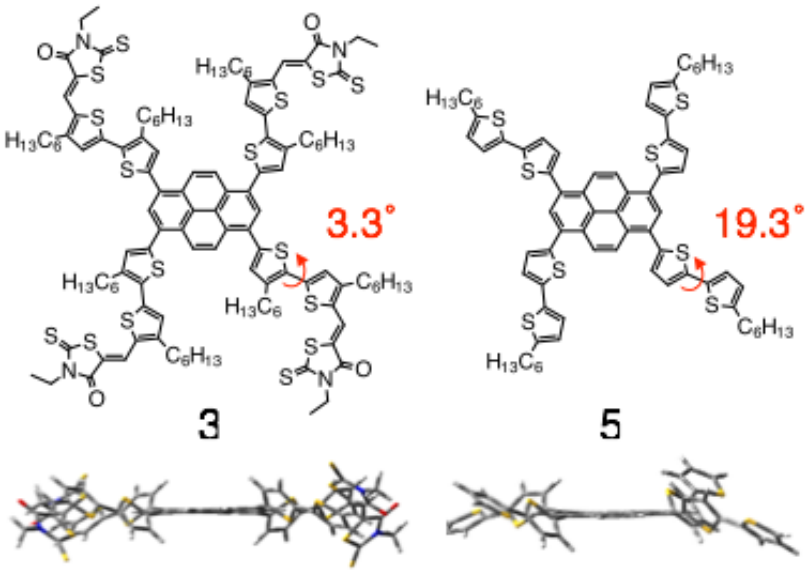

Figure 2. Optimized molecular geometries of **3** and **5** by DFT calculation with B3LYP 6-31G* level.

The dihedral angle between thiophene units in the optimized structure of **3** (3^o) is smaller than that in **5** (19^o), suggesting that the increase of double bond character between two thiophene units is caused by the introduction of rhodanine terminates (Figure 2). Broad absorption ranges and high ε values of

rhodanine-terminated donors are anticipated to efficient capturing of photon energy in solar cell devices.

The energy gap between the highest occupied molecular orbital (HOMO) of the donor and the lowest unoccupied molecular orbital (LUMO) of the acceptor correlate with the potential output of the devices. The HOMO energy levels of **1-4** were determined by cyclic voltammetry in combination with differential pulse voltammetry (DPV) in dry CH_2Cl_2 containing 0.1M tetrabutylammonium hexafluorophosphate ($TBAPF_6$) as a supporting electrolyte (Table 1). The cyclic voltammogram of **1-4** reveal reversible one-electron oxidation at 0.71, 0.76, 0.56 and 0.57V *vs.* ferrocene/ferrocenium redox couple (Fc/Fc^+). The HOMO energy levels of **1-4** were calibrated from the oxidation potentials determined from DPV (Table 1).[34]

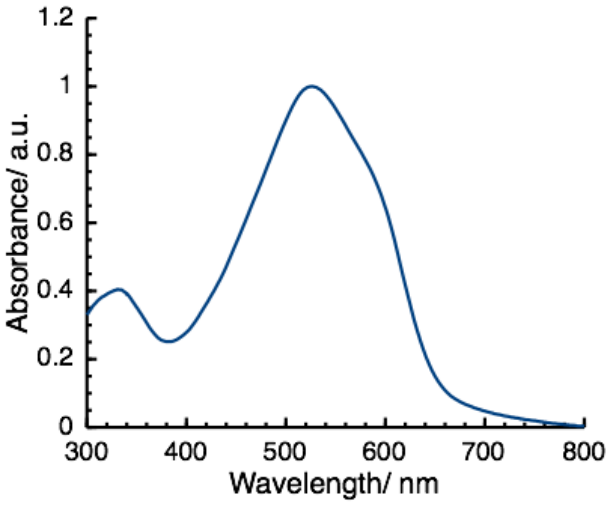

Figure 3. (a) Absorption spectra of spin-coated thin film of **3**.

The spin-coated film of **3** shows a broader absorption from 300-670nm and a red-shifted λ_{max} at 526nm with a vibronic shoulder peak at 600nm (Figure 3, Table 1). These spectral changes indicate π-π packing between the molecule backbones at the solid state.[35,36]

The LUMO energy levels for **1-4** are estimated from the HOMO energy levels and the optical energy gaps ($E_{0\text{-}0}$) determined from the onset of absorption bands of the thin films. Figure 4 shows the energy bad diagrams of **1-4** in relation to

the relative energy levels of fullerene derivatives. Whereas the HOMO level of rhodanine-terminated **3** is similar to that of **5**, the LUMO level of **3** is significantly stabilized through the electron accepting effect of rhodanine terminates. The LUMO energy levels of all pyrene-cored donors are still higher than those of [6,6]-phenyl-C61-butylic acid methyl ester ($PC_{61}BM$) and $PC_{71}BM$, revealing a sufficient driving force for electron transfer after photoexcitation.[1,2] Thus, the pyrene-cored donors **1-4** are expected to be a suitable candidate for the donor materials in BHJ solar cells with $PC_{61}BM$ or $PC_{71}BM$.

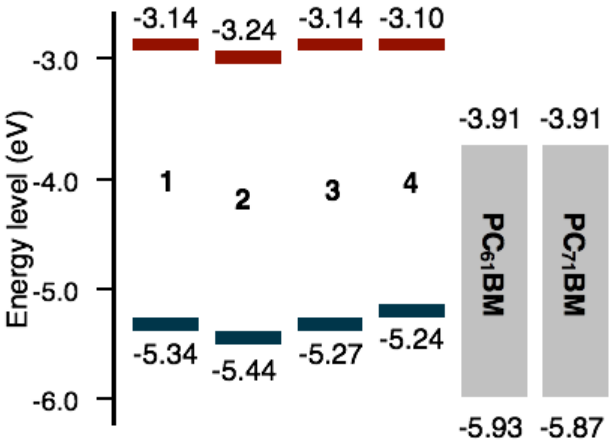

Figure 4. Energy diagrams of **1-4**, $PC_{61}BM$, and $PC_{71}BM$.

3-2-3 Thermal Properties

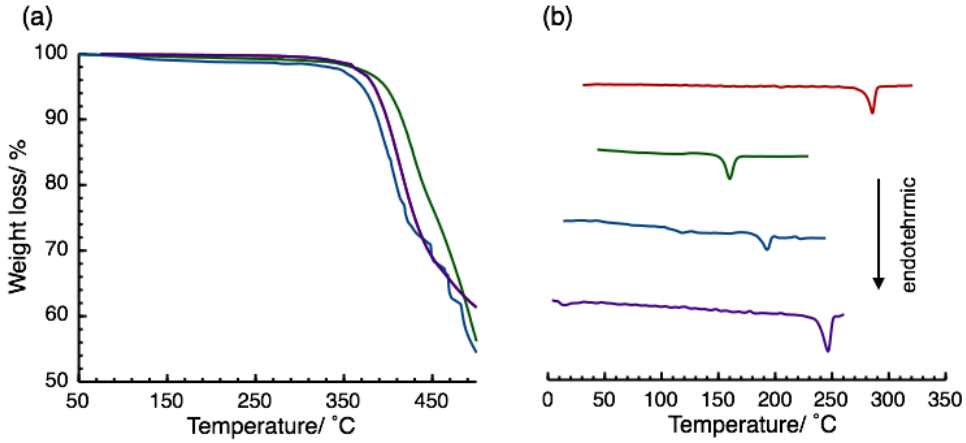

Figure 5. TGA (a) and DSC (b) profiles for **1** (red), **2** (green), **3**(blue) and **4**(purple) at scan rate of 10˚C/ min.

The thermal properties of **1-4** were characterized using themogravimetric analysis (TGA) and differential scanning calorimetry (DSC) (Figure 5). TGA analyses showed that all pyrene-cored donors **1-4** exhibit a good thermal stability with decomposition temperatures of above 350°C under an N_2 atmosphere. The DSC analyses of **1-4** revealed one endothermic peak, corresponding to the melting point (Table 1). The melting points of organic molecules are determined by factors including molecular symmetry, electric dipoles, and interaction energies.[37] The melting point of **4** is higher than that of **3**, revealing the increase of intermolecular interaction energy by shortening the alkyl chains of the outer thiophene units in the peripheral substituents.

3-2-4 Self-assembled Properties

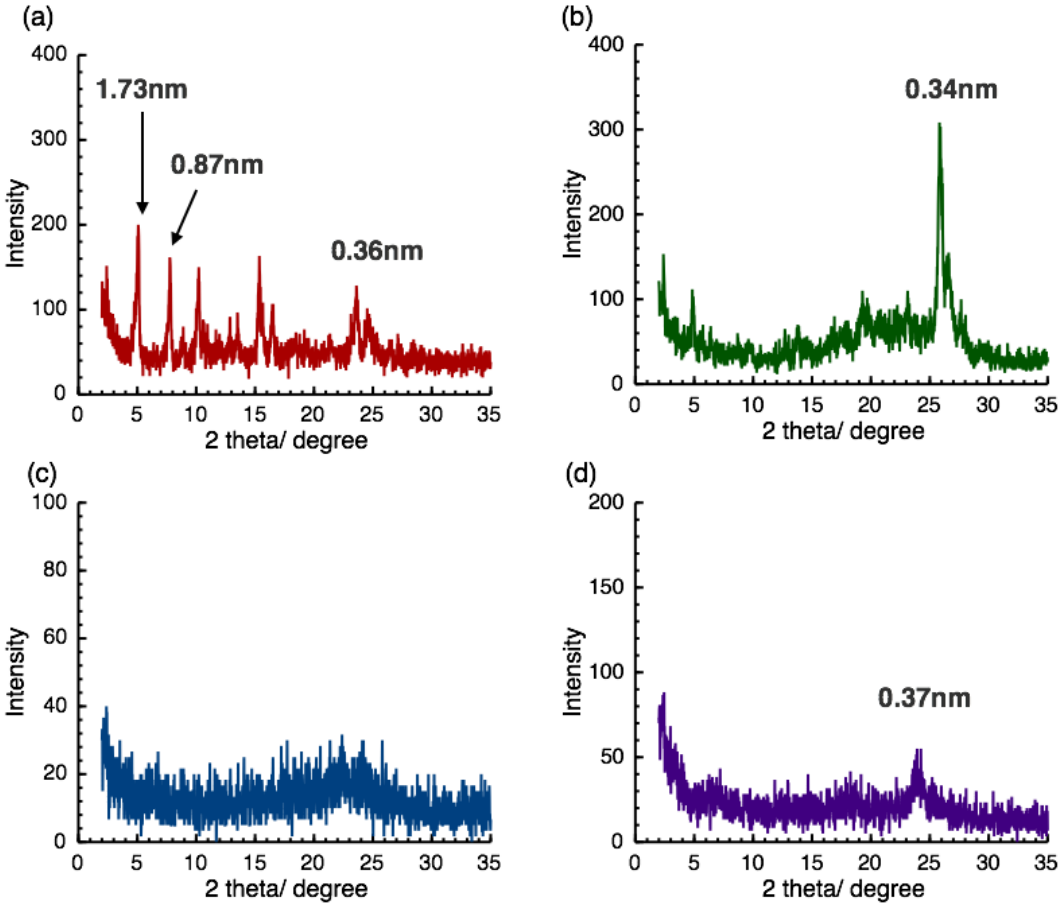

Figure 6. XRD patterns of **1**(a), **2**(b), **3**(c) and **4**(d) at RT.

The structural ordering of **1-4** was investigated by powdered XRD analyses (Figure 6). The reflection patterns of **1** showed several reflection peaks at 2θ=2-30°, indicating a high degree of crystallinity. In contrast, the XRD patterns of **2-4** did not provide any peaks at 2θ=2-15°. The films of **2** and **4** exhibited a sharp reflection peak at 0.37nm due to the stacking distance between rigid aromatic segments, suggesting the presence of long-range periodicity in stacks.

3-2-5 Hole-mobility of Disk-shaped Donor

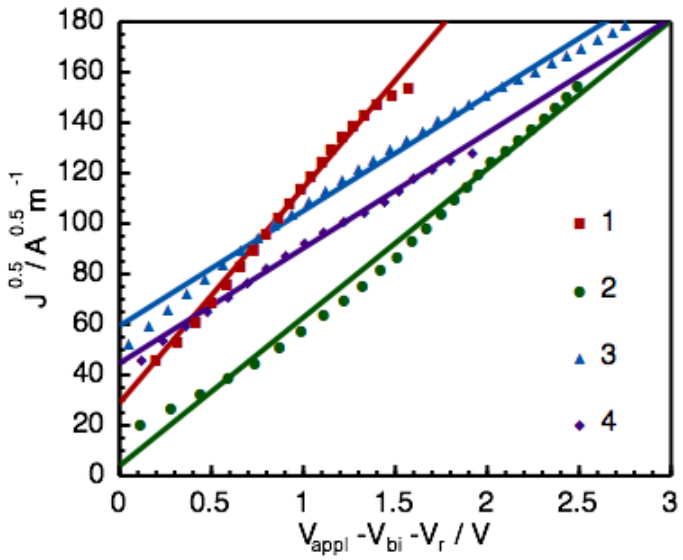

Figure 7. $J^{0.5}$-V plots for **1** (red), **2** (green), **3** (blue) and **4** (purple) hole-only devices under dark condition. The solid lines are fitted with the data points. Film thickness: **1**, 35nm; **2**, 50nm, **3**, 30nm; **4**, 45nm.

The hole mobilities of **1-4** in the thin films were evaluated by space charge limited current (SCLC) method (Figure 7, Table 2).[38-42] The hole mobility of **3** was ten times less than those of **1** and **2**, presumably due to the low degree of crystallinity of **3** as described in the XRD analyses. On the other hand, **4** showed a six times higher mobility compared to **3**, implying that the stacking provides a transport pathway for holes in the solid state.

3-2-6 Surface Morphology of Blended Films

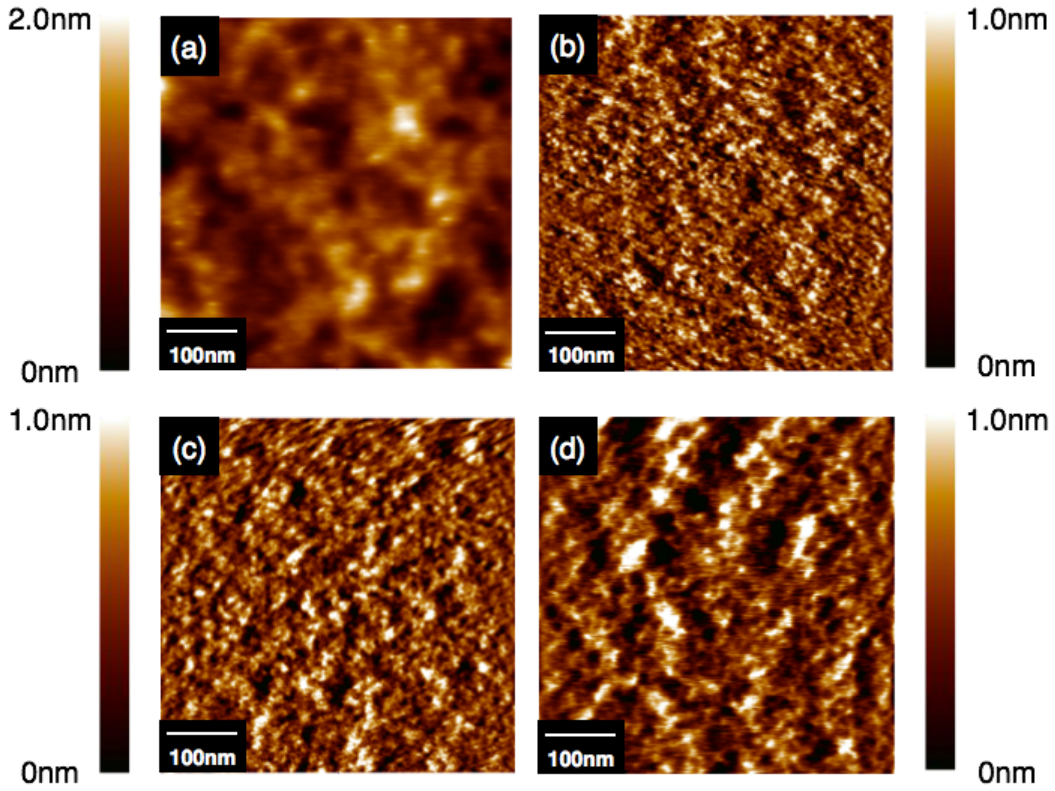

Figure 8. Tapping-mode AFM height images of **1-4** (a-d)/$PC_{61}BM$ blended film.

Control of the phase-segregation structure in the blended active layers is an important factor in enhancing the PCE of BHJ solar cells. The surface morphology of blended films was examined by tapping mode atomic force microscopy (AFM) (Figure 8).[11,13,15] The blended films were prepared by the spin coating from the chloroform solution of **1-4** and $PC_{61}BM$ on quartz substrates. The blended film of **1**/$PC_{61}BM$ showed large-sized domains with an average size above 50nm. The topography image of **2**/$PC_{61}BM$ comprises small domains less than 20 nm wide with a surface roughness (rms) of 0.27nm. The blended films of **3** or **4** with $PC_{61}BM$ are also smooth with an rms less than 1 nm. The AFM images indicates that **2-4** have a good miscibility with $PC_{61}BM$ in the blended films and the spontaneous phase-segregation process in the mixed layer can form a bicontinuous network structure, which acts as percolation channels for the efficient carrier collection within the active layer of BHJ solar cells.[3,4]

3-2-7 Photovoltaic Properties

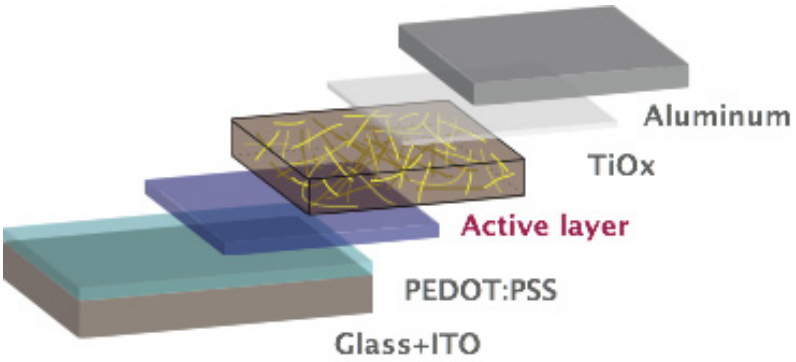

Figure 9. Device structure of BHJ solar cells.

BHJ solar cells were fabricated using **1-4** as the electron donor and $PC_{61}BM$ or $PC_{71}BM$ as the electron acceptor with tin-doped indium oxide (ITO)/ poly(3,4-ethylenedioxythiophene):polystyrene sulfonate (PEDOT:PSS)/ active layer/TiO_x/aluminium device structure using a solution process (Figure 9). The cleaned ITO was modified by spin-coating of PEDOT:PSS as a hole-extraction/electron-blocking layer with a 40nm thickness. The active layer was deposited from a chloroform solution onto the PEDOT: PSS modified ITO anodes in an argon-filled grove box, and the thickness was typically 60-70nm. The TiO_x layer was used as an electron-collection/hole-blocking layer in the BHJ solar cells. Finally, an aluminum cathode was deposited through a shadow mask by thermal evaporation under vacuum.

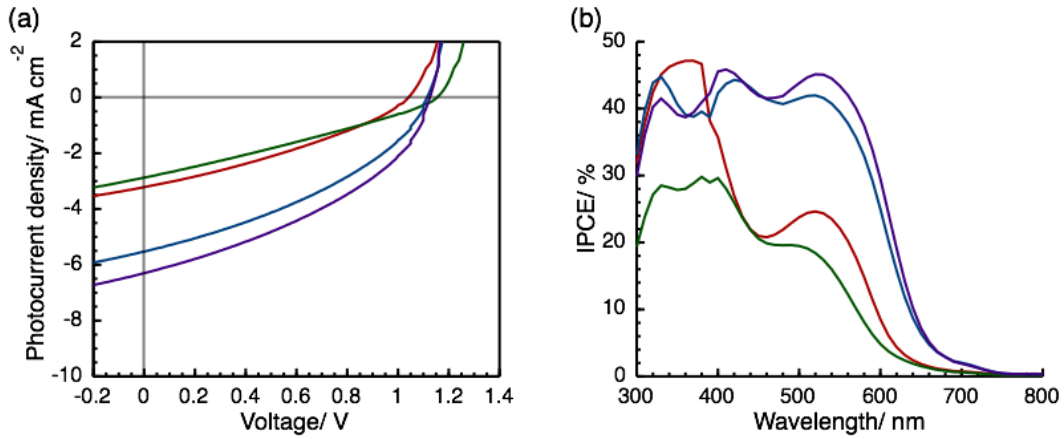

Figure 10. (a) Photocurrent voltage curve obtained with BHJ solar cells based on **1** (red), **2** (green), **3** (blue) and **4**(purple)/$PC_{61}BM$ blended active layers under a standard global AM 1.5 solar condition. b) Incident photon-to-current conversion efficiency spectrum based on **1** (red), **2** (green), **3** (blue) and **4** (purple)/$PC_{61}BM$ and blended active layers.

Table 2. Summary of device parameters of BHJ solar cells based on mixed active layers of **1-4** and P3HT/ PCBMs.

Active layer (weight ratio)	thickness /nm	V_{oc} / V	J_{sc} /mA cm^{-2}	*FF*	PCE / %
1/ $PC_{61}BM$ (1:2)	65	1.04	3.21	0.33	1.1
2/ $PC_{61}BM$ (1:4)	70	1.15	2.87	0.29	1.0
3/ $PC_{61}BM$ (1:4)	70	1.11	5.53	0.38	2.3
4/ $PC_{61}BM$ (1:2)	70	1.10	5.50	0.36	2.1
4/ $PC_{61}BM$ (1:3)	70	1.13	6.30	0.39	2.8
4/ $PC_{61}BM$ (1:4)	70	1.10	5.97	0.39	2.5
4/ $PC_{71}BM$ (1:3)	70	1.08	8.42	0.41	3.7
P3HT/ $PC_{61}BM$ (2:1)	90	0.65	8.38	0.67	3.7

The performances for all devices under AM 1.5G illumination at an intensity of 100 mWcm^{-2} are summarized in Figure 10 and Table 2. The cell performance of a poly(3-hexyl)thiophene (P3HT)/$PC_{61}BM$ device is provided as a benchmark. The effect of the different composition of **4**/ $PC_{61}BM$ was investigated (Table 2). The weight ratio of 1:2 w/w of **4**/$PC_{61}BM$ showed a PCE of 2.1% with a V_{oc} of 1.10V, short-current density (J_{sc}) of 5.50mA/ cm^2 and fill factor (*FF*) of 36%. When the composition ratio of **4**/$PC_{61}BM$ was changed to 1:3 w/w, the PCE increased to 2.8%. Further increase of composition ratio show a drop in the PCE value. The PCE value was in the order of **1** = **2** < **3** < **4** cells in the optimized composition ratios of donor/$PC_{61}BM$ (Figure 10, Table 2). The PCE values strongly depended on the structure of pyrene-cored donors. The Incident photon-to-current incident-photon to current conversion efficiency (IPCE) characteristics of **1-4**/ $PC_{61}BM$ devices are shown in Figure 10. When the number of the side chains is increased, the J_{sc} was greatly improved from 2.87 to 5.53 mA/ cm^2 with higher IPCE value of over 40% in 500 – 600nm. This is due to the higher absorption coefficients of **3** than **2** (Figure 1). The replacement of hexyl chains in **3** with methyl groups in **4** resulted in a higher PCE of 2.8 %. This higher PCE for **4** corresponds to higher J_{sc} values relative to **3**, which is believed to be due to its better hole mobility in stacking. The FF is determined by the series resistance (R_s) and shunt resistance (R_{sh}).[43] The R_s is closely related with the intrinsic resistance, morphology, and thickness of the active layer. On the other hand, R_{sh} is correlated with charge recombination and leakage current.[43] The FF of **3**/$PC_{61}BM$ devices is slightly higher than those of **1** and **2**/$PC_{61}BM$ devices, partly due to the decreased R_s (from 43 to 20 Ω/cm^2) while hole mobilities of **1** and **2** was ten times higher than those of **3**. There are several reports that the FF is also affected by geminate and non-geminate recombination.[44-47] Further investigation of recombination is required for discuss the relationship between molecular structure and FF.

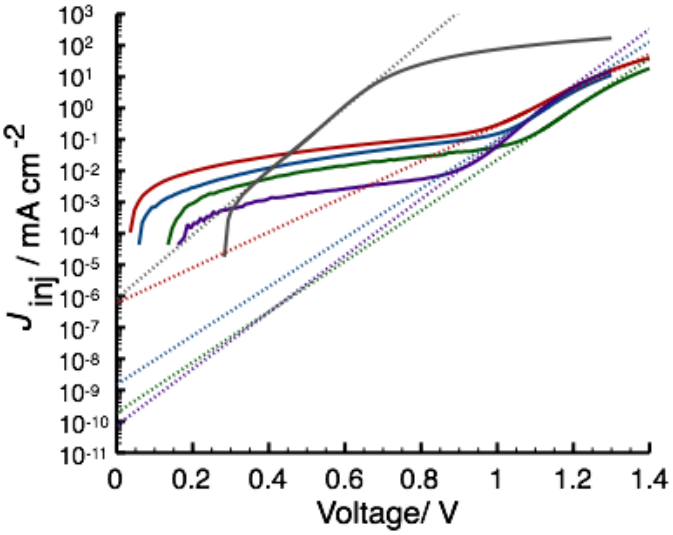

Figure 11. Dark injected current J_{inj} versus voltage V for **1** (red), **2** (green), **3** (blue) and **4**(purple) and P3HT (black)/$PC_{61}BM$ blended active layers. The dotted lines represent exponential fits, allowing determination of $J_{0,n}$.

The BHJ solar cells based on **1-4** exhibited high V_{oc} values of > 1.0 V. The rhodanine-terminated donors based on benzo[1,2-*b*:4,5-*b'*]dithiophene unit also exhibited high V_{oc} values above 0.9V in the solution processes BHJ solar cells as reported by Zhou et el.[20, 21] The origin of high V_{oc} values was analyzed by fitting the dark current density-voltage curve using the Shockley diode model modified for organic solar cells (Figure 11, Table 3).[48-50] The J_{so} values obtained from the Shockley equation have been used as an index for the strength difference of intermolecular interactions of donors with $PC_{61}BM$ in the active layer. The J_{so} value for the **4**/$PC_{61}BM$ cell (4.80×10^{-3} mA/cm^2) was much smaller than that for the P3HT/$PC_{61}BM$ cell (3.79 mA/cm^2), revealing that **4** showed weaker interaction with $PC_{61}BM$ than P3HT.[50] Pyrene-cored donor **4** showed the weaker interaction with $PC_{61}BM$. The high V_{oc} values above 1.0 V might be cased by a small recombination loss of carriers in active layer due to the weak intermolecular interactions between the disk-shaped donor and the fullerene acceptor.

Table 3. Summary of measured and simulated device parameters of BHJ solar cells based on mixed active layers composed of **1-4** and P3HT/ $PC_{61}BM$.

active layer (weight ratio)	$J_{0,n}$ /mA cm^{-2}	ΔE_{DA} [a]	J_{so} /mA cm^{-2}	$V_{oc,\,cal}$/ V	$V_{oc,\,exp}$/ V
1/ $PC_{61}BM$ (1:3)	5.91×10^{-7}	1.43	6.70×10^{-3}	1.19	1.04
2/ $PC_{61}BM$ (1:4)	1.85×10^{-10}	1.53	2.81×10^{-4}	1.26	1.15
3/ $PC_{61}BM$ (1:4)	1.94×10^{-9}	1.36	3.06×10^{-4}	1.23	1.11
4/ $PC_{61}BM$ (1:3)	7.40×10^{-11}	1.33	7.52×10^{-5}	1.21	1.13
P3HT/ $PC_{61}BM$ (2:1)	8.28×10^{-7}	1.09	2.93×10^{-1}	0.69	0.65

[a] the energy difference between the HOMO of donor and the LUMO of acceptor materials.

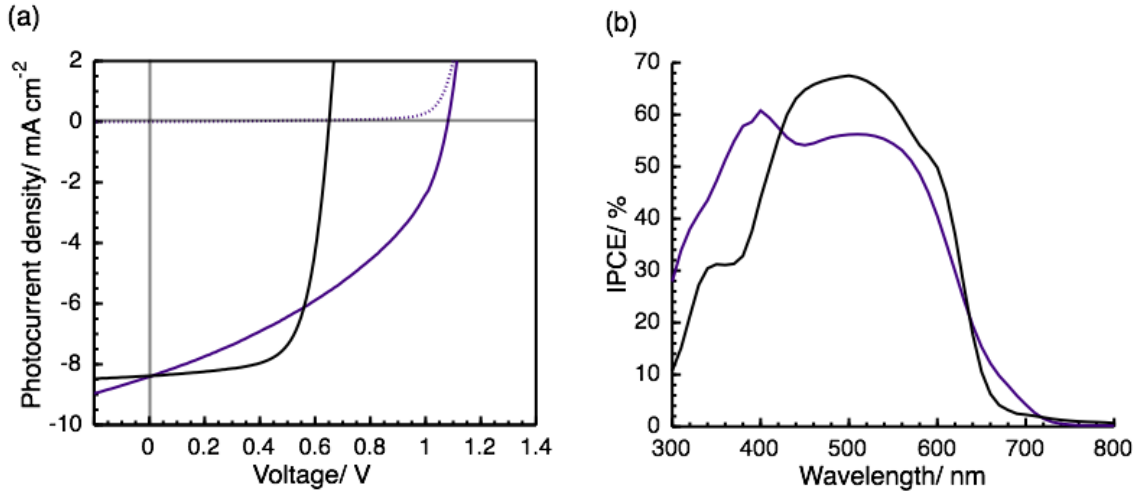

Figure 12. (a) Photocurrent voltage curve obtained with BHJ solar cells based on **4**/ $PC_{71}BM$ (purple) and P3HT/ $PC_{61}BM$ (black) blended active layers under a standard global AM 1.5 solar condition (solid line) and dark current (dotted line). b) Incident photon-to-current conversion efficiency spectrum based on **4**/$PC_{71}BM$ (purple) and P3HT/$PC_{61}BM$ (black) blended active layers.

Figure 12 shows the *J-V* and IPCE characteristics of a **4**/$PC_{71}BM$ device (**4**:$PC_{71}BM$ composition ratio = 1:3 w/w). Since $PC_{71}BM$ has a higher absorption coefficient in the visible range, the J_{sc} value was improved significantly by changing from $PC_{61}BM$ to $PC_{71}BM$. The **4**/$PC_{71}BM$ cell showed a PCE of 3.7 % with a J_{sc} of 8.4 mA/cm^2, V_{oc} of 1.09 V, and *FF* of 41% under one sun condition and exhibited a broad IPCE between 300 and 700nm with a maximum of 57 % at 530 nm (Figure 12b). The IPCE spectra followed the absorption feature of rhodanine-terminated

pyrene-cored donor **4** and $PC_{71}BM$. The low *FF* value of the **4**/$PC_{71}BM$ cell suggests a poor balance of charge carrier mobilities in the active layer. Further enhancement of solar cell performance requires the improvement of hole mobility and investigation of carrier recombination in active layer. Investigations are underway to optimize the structure of pyrene-cored donors to improve the PCEs in BHJ solar cells.

3-3 Conclusions

Four disk-shaped donors **1-4** comprised of a pyrene core and dithiophene linkers, and rhodanine terminal units were synthesized as the donor components of solution-processed BHJ solar cells. The introduction of rhodanine terminal units resulted in expansion of light-harvesting area in the visible light region as well as enhancement of molar absorption coefficients compared to the pyrene-cored donors lacking rhodanine terminal units. The length of peripheral alkyl chains changed molecular ordering and carrier transport properties in solid state. The HOMO and LUMO energy levels of these materials were suitable for the donor component in BHJ solar cells with fullerene acceptor. The BHJ solar cells were fabricated by the solution process using mixed solutions of pyrene-cored donors with fullerene acceptors. The PCE values strongly depended on the structure of the donor. The J_{sc} is strongly affected by the number of the functional side chains. In addition, the shortening of the peripheral alkyl chain length in the dithiophene linkers improved the J_{sc} due to its better hole-mobility in the film. There is no clear relationship between hole mobilities and FF in this study. The highest PCE of BHJ solar cells achieved a **4**/ $PC_{71}BM$ device with a PCE of 3.7%, J_{sc} of 8.4 mA/cm^2, V_{oc} of 1.09 V, and *FF* of 41% under one sun condition.

3-4 Experimental Section

3-4-1 General

NMR spectra were recorded on a Bruker AVANCE 400 FT NMR spectrometer at 400.13 MHz and 100.61MHz for ^1H and ^{13}C in $CDCl_3$ solution. Chemical shifts are reported relative to internal TMS. UV-Vis spectra were measured

on a JASCO V-650. MALDI-TOF mass spectra were obtained on a Bruker autoflex with dithranol as matrix. The transition temperatures were measured by differential scanning calorimetry with a SII DSC 6200 operated at a scanning rate of $10^{o}C\ min^{-1}$ on heating and cooling. The apparatus was calibrated with indium as standard. The XRD patterns were obtained with a Rigaku XRD-DSC with Cu Ka radiation. Atomic force microscopy images were acquired in tapping mode by a JEOL JSPM-5400 system. The samples for AFM were prepared by the spin-coating of $CHCl_3$ solutions on quartz substrate. Cyclic voltammetric measurements were recorded on an ALS 700 potentiostat using a three cell electrode system with a Pt working electrode, a Pt counter electrode and an Ag/AgCl reference electrode. $TBAPF_6$ was used as the electrolyte.

3-4-2 Materials

All chemicals were purchased from commercial suppliers and used without purification. P3HT was purchase from Rieke Metals Inc. (electronic grade) and used without any purification. 1,3,6,8-Tetrabromopyrene and 5-bromo-3-hexylthiophene-2-carbaldehyde were synthesized according to the literature methods.[24,51,52] Column chromatography was performed with silica gel (Wakogel C-200). Recycling preparative gel permeation chromatography was carried out by a JAI recycling preparative HPLC using $CHCl_3$ as an eluent. Analytical thin layer chromatography was performed with commercial Merck plates coated with silica gel 60 F_{254}. The purities of target compounds were confirmed by NMR, MALDI-TOF-Ms and analytical HPLC.

Four pyrene-cored donors **1-4** were prepared according to the synthetic route as shown in Scheme 1.

1: **8** (48mg, 0.05mmol) was dissolved in solution of dry $CHCl_3$ (15ml), then a few drops of dry piperidine and 3-ethylrhodanine (0.1g, 0.62mmol) was added. The mixture was stirred at 65˚C for 24h. After cooling to room temperature, the reaction mixture was poured into water, extracted with $CHCl_3$. The organic layer was dried

over magnesium sulfate and the solvent was evaporated. The residue was purified by column chromatography on silica gel by eluting with $CHCl_3$ and recycling preparative HPLC to give **1** as dark purple solid (37mg, yield 59 %). ^{1}H-NMR (400.13 MHz, $CDCl_3$): δ (ppm) = 8.37 (s, 4H, Ar*H*), 8.09 (s, 4H, Ar*H*), 7.97 (s, 2H, Ar*H*), 7.50 (s, 2H, Ar*H*), 7.18 (s, 2H, Ar*H*), 4.22 (q, *J* = 6.7 Hz, 4H, -CH_2-), 2.93 (t, *J* = 7.9 Hz, 4H, -CH_2-), 2.84 (t, *J* = 7.9 Hz, 4H, -CH_2-), 1.85-1.71 (m, 4H, -CH_2-), 1.79-1.72 (m, 4H, -CH_2-), 1.41-1.34 (m, 24H, -CH_2-), 1.32 (t, *J* = 6.8 Hz, 6H, -CH_3), 0.96-0.90 (m, 12H, -CH_3). MALDI-TOF-Ms: *m/z* = 1207.97 (M+H); Calcd for $C_{68}H_{76}N_2O_2S_8$: *m/z* = 1208.37. UV-Vis ($CHCl_3$): λ_{max} (log ε) = 510 (4.82), 345 (4.75), 327 (4.64).

2: Yield 66%. ^{1}H-NMR (400.13 MHz, $CDCl_3$): δ (ppm) = 8.52 (d, *J* = 9.2 Hz, 2H, Ar*H*), 8.24 (s, 2H, Ar*H*), 8.17 (s, 1H, Ar*H*), 8.09 (d, *J* = 9.2 Hz, 2H, Ar*H*), 7.90 (s, 1H, Ar*H*), 7.27 (s, 2H, Ar*H*), 7.14 (s, 2H, Ar*H*), 4.18 (q, *J* = 6.7 Hz, 4H, -CH_2-), 2.92 (t, *J* = 7.6 Hz, 4H, -CH_2-), 2.76 (t, *J* = 7.6 Hz, 4H, -CH_2-), 1.83-1.75 (m, 4H, -CH_2-), 1.70-1.62 (m, 4H, -CH_2-), 1.60 (s, 9H, -CH_3), 1.51-1.48 (m, 4H, -CH_2-), 1.41-1.32 (m, 20H, -CH_3), 1.30 (t, *J* = 6.8 Hz, 6H, -CH_2-), 0.95-0.88 (m, 12H, -CH_2-). ^{13}C-NMR ($CDCl_3$, 100.61 MHz): δ (ppm) = 192.6, 167.9, 151.1, 150.2, 156.0, 143.6, 142.5, 142.1, 132.3, 131.5, 130.0, 129.3, 128.8, 128.7, 126.1, 124.9, 123.9, 123.5, 119.5, 40.3, 35.7, 32.3, 32.3, 32.0, 31.5, 31.0, 30.5, 29.8, 29.5, 29.4, 23.2, 23.0, 21.7, 14.6, 14.5. MALDI-TOF-Ms: *m/z* = 1264.06 (M+H); Calcd for $C_{72}H_{84}N_2O_2S_8$: *m/z* = 1264.43. UV-Vis ($CHCl_3$): λ_{max} (log ε) = 494 (4.95), 395 (4.55), 314 (4.67).

3: Yield 65 %. ^{1}H-NMR (400.13 MHz, $CDCl_3$): δ (ppm) = 8.37 (s, 4H, Ar*H*), 8.10 (s, 2H, Ar*H*), 7.88 (s, 4H, Ar*H*), 7.20 (s, 4H, Ar*H*), 7.16 (s, 4H, Ar*H*), 4.22 (q, *J* = 6.7 Hz, 8H, -CH_2-), 2.93 (t, *J* = 7.6 Hz, 8H, -CH_2-), 2.82 (t, *J* = 7.6 Hz, 8H, -CH_2-), 1.82-1.74 (m, 8H, -CH_2-), 1.73-1.68 (m, 8H, -CH_2-), 1.54-1.37 (m, 48H, -CH_2-), 1.33 (t, *J* = 7.2 Hz, 12H, -CH_3), 0.97-0.91 (m, 24H, -CH_3). ^{13}C-NMR ($CDCl_3$, 100.61 MHz): δ (ppm) = 192.0, 167.4, 150.6, 142.0, 141.2, 132.2, 131.9, 131.7, 129.2, 123.2, 119.1, 40.0, 31.8, 31.7, 31.2, 30.4, 29.5, 29.2, 29.1, 22.8, 14.2. MALDI-TOF-Ms: *m/z* = 2214.38 (M+H); Calcd for $C_{120}H_{142}N_4O_4S_{16}$: *m/z* = 2214.67. UV-Vis ($CHCl_3$): λ_{max} (log ε) = 501 (5.18), 320 (4.84).

4: Yield 79%. ^{1}H-NMR (400.13 MHz, $CDCl_3$): δ (ppm) = 8.18 (s, 4H, Ar*H*), 7.97 (s, 2H, Ar*H*), 7.81 (s, 4H, Ar*H*), 7.12 (s, 4H, Ar*H*), 7.10 (s, 4H, Ar*H*), 4.22 (q, *J* = 6.7Hz, 8H, -C*H*$_2$-), 2.90 (t, *J* = 7.6 Hz, 8H, -C*H*$_2$-), 2.47 (s, 12H, -C*H*$_2$-), 1.81-1.73 (m, 8H, -C*H*$_2$-), 1.55-1.51 (m, 8H, -C*H*$_2$-), 1.44-1.41 (m, 16H, -C*H*$_2$-), 1.33 (t, *J* = 7.2 Hz, 12H, -C*H*$_3$), 0.97 (t, *J* = 7.2 Hz, 12H, -C*H*$_3$). ^{13}C-NMR ($CDCl_3$, 100.61 MHz): δ (ppm) = 191.8, 167.3, 145.0, 143.3, 141.9, 141.2, 132.1, 131.7, 130.7, 128.9, 128.2 127.8, 125.0, 124.9, 124.5, 123.0, 118.8, 45.6, 45.2, 40.1, 37.5, 37.1, 34.5, 33.4, 32.8, 31.8, 32.5, 30.5, 30.2, 30.1, 29.7, 29.6, 27.5, 27.1, 22.9, 20.4, 19.8, 14.8, 14.3. MALDI-TOF-Ms: *m/z* = 1934.07 (M+H); Calcd for $C_{100}H_{102}N_4O_4S_{16}$ *m/z* = 1934.34. UV-Vis ($CHCl_3$): λ_{max} (log ε) = 502 (5.16), 321 (4.78).

Synthetic Procedures of 6-18.

6: A solution of 5-bromo-3-hexylthiophene-2-carbaldehyde (0.18g, 0.66mmol), 3-hexyl-2-thiopheneboronic acid pinacol ester (0.29g, 0.99mmol) and $Pd(PPh_3)_4$ (15mg, 0.02mmol) in toluene (8ml), THF (9.6ml) and 2.0 M K_2CO_3 aqueous solution (5ml) was refluxed for 48 h under nitrogen. After cooling to room temperature, the reaction mixture was poured into water, extracted with CH_2Cl_2. The organic layer was dried over magnesium sulfate and the solvent was evaporated. The residue was purified by column chromatography on silica gel by eluting with CH_2Cl_2 and recycling preparative HPLC to give **6** as yellow oil (0.13g, yield 54 %). ^{1}H-NMR (400.13 MHz, $CDCl_3$): δ (ppm) = 10.00 (s, 1H, Ar*H*), 7.24 (d, *J* = 5.2 Hz, 1H, Ar*H*), 7.02 (s, 1H, Ar*H*), 6.94 (d, *J* = 5.2 Hz, 1H, Ar*H*), 2.93 (t, *J* = 7.6 Hz, 2H, -C*H*$_2$-), 2.80 (t, *J* = 7.6 Hz, 2H, -C*H*$_2$-), 1.75-1.62 (m, 4H, -C*H*$_2$-), 1.43-1.27 (m, 12H, -C*H*$_2$-), 0.93-0.88 (m, 6H, -C*H*$_3$). ^{13}C-NMR ($CDCl_3$, 100.61 MHz): δ (ppm) = 182.1, 153.7, 145.9, 142.4, 136.8, 131.1, 130.3, 128.9, 125.9, 32.1, 32.0, 31.8, 30.8, 30.0, 29.6, 29.4, 28.9, 23.0, 21.7, 14.5.

7: N-Bromosuccinimide (NBS) (67mg, 0.37mmol) was slowly added to the solution of **6** (0.11g, 0.31mmol) in chloroform (10ml) and acetic acid (10ml). The reaction mixture was refluxed for 24h and poured into water. After extraction with CH_2Cl_2, the organic layer was dried over magnesium sulfate and the solvent was evaporated. The

residue was purified by column chromatography on silica gel by eluting with CH_2Cl_2 and recycling preparative HPLC to give **7** as yellow solid (94mg, yield 68%). ^{1}H-NMR (400.13 MHz, $CDCl_3$): δ (ppm) = 10.00 (s, 1H, -C*H*O), 7.17 (s, 1H, Ar*H*), 7.09 (s, 1H, Ar*H*), 3.12-3.05 (m, 2H, -CH_2-), 2.99-2.90 (m, 2H, -CH_2-), 1.84-1.78 (m, 4H, -CH_2-), 1.51-1.40 (m, 12H, -CH_2-), 1.06-1.01 (m, 6H, -CH_3). ^{13}C-NMR ($CDCl_3$, 100.61 MHz): δ (ppm) = 182.4, 154.0, 146.2, 142.7, 137.1, 131.4, 130.6, 129.4, 129.2, 126.2, 32.4, 32.3, 32.1, 31.1, 31.0, 29.9, 29.8, 29.2, 23.3, 21.7, 14.7.

Suzuki-Miyaura coupling reaction with pyrene-cores.

8: A solution of 2,7-Bis(4,4,5,5-tetramethyl-1,3,2-dioxaborolan-2-yl)pyrene (32mg, 0.07 mmol), **7** (94mg, 0.21mmol) and $Pd(PPh_3)_4$ (21mg, 0.02mmol) in toluene (25ml), ethanol (8ml) and 2.0 M K_2CO_3 aqueous solution (5ml) was stirred at 120 °C for 48 h under nitrogen. After cooling to room temperature, the reaction mixture was poured into water, extracted with $CHCl_3$. The organic layer was dried over magnesium sulfate and the solvent was evaporated. The residue was purified by column chromatography on silica gel by eluting with $CHCl_3$ and recycling preparative HPLC to give **8** as yellow solid (48mg, yield 74 %). ^{1}H-NMR (400.13 MHz, $CDCl_3$): δ (ppm) = 10.00 (s, 2H, -C*H*O), 8.09 (s, 4H, Ar*H*), 7.88 (s, 4H, Ar*H*), 7.29 (s, 2H, Ar*H*), 7.02 (s, 2H, Ar*H*), 2.91 (t, *J* = 7.9 Hz, 4H, -CH_2-), 2.78 (t, *J* = 7.9Hz, 4H, -CH_2-), 1.76-1.67 (m, 8H, -CH_2-), 1.48-1.34 (m, 24H, -CH_2-), 0.98-0.93 (m, 12H, -CH_3). ^{13}C-NMR ($CDCl_3$, 100.61 MHz): δ (ppm) = 181.9, 153.7, 145.7, 144.1, 143.6, 136.5, 131.6, 131.3, 130.3, 128.3, 128.2, 127.4, 124.2, 122.2, 32.2, 32.0, 31.8, 30.8, 30.6, 30.5, 29.8, 29.5, 28.9, 23.1, 14.5. MALDI-TOF-Ms: *m/z* = 923.44 (M+H); Calcd for $C_{58}H_{60}O_2S_4$: *m/z* = 922.39.

9: Yield 81%. ^{1}H-NMR (400.13 MHz, $CDCl_3$): δ (ppm) = 8.49 (d, *J* = 9.2 Hz, 2H, Ar*H*), 8.19 (s, 2H, Ar*H*), 8.16 (s, 1H, Ar*H*), 8.03 (d, *J* = 9.2 Hz, 2H, Ar*H*), 7.20 (s, 2H, Ar*H*), 7.03 (s, 2H, Ar*H*), 2.68 (t, *J* = 7.9Hz, 4H, -CH_2-), 1.85-1.78 (m, 4H, -CH_2-), 1.56 (s, 9H, -CH_3), 1.54-1.42 (m, 12H, -CH_2-), 0.90 (t, *J* = 6.9 Hz, 6H, -CH_3). ^{13}C-NMR ($CDCl_3$, 100.61 MHz): δ (ppm) =149.9, 144.2, 142.3, 131.7, 130.7, 130.2, 130.0, 129.0, 128.7, 126.0, 125.4, 123.7, 123.0, 121.4, 35.7, 32.4, 32.2, 31.2, 31.0,

29.6, 25.1, 23.2, 14.7. MALDI-TOF-Ms: *m/z* = 590.37 (M+H); Calcd for $C_{40}H_{46}S_2$: *m/z* = 590.30.

11: Yield 66%. ^{1}H-NMR (400.13 MHz, $CDCl_3$): δ (ppm) = 8.58 (d, *J* = 9.2 Hz, 2H, Ar*H*), 8.21 (s, 2H, Ar*H*), 8.09 (d, *J* = 9.2Hz, 2H, Ar*H*), 7.22 (s, 1H, Ar*H*), 7.05 (s, 2H, Ar*H*), 6.89 (s, 2H, Ar*H*), 2.86 (t, *J* = 8.0Hz, 4H, Ar*H*), 2.61 (t, *J* = 7.2 Hz, 4H, -CH_2-), 1.89-1.81 (m, 4H, -CH_2-), 1.79-1.73 (m, 4H, -CH_2-), 1.68 (s, 12H, -CH_3), 1.51-1.45 (m, 4H, -CH_2-), 1.38-1.33 (m, 24H, -CH_2-), 0.90 (m, 12H, -CH_3). ^{13}C-NMR ($CDCl_3$, 100.61 MHz): δ (ppm) = 150.0, 149.3, 144.1, 140.3, 136.2, 132.7, 131.7, 130.3, 129.6, 128.9, 127.7, 126.2, 125.3, 123.7, 120.5, 35.7, 32.4, 32.2, 31.2, 31.0, 30.9, 30.0, 29.8, 29.5, 23.2, 23.1,14.6. MALDI-TOF-Ms: *m/z* = 922.32 (M+H); Calcd for $C_{60}H_{74}S_4$: *m/z* = 922.47.

13: Yield 76%. ^{1}H-NMR (400.13 MHz, $CDCl_3$): δ (ppm) = 8.54 (s, 4H, Ar*H*), 8.21 (s, 2H, Ar*H*), 7.23 (s, 4H, Ar*H*), 7.09 (s, 4H, Ar*H*), 2.72 (t, *J* = 7.6 Hz, 8H, -CH_2-), 1.76-1.69 (m, 8H, -CH_2-), 1.45-1.32 (m, 24H, -CH_2-), 0.91 (t, *J* = 7.2 Hz, 12H, -CH_3). ^{13}C-NMR ($CDCl_3$, 100.61 MHz): δ (ppm) =144.0, 142.0, 131.3, 130.5, 130.2, 129.2, 126.4, 126.1, 121.5, 32.1, 31.1, 31.0, 29.5, 23.1, 14.5. MALDI-TOF-Ms: *m/z* = 866.51 (M+H); Calcd for $C_{56}H_{66}S_4$: *m/z* = 866.40.

15: Yield 80%. ^{1}H-NMR (400.13 MHz, $CDCl_3$): δ (ppm) = 8.64 (s, 4H, Ar*H*), 8.26 (s, 2H, Ar*H*), 7.25 (s, 4H, Ar*H*), 7.06 (s, 4H, Ar*H*), 6.93 (s, 4H, Ar*H*), 2.87 (t, *J* = 7.6 Hz, 8H, -CH_2-), 2.64 (t, *J* = 7.6 Hz, 8H, -CH_2-), 1.79-1.72 (m, 8H, -CH_2-), 1.71-1.63 (m, 8H, -CH_2-), 1.47-1.31 (m, 48H, -CH_2-), 0.92-0.88 (m, 24H, -CH_3). ^{13}C-NMR ($CDCl_3$, 100.61 MHz): δ (ppm) = 144.1, 140.3, 139.9, 136.1, 132.9, 131.7, 131.0, 130.0, 129.1, 127.8, 126.5, 126.1, 120.5, 32.1, 31.2, 30.9, 30.8, 29.9, 29.8, 29.5, 23.1, 23.0, 14.5. MALDI-TOF-Ms: *m/z* = 1530.82 (M+H); Calcd for $C_{96}H_{122}S_8$: *m/z* = 1531.74.

17: Yield 64%. ^{1}H-NMR (400.13 MHz, $CDCl_3$): δ (ppm) = 8.63 (s, 4H, Ar*H*), 8.25 (s, 2H, Ar*H*), 7.25 (s, 4H, Ar*H*), 7.04 (s, 4H, Ar*H*), 6.93 (s, 4H, Ar*H*), 2.87 (t, *J* = 7.6 Hz, 8H), 2.31 (s, 12H, -CH_3), 1.82-1.75 (m, 8H, -CH_2-), 1.79-1.72 (m, 8H, -CH_2-), 1.40-1.34 (m, 16H, -CH_2-), 0.90 (t, *J* = 7.2 Hz, 24H, -CH_3). ^{13}C-NMR ($CDCl_3$, 100.61

MHz): δ (ppm) = 140.4, 140.0, 138.5, 136.2, 132.7, 131.7, 131.0, 130.0, 129.1, 128.7, 126.1, 121.2, 32.1, 31.2, 29.9, 29.7, 23.1, 16.2, 14.5. MALDI-TOF-Ms: *m/z* = 1250.08 (M+H); Calcd for $C_{76}H_{82}S_8$: *m/z* = 1249.98.

Bromination of thiophene terminates.

10: NBS (0.12g, 0.65mmol) was slowly added to the solution of **9** (0.15g, 0.32mmol) in dry THF (20ml) at 0°C. The reaction mixture was stirred for 12h at RT and poured into water. After extraction with CH_2Cl_2, the organic layer was dried over magnesium sulfate and the solvent was evaporated. The residue was purified by column chromatography on silica gel by eluting with CH_2Cl_2 and recycling preparative HPLC to give **10** as yellow solid (0.19g, yield 95%). ^{1}H-NMR (400.13 MHz, $CDCl_3$): δ (ppm) = 8.32 (d, *J* = 9.2 Hz, 2H, Ar*H*), 8.11 (s, 2H, Ar*H*), 7.95 (d, *J* = 9.2 Hz, 2H, Ar*H*), 7.92 (s, 1H, Ar*H*), 6.95 (s, 2H, -C*H*$_2$-), 2.56 (t, *J* = 7.9 Hz, 4H, -C*H*$_2$-), 1.80-1.78 (m, 4H, -C*H*$_2$-), 1.64 (s, 9H, -C*H*$_3$), 1.52-1.38 (m, 4H, -C*H*$_2$-), 0.81 (t, *J* = 7.2 Hz, 6H, -C*H*$_3$). ^{13}C-NMR ($CDCl_3$, 100.61 MHz): δ (ppm) =150.1, 143.1, 142.0, 131.5, 130.2, 129.6, 129.2, 129.1, 126.0, 125.6, 124.9, 123.5, 110.1, 35.7, 32.4, 32.3, 30.4, 30.3, 29.6, 23.2, 14.6. MALDI-TOF-Ms: *m/z* = 747.95 (M+H); Calcd for $C_{40}H_{44}Br_2S_2$: *m/z* = 746.12.

14: Yield 94%. ^{1}H-NMR (400.13 MHz, $CDCl_3$): δ (ppm) = 8.49 (s, 4H, Ar*H*), 8.09 (s, 2H, Ar*H*), 7.07 (s, 4H, Ar*H*), 2.68 (t, *J* = 7.2 Hz, 8H, -C*H*$_2$-), 1.73-1.65 (m, 8H, -C*H*$_2$-), 1.45-1.33 (m, 24H, -C*H*$_2$-), 0.91 (t, *J* = 7.2 Hz, 12H, -C*H*$_3$). ^{13}C-NMR ($CDCl_3$, 100.61 MHz): δ (ppm) = 143.2, 141.5, 129.8, 129.4, 126.2, 126.1, 110.3, 32.0, 30.2, 30.1, 29.4, 23.0, 14.5. MALDI-TOF-Ms: *m/z* = 1182.36 (M+H); Calcd for $C_{56}H_{62}Br_4S_4$: *m/z* = 1182.04.

Formylation of thiophene terminates.

12: A solution of **11** (0.19g, 0.21mmol) in dry 1,2-dichloroethane (15ml) was stirred at 0˚C. Vilsmeir-reagent, which was prepared with 1 ml of $POCl_3$ in dry DMF 5 ml, was added. The mixture was refluxed for overnight and quenched 10% aqueous solution of NaOAc after cooling. After extraction with CH_2Cl_2, the organic layer was

dried over magnesium sulfate and the solvent was evaporated. The residue was purified by column chromatography on silica gel by eluting with CH_2Cl_2 and recycling preparative HPLC to give **12** as yellow solid (0.15g, Yield 74%). ^{1}H-NMR (400.13 MHz, $CDCl_3$): δ (ppm) = 10.05 (s, 2H, Ar*H*), 8.56 (d, *J* = 9.2 Hz, 2H, Ar*H*), 8.29 (s, 2H, Ar*H*), 8.22 (s, 1H, Ar*H*), 8.14 (d, *J* = 9.3Hz, 2H, Ar*H*), 7.30 (s, 2H, Ar*H*), 7.15 (s, 2H, Ar*H*), 2.96 (t, *J* = 7.6 Hz, 8H, -C*H*$_2$-), 1.85-1.78 (m, 4H, -C*H*$_2$-), 1.77-1.70 (m, 4H, -C*H*$_2$-), 1.64 (s, 9H, -C*H*$_3$), 1.55-1.48 (m, 4H, -C*H*$_2$-), 1.45-1.34 (m, 20H, -C*H*$_2$-), 0.98-0.93 (m, 12H, -C*H*$_3$). ^{13}C-NMR ($CDCl_3$, 100.61 MHz): δ (ppm) = 182.0, 153.7, 145.6, 143.0, 142.3, 136.9, 132.2, 131.5, 130.0, 129.4, 129.1, 128.8, 126.0, 124.8, 123.5, 35.7, 32.3, 32.0, 31.8, 30.9, 30.4, 29.8, 29.4, 28.9, 25.1, 23.1, 23.0, 21.8, 14.5. MALDI-TOF-Ms: *m/z* = 978.42 (M+H); Calcd for $C_{62}H_{74}O_2S_4$: *m/z* = 978.46.

16: Yield 76%. ^{1}H-NMR (400.13 MHz, $CDCl_3$): δ (ppm) =10.05 (s, 4H, -C*H*O), 8.63 (s, 4H, Ar*H*), 8.27 (s, 2H, Ar*H*), 7.30 (s, 4H, Ar*H*), 7.14 (s, 4H, Ar*H*), 3.00-2.91 (m, 16H, -C*H*$_2$-), 1.82-1.70 (m, 16H, -C*H*$_2$-), 1.50-1.31 (m, 48H, -C*H*$_2$-), 0.90 (m, 24H, -C*H*$_3$). ^{13}C-NMR ($CDCl_3$, 100.61 MHz): δ (ppm) = 182.1, 153.8, 145.3, 143.0, 141.8, 137.0, 132.5, 131.8, 129.8, 129.4, 129.0, 126.3, 32.1, 32.0, 31.8, 20.9, 30.3, 29.7, 29.4, 29.9, 23.1, 23.0, 14.5. MALDI-TOF-Ms: *m/z* = 1642.37 (M+H); Calcd for $C_{160}H_{122}O_4S_8$: *m/z* = 1642.71.

18: Yield 49%. ^{1}H-NMR (400.13 MHz, $CDCl_3$): δ (ppm) = 10.03 (s, 4H, -C*H*O), 8.40 (s, 4H, Ar*H*), 8.14 (s, 2H, Ar*H*), 7.21 (s, 4H, Ar*H*), 7.06 (s, 4H, Ar*H*), 2.90 (t, *J* = 7.6 Hz, 8H, -C*H*$_2$-), 2.58 (s, 12H, -C*H*$_3$), 1.81-1.72 (m, 8H, -C*H*$_2$-), 1.52-1.44 (m, 8H, -C*H*$_2$-), 1.39-1.33 (m, 16H, -C*H*$_2$-), 0.90 (t, *J* = 7.2 Hz, 12H, -C*H*$_3$). ^{13}C-NMR ($CDCl_3$, 100.61 MHz): δ (ppm) = 182.1, 148.2, 145.2, 143.0, 141.9, 136.9, 132.4, 131.7, 131.0, 129.7, 129.3, 128.7, 125.9, 32.1, 30.9, 30.4, 29.8, 23.1, 14.6. MALDI-TOF-Ms: *m/z* = 1362.25 (M+H); Calcd for $C_{80}H_{82}O_4S_8$: *m/z* = 1362.40.

3-4-3 Device Fabrications

Indium tin oxide (ITO) patterned glass substrates were cleaning with sonication in neutral detergent, distilled water, acetone and 2-propanol. The substrates were dried and apply UV-O_3 treatment for 30min. Electron blocking layer were prepared by spin-coated the PEDOT:PSS (H. C. Starck) with a thickness of 40 nm. The substrates were baked at 200˚C for 30 min. A solution containing a mixture of pyrene-cored donors and fullerene derivatives in chloroform were spin-coated onto the PEDOT: PSS layer, and apply thermal annealing treatment at 150˚C for 10min in the argon filled globe box. Titanium oxide solution was spin-coated onto the active layer then place in air for 30min. The counter electrode of aluminum was prepared by thermal deposition with a thickness of 100nm. Current density-voltage (*J-V*) characteristics were measured using a Keithley 2400 Source Measure Unit. Performance of BHJ solar cells devices was measured under one-sun conditions (AM 1.5, 100mW/cm^2) by a solar simulator (XES-151S, Sanei electric Inc.).

3-4-4 Hole-mobility Measurement

Hole-mobility of donor materials were carried out with the device structure of ITO/ PEDOT:PSS/ donor material/ Au by taking current-voltage curves in the range of 0-7V. The hole-mobility was calculated using the space charge current limited (SCLC) method using the Mott-Gurney square law[53-56] (Eq. 1),

$$J = \frac{9}{8}\,\varepsilon_0 \varepsilon_r \mu_h \frac{V^2}{L^3} \quad (1)$$

where J is the current density, ε_0 is the permittivity of free space (8.85×10^{-12} F m^{-1}), ε_r is the relative dielectric constant of the transport of medium (assumed to be 3), μ_h is the hole mobility, V is the internal voltage in the device ($V = V_{appl} - V_r - V_{bi}$, where V_{appl} is the applied voltage in the device, V_r is voltage drop due to the contact resistance and V_{bi} is the built-in voltage due to relative work function difference between the two electrodes. The V_{bi} can be determined from the transition between the Ohmic region and SCLC region and L is the thickness of film.

3-4-5 Discussion about Open Circuit Voltage

The dark injected current J_{inj} versus applied voltage for **1-4** and P3HT /$PC_{61}BM$ devices was exponentially fitted according to Eq. 2, therefore to determine reverse saturation current density $J_{0,n}$ (Figure 8).

$$J_{inj} = J_{0,n}\exp\left(\frac{qV}{nkT}\right) \quad (2)^{57}$$

J_{so} is calculated according to Eq. 3.

$$J_{0,n} = J_{so}\exp\left(\frac{-\Delta E_{DA}}{2nkT}\right) \quad (3)^{58}$$

For comparison, the V_{oc} of **1-4** and P3HT/ $PC_{61}BM$ were calculated from Eq. 4 and resulted V_{oc} was consistent with the trend of the experimental V_{oc} (Table 3).

$$V_{oc} = \frac{nkT}{q}\ln\left(\frac{J_{sc}}{J_{0,n}} + 1\right) \approx \frac{nkT}{q}\ln\left(\frac{J_{SC}}{J_{SO}}\right) + \frac{\Delta E_{DA}}{2q} \quad (4)^{58}$$

3-5 References

1. S. Günes, H. Neugebauer, N. S. Sariciftci, *Chem. Rev.*, **2007**, 107, 1324.
2. A. J. Heeger, *Adv. Mater.*, **2014**, 26, 10.
3. M. T. Dang, L. Hirsch, G. Wantz, J. D. Wuest, *Chem. Rev.*, **2013**, 113, 3734.
4. Y. Huang, E. J. Kramer, A. J. Heeger, G. C. Bazan, *Chem. Rev.*, **2014**, 114, 7006.
5. T. M. Clarke, J. R. Durrant, *Chem. Rev.*, **2010**, 110, 6736.
6. Y. –J. Cheng, S. –H. Yang, C. –S. Hsu, *Chem. Rev.*, **2009**, 109, 5868.
7. M. Riede, T. Mueller, W. Tress, R. Schueppei, K. Leo, *Nanotechnology*, **2008**, 19, 424001.
8. J. Roncali, *Acc. Chem. Res.*, **2009**, 42, 1719.
9. B. Walker, C. Kim, T. –Q. Nguyen, *Chem. Mater.*, **2011**, 23, 470.
10. A. Mishra, P. Bäuerle, *Angew. Chem. Int. Ed.*, **2012**, 51, 2020.
11. B. Walker, A. B. Tamayo, X. –D. Dang, P. Zalar, J. H. Seo, A. Garcia, M. Tantiwiwat, T. –Q. Nguyen, *Adv. Funct. Mater.*, **2009**, 19, 3063.
12. Y. Matsuo, Y. Sato, T. Niinomi, I. Soga, H. Tanaka, E. Nakamura, *J. Am. Chem. Soc.*, **2009**, 131, 16048.
13. G. Wei, S. Wang, K. Renshaw, M. E. Thompson, S. R. Forrest, *ACS Nano*, **2010**, 4, 1927.

14. G. Wei, S. Wang, K. Sun, M. E. Thompson, S. R. Forrest, *Adv. Energy Mater.*, **2011**, 1, 184.
15. H. Shang, H. Fan, Y. Liu, W. Hu, Y. Li, X. Zhan, *Adv. Mater.*, **2011**, 23, 1554.
16. S. Loser, C. J. Bruns, H. Miyauchi, R. P. Prtiz, A. Facchetti, S. I. Stupp, T. J. Marks, *J. Am. Chem. Soc.*, **2011**, 133, 8142.
17. J. Zhang, D. Deng, C. He, Y. He, M. Zhang, Z. –G. Zhang, Z. Zhang, Y. Li, *Chem. Mater.*, **2011**, 23, 817.
18. Y. Sun, G. C. Welch, W. L. Leong, C. J. Takacs, G. C. Bazan, A. J. Heeger, *Nat. Mater.*, **2012**, 11, 44.
19. T. S. van der Poll, J. A. Love, T. –Q. Nguyen, G. C. Bazan, *Adv. Mater.*, **2012**, 24, 3646.
20. J. Zhou, X. Wan, Y. Liu, Y. Zuo, Z. Li, G. He, G. Ling, W. Ni, C. Li, X. Su, Y. Chen, *J. Am. Chem. Soc.*, **2012**, 134, 16345.
21. J. Zhou, Y. Zuo, X. Wan, G. Long, Q. Zhang, W. Ni, Y. Liu, Z. Li, G. He, C. Li, B. Kan, M. Li, Y. Chen, *J. Am. Chem. Soc.*, **2013**, 135, 8484.
22. K. Takemoto, M. Karasawa, M. Kimura, *ACS Appl. Mater. Interfaces*, **2012**, 4, 6289.
23. T. M. Figueira-Duarte, K. Müllen, *Chem. Rev.*, **2011**, 111, 7260.
24. M. Uchimura, Y. Watanabe, F. Araoka, J. Watanabe, H. Takezoe, G. Konishi, *Adv. Mater.*, **2010**, 22, 4473.
25. Y. Niko, S. Kawauchi, S. Otsu, K. Tokumaru, G. Konishi, *J. Org. Chem.*, **2013**, 78, 3196.
26. Y. Lin, Y. Li, X. Zhan, *Chem. Soc. Rev*. **2012**, 41, 4245.
27. Y. Li, Q. Gao, Z. Li, J. Pei, W. Tian, *Energy Environ. Sci.*, **2010**, 3, 1427.
28. P. –L. T. Boudreault, A. Najari, M. Leclerc, *Chem. Mater.*, **2011**, 23, 456.
29. A. Guerrero, S. Loser, G. Garcia-Belmonte, C. J. Burns, J. Smith, H. Miyauchi, S. I. Stupp, J. Bisquert, T. J. Marks, *Phys. Chem. Chem. Phys*., **2013**, 15, 16456.
30. D. Credgington, F. C. Jamieson, B. Walker, T.-Q. Nguyen, J. R. Durrant, *Adv. Mater.*, **2012**, 24, 2135.
31. C. M. Proctor, C. Kim, D. Neher, T. –Q. Nguyen, *Adv. Funct. Mater*., **2013**, 23, 3584.
32. Z. Li, G. He, X. Wan, Y. Liu, J. Zhou, G. Lomng, Y. Zuo, M. Zhang, Y. Chen, *Adv. Energy Mater.*, **2012**, 2, 74.
33. K. Colladet, S. Fourier, T. J. Cleij, L. Lutsen, J. Gelan, D. Vanderzande, L. H. Nguyen, H. Neugebauer, S. Sariciftci, A. Aguirre, G. Janssen, E. Goovaerts, *Macromolecules*, **2007**, 40, 65.

34. R. Grisorio, G. Allegretta, G. P. Suranna, P. Mastrorilli, A. Loiudice, A. Rizzo, M. Mazzeo, G. Gigli, *J. Mater. Chem.*, **2012**, 22, 19752.
35. A. R. Murphy, P. C. Chang, P. VanDyke, J. Liu, J. M. Fréchet, V. Subramanian, D. M. DeLongchamp, S. Sambasivan, D. A. Fischer, E. K. Lin, *Chem. Mater*., **2005**, 17, 6033.
36. S. Samitsu, T. Shimomura, S. Heike, T. Hashizume, K. Ito, *Macromolecules*, **2008**, 41, 8000.
37. J. D. Dunitz, A. Gavezzotti, *Chem. Soc. Rev.*, **2009**, 38, 2622.
38. G. G. Malliaras, J. R. Salem, P. J. Brock, C. Scott, *Phys. Rev. B*, **1998**, 58, R13411.
39. C. Goh, R. J. Kline, M. D. McGehee, E. N. Kadnikova, J. M. J. Fréchet, *Appl. Phys. Lett.*, **2005**, 86, 12110.
40. Y. Liang, D. Feng, Y. Wu, S. –T. Tsai, G. Li, C. Ray, L. Yu, *J. Am. Chem. Soc.*, **2009**, 131, 7792.
41. Z. B. Wang, M. G. Helander, M. T. Greiner, J. Qiu, Z. H. Lu, *J. Appl. Phys.*, **2010**, 107, 034506.
42. M. D. Perez, C. Borek, S. R. Forrest, M. E. Thompson, *J. Am. Chem. Soc.*, **2009**, 131, 9281.
43. M. –S. Kim, B. –G. Kim, J. Kim, *ACS Appl. Mater. Interfaces*, **2009**, 6, 1264.
44. G. F. A. Dibb, F. C. Jamieson, A. Maurano, J. Nelson, J. R. Durrant, *J. Phys. Chem. Lett*., **2013**, 4, 803.
45. A. K. K. Kyaw, D. H. Wang, V. Gupta, W. L. Leong, L. Ke, G. C. Bazan, A. J. Heeger, ACS Nano, 2013, 7, 4569.
46. Y. Zhang, X. –D. Dang, C. Kim, T. –Q. Nguyen, Adv. Energy. Mater, 2011, 1, 610.
47. J. Min, Y. N. Luponosov, A. Gerl, M. S. Polinskaya, S. M. Peregudova, P. V. Dmitryakov, A. V. Bakirov, M. A. Shcherbina, S. N. Chvalun, S. Grigorian, N. K. –Busies, S. A. Ponomarenko, T. Ameri, C. J. Brabec, Adv. Energy. Mater., 2014, 4, 1301234.
48. K. Vandewal, K. Tvingstedt, A. Gadisa, O. Inganäs, J. Manca, *Nat. Mater.*, **2009**, 8, 904.
49. L. Yang, H. Zhou, W. You, *J. Phys. Chem. C*, **2010**, 114, 16793.
50. G. Long, X. Wan, B. Kan, Y. Liu, G. He, Z. Li, Y. Zhang, Y. Zhang, M. Zhang, Y. Chen, *Adv. Energy Mater.*, **2013**, 3, 639.
51. K. C. Stylianou, R. Heck, S. Y. Chong, J. Bacsa, J. T. A. Jones, Y. Z. Khimyak, D. Bradshow, M. J. Rosseinsky, *J. Am. Chem. Soc.*, **2010**, 132, 4119.

52. Y. Wang, L. Xu, X. Wei, X. Li, H. Ågren, W. Wua and Y. Xie, *New J. Chem*., **2014**, 38, 3227.
53. G. G. Malliaras, J. R. Salem, P. J. Brock, C. Scott, *Phys. Rev. B*, **1998**, 58, R13411.
54. C. Goh, R. J. Kline, M. D. McGehee, E. N. Kadnikova, J. M. J. Fréchet, *Appl. Phys. Lett.*, **2005**, 86, 12110.
55. Y. Liang, D. Feng, Y. Wu, S. –T. Tsai, G. Li, C. Ray, L. Yu, *J. Am. Chem. Soc.*, **2009**, 131, 7792.
56. Z. B. Wang, M. G. Helander, M. T. Greiner, J. Qiu, Z. H. Lu, *J. Appl. Phys.*, **2010**, 107, 034506.
57. K. Vandewal, K. Tvingstedt, A. Gadisa, O. Inganäs, J. Manca, *Nat. Mater.*, **2009**, 8, 904.
58. M. D. Perez, C. Borek, S. R. Forrest, M. E. Thompson, *J. Am. Chem. Soc.,* **2009**, 131, 928.

Chapter 4

Small Molecule Bulk-Heterojunction Solar Cells Composed of Two Discrete Organic Semiconductors

Abstract

Small molecule bulk-heterojunction (BHJ) solar cells were fabricated by using two disk-shaped organic semiconductors. Perylene-3,4,9,10-tetracarboxylic acid diimide (PDI) derivatives were used as a non-fullerene electron acceptor component for the BHJ solar cells. The attachment of thiophene units with the PDI core enhanced the solar cell performance.

4-1 Introduction

Solution-processed BHJ solar cells have been investigated as a promising candidate for low-cost, flexible, and scalable solar cells.[1] Spontaneous phase segregation of electron donor and acceptor components in the active layer improves the power conversion efficiency (PCE) of these cells.[2] Whereas numerous π-conjugated oligomers and polymers have been developed as donor components for cells[3], fullerene derivatives have been typically used as an accepter component.[4] These derivatives have several drawbacks, such as a low absorption coefficient in the visible region and difficulty in tuning their energy levels. To avoid these drawbacks, non-fullerene acceptors have been designed and synthesized.[5] Perylene-3,4,9,10-tetracarboxylic acid diimide (PDI) derivatives have been receiving attention as an n-type organic semiconductor in several organic-based devices. Large absorption coefficients, good electron accepting properties, and good thermal stabilities of PDI derivatives are favorable for the acceptor components in BHJ solar cells.[6] In addition, the derivatives exhibit high electron mobility in the solid state. In this context, PDI derivatives have been incorporated as the non-fullerene electron-accepting component in the cells. Recently, Zhong et al. reported on a PCE above 6% of PDI-based BHJ solar cells that use narrow-band-gap semiconducting polymers.[7]

We reported on the performance of small molecule BHJ (SM BHJ) solar cells containing self-organized stacks of disk-shaped pyrene-cored donors.[8] Modification by varying the substitution at different positions of the pyrene ring allows the tuning of optical and electronic properties, and the molecular shape of pyrene derivatives affects the molecular packing in the solid state. Pyrene-cored donors with linear oligothiophenes were organized into one-dimensional stacks through intermolecular π-π interaction, and the π-π overlap within the stacks provided an efficient transport pathway for charge or energy. In this chapter, we report on the solar cell performance of heterojunction active layers composed of pyrene-cored donors and non-fullerene PDI derivatives. Although a lot of studies have been focused

on replacing fullerenes with non-fullerene acceptors in polymer-based BHJ solar cells,[5,9] SM BHJ solar cells using non-fullerene acceptors are scarcely studied.[10] Morphological control in heterojunction active layers is difficult for the small molecules. The molecular ordering and segregation size in the active layers are important requirements to improve the photovoltaic performance of SM BHJ solar cells. We found that the phase-segregated nanostructure of PDI derivatives in heterojunction layers with pyrene-cored donor **1** was adjusted by the introduction of thiophene units at the bay positions of perylene core (chart 1). SM BHJ solar cells composed of **1** and PDI derivatives were fabricated and investigated their properties.

4-2 Results and Discussion

4-2-1 Synthesis of PDI Derivatives

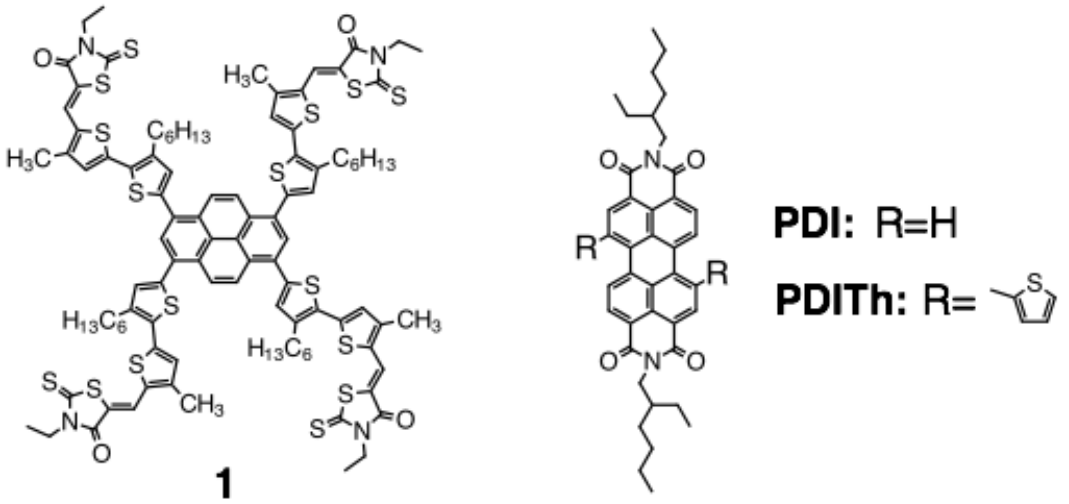

Chart 1

Two PDI derivatives, **PDI** and **PDITh**, were synthesized in according with the reported method.[11] Thermogravimetric analyses (TGA) of **PDI** and **PDITh** showed good thermal stability at a decomposition temperature above 400˚C under a N_2 atmosphere (Figure 1).

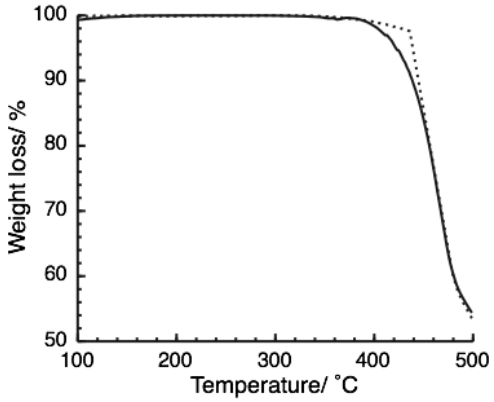

Figure 1. TGA profiles for **PDI** (solid) and **PDITh** (dotted) at scan rate of 10˚C/ min.

4-2-2 Optical and Electrochemical Properties

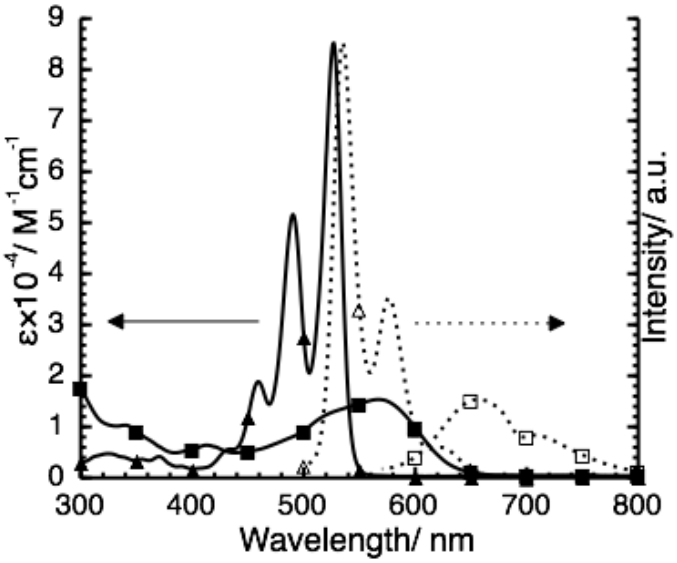

Figure 2. UV-Vis absorption (solid) and florescence (dotted) spectra of **PDI** (triangles) and **PDITh** (squares) in chloroform.

The absorption and fluorescence spectra of **PDI** and **PDITh** in $CHCl_3$ are shown in Figure 2. **PDI** showed a sharp absorption peak at 526 nm with a e value of 8.53×10^4 M^{-1} cm^{-1}. In comparison, the absorption maximum of **PDITh** was red-shifted to λ_{max} = 567 nm with considerable peak broadening and low resolved vibronic fine structure. The fluorescence maximum of **PDITh** was red-shifted by 120 nm compared with **PDI**. This is due to the intramolecular charge transfer from thiophene to the perylene core along with effective π-conjugation.[11]

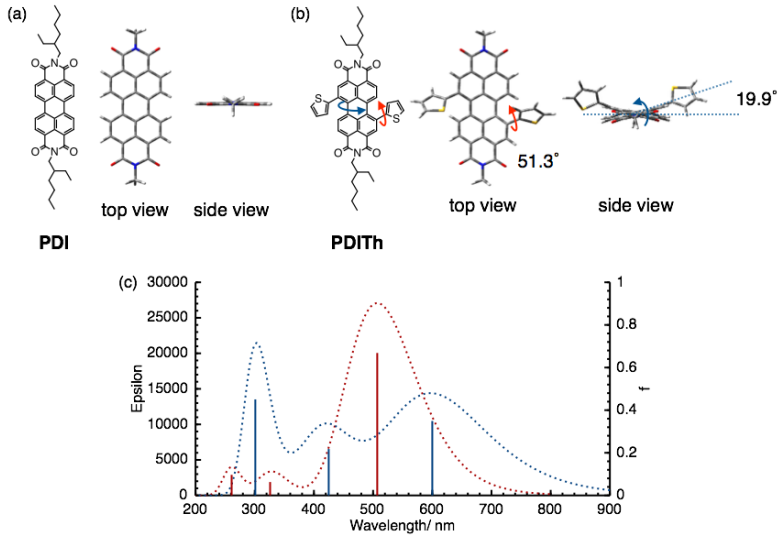

Figure 3. Optimized molecular geometries of **PDI** (a) and **PDITh** (b) by DFT calculation with B3LYP 6-31G* level. (c) Calculated molar extinction coefficients and oscillator strength of **PDI** (red) and **PDITh** (blue).

The optimized structures of the **PDI** and **PDITh** were calculated by density functional theory (DFT) calculation. The relationship between the calculated molar extinction coefficient of **PDI** and **PDITh** was in good agreement with the experimental results. According to the optimized structure of **PDITh**, the central six-membered ring of the perylene core was highly twisted with a dihedral angle of 19.9˚, as shown in Figure 3. The bathochromic shift and loss of vibronic fine structure in **PDITh** resulted from the loss of planarity and rigidity of the perylene diimide chromophore caused by the introduction of thiophene units at the bay positions of the perylene core.[12]

The electrochemical properties of the **PDI** and **PDITh** were investigated by cyclic voltammetry. The reduction half-wave potentials of the **PDI** and **PDITh** were observed at -0.98 and -0.93 V (*vs.* Fc/Fc^{+}), respectively. The HOMO and LUMO energy levels of both compounds were calculated by using the reduction potentials and optical band gap (Figure 4). The optical energy gaps of **PDI** and **PDITh** were estimated to be 2.14 and 1.99 eV from the onset of the absorption bands of the thin films. The HOMO and LUMO energy levels of **PDI** and **PDITh** were lower than

those of donor component **1**, revealing a sufficient driving force for charge separation and transfer after photo-excitation.

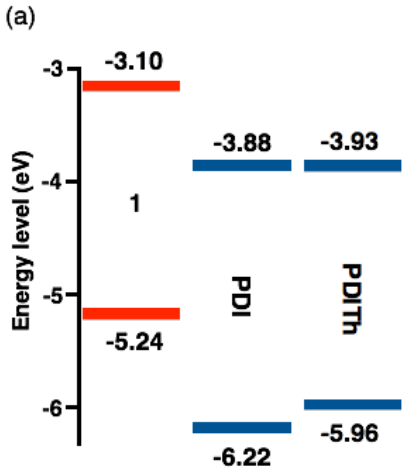

Figure 4. Energy diagram of **1**, **PDI** and **PDITh**.

4-2-3 Self-assembled Properties

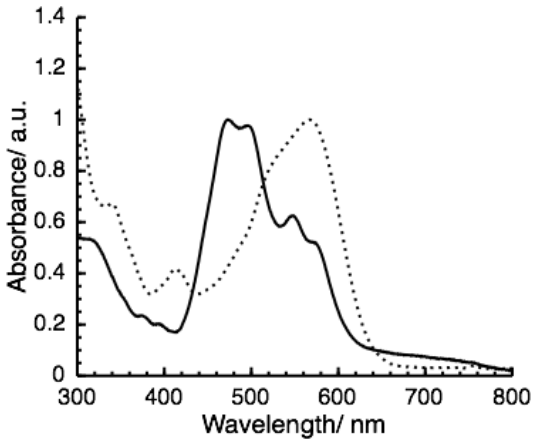

Figure 5. UV-Vis absorption spectra of **PDI** (solid) and **PDITh** (dotted) in thin-films.

The absorption spectra of spin-coated thin films of **PDI** and **PDITh** are shown in Figure 1b. The absorption maxima of the **PDI** film shifted to a shorter wavelength compared with that in the solution, suggesting the formation of

H-aggregates in the solid state.[13] On the contrary, the absorption band of the **PDITh** thin film remained unaltered.

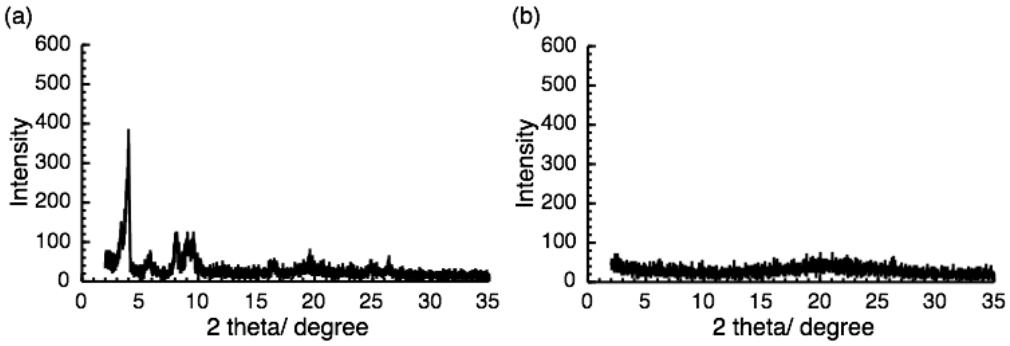

Figure 6. XRD patterns for (a) **PDI** and (b) **PDITh** at RT.

The molecular ordering of the PDI derivatives in the films were investigated by the X-ray diffraction (XRD) of **PDI** and **PDITh** thin films (Figure 6). **PDI** gave several reflection peaks, while **PDITh** had no clear reflection peaks. The differences of absorption spectra and XRD patterns between **PDI** and **PDITh** imply that the twisted structure of **PDITh** inhibited three-dimensional crystallization in the solid.

4-2-4 Photovoltaic Properties

BHJ solar cells were fabricated by using **1** as an electron donor and **PDI** or **PDITh** as an electron acceptor with the device structure of tin-doped indium oxide (ITO)/poly(3,4-rthylenedioxythiophene):polystyrenesulfonate (PEDOT:PSS)/active layer/TiOx/aluminum with a solution process (Figure 7). The cleaned ITO electrode was modified by spin-coating of PEDOT:PSS as a hole-extraction/electron-blocking layer with a 40 nm thickness. The active layer was prepared from a $CHCl_3$ solution of **1** and PDI derivatives onto the PEDOT:PSS modified ITO anodes in an argon filled glove box ($[O_2]$<0.1 ppm and $[H_2O]$<0.1 ppm), and the thickness was typically 50 - 80 nm. The TiOx layer has been used as an electron-collection/hole-blocking layer in BHJ solar cells.[14] Finally, an aluminum cathode was deposited through a shadow mask by thermal evaporation under vacuum.

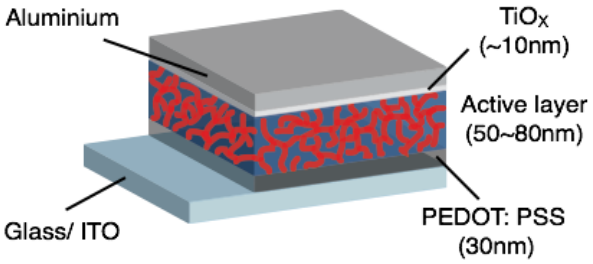

Figure 7. Device structure of BHJ solar cells.

The performance of BHJ solar cells composed of **1**/ **PDI** or **PDITh** with a composition ratio of 2:1 w/w are summarized in Table 1. The PCE of **1**/**PDITh** was slightly higher than that of **1**/**PDI**, which was mainly due to the increase of short-circuit current density (J_{sc}). Both cells yielded high open-circuit voltages (V_{oc}) above 1.0 V. High V_{oc} values were also observed in the cells of **1** with fullerene acceptors. The PCEs decreased by changing the composition ratio of **1**/**PDITh** from 2:1 w/w to 1:1 w/w or 3:1 w/w (Table 1).

Table 1. Summary of device parameters of BHJ solar cells based on mixed active layers of **1**/ **PDI** and **PDITh**.

Active layer (weight ratio)	DIO /%	V_{oc}/ V	J_{sc} /mA cm^{-2}	FF	PCE /%
1/ **PDI** (2:1)	0	1.03	0.42	0.26	0.11
1/**PDITh** (1:1)	0	0.52	0.09	0.19	0.01
1/**PDITh** (2:1)	0	1.06	0.73	0.21	0.16
1/**PDITh** (3:1)	0	0.84	0.47	0.24	0.09
1/**PDITh** (2:1)	0.6	1.11	2.30	0.28	0.73

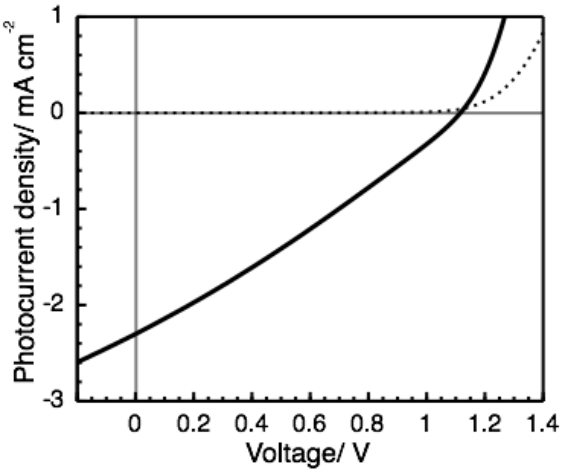

Figure 8. Photocurrent voltage curve obtained with BHJ solar cells based on **1**/ **PDITh** (2:1 w/w) with 0.6% DIO blended active layers under a standard global AM 1.5 solar condition (solid line) and dark current (dotted line).

Adding polar and high boiling point additives such as 1,8-diiodeoctane (DIO), 1,8-octanedithiol and 1-chloronaphthalene can tune the molecular ordering and segregation size in the active layers, and the photovoltaic performance of SM BHJ solar cells has been improved by the addition of additives.[15] Figure 8 shows *J-V* and IPCE characteristics of an optimized device of **1**/**PDITh** with DIO. When adding the 0.6 v/v% of DIO to **1**/**PDITh**, the PCE was significantly improved to 0.72% with a V_{oc} of 1.11V, J_{sc} of 2.30 mA/ cm^2 and *FF* of 0.28. In contrast, the PCE of the **1**/**PDI** cell did not improve by the addition of DIO, which is probably result from the over aggregation of **PDI** in the active layer. The series resistance (R_s) of the **1**/**PDITh** cell was decreased from 1406 to 274 Ω cm^{-2} by the addition of DIO.

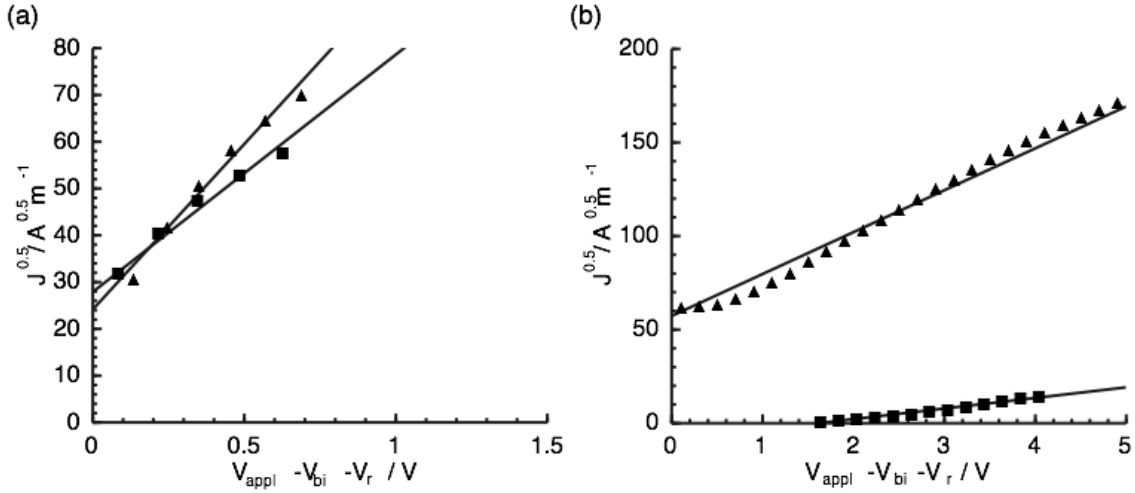

Figure 9. $J^{0.5}$-V plots for (a) hole and (b) electron devices based **1**/**PDITh**(2:1) blended active layer with different concentration of DIO none (triangle) and 0.6% (square) under dark condition. The solid lines are fitted with the data points.

Table 2. Hole and electron mobilities of **1**/**PDITh**(2:1) blended active layer with different concentration of DIO none and 0.6% .

Active layer (Weight ratio)	Additives/ v/v%	μ_hx10^{-4}/ cm^2 V^{-1} s^{-1}	μ_ex10^{-5} / cm^2 V^{-1} s^{-1}
1/**PDITh** (2:1)	0	1.80±0.67	0.23±0.02
1/**PDITh** (2:1)	0.6	3.70±0.91	1.62±0.66

Hole and electron mobilities of **1**/**PDITh** were determined by using the space-charge limited current (SCLC) method (Figure 9, Table 2).[16] When DIO was used as the additive for the active layers, the hole (μ_h) and electron (μ_e) mobilities of **1**/**PDITh** were significantly improved (μ_h: 1.8 to 3.7×10^{-4} cm^2 V^{-1} s^{-1} and μ_e: 0.23 to 1.62×10^{-5} cm^2 V^{-1} s^{-1}).

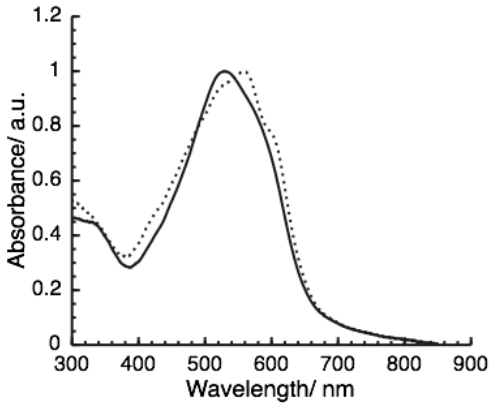

Figure 10. Absorption spectra of **1**/**PDITh** (2:1) blended active layer with different concentration of DIO none (solid) and 0.6% (dotted).

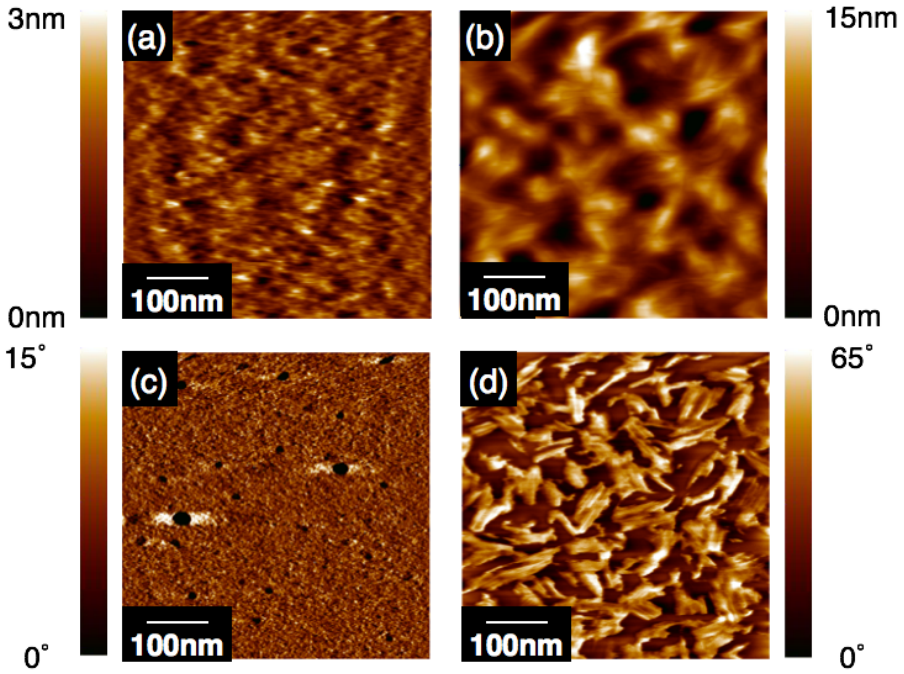

Figure 11. Tapping-Mode AFM height (a, b) and phase (c, d) images of **1**/**PDITh** (2:1) blended active layer with different concentration of DIO (a, c) none and (b, d) 0.6%

The UV-Vis absorption spectra of **1**/**PDITh** with 0.6 v/v% of DIO showed several shoulder peaks around 620 nm, indicating the formation of ordered stacks of the π-conjugated molecules (Figure 10). The morphological change of the **1**/**PDITh** layer with DIO was investigated by using a tapping mode atomic force microscope (AFM). The phase and height images demonstrate that the domain size in the

1/**PDITh** layer was enlarged by using DIO (Figure 11). The enlarged phases helped to form continuous interpenetrating networks for charge transportation.

The incident photon to current conversion efficiency (IPCE) spectrum of the **1**/**PDITh** cell is shown in Figure 12a. The IPCE spectrum of the **1**/**PDITh** cell shows 15% of the maximum IPCE values at 560 nm, and the estimated J_{sc} value from the overlap integral of IPCE with the solar spectrum almost agreed with the experimental value of the **1**/**PDITh** cell.[17] Because of the low absorption coefficients of the fullerene derivatives in the visible light region, the maximum wavelength of the IPCE spectrum of **1**/$PC_{61}BM$ was 520 nm (Figure 12b). The IPCE spectrum of the **1**/**PDITh** cell almost agreed with the sum of the absorption spectra of **1** and **PDITh**, indicating the contribution of **PDITh** to photocurrent generations in the visible light region (Figure12c). The use of **PDITh** as the electron acceptor component could expand the light-harvesting area of BHJ solar cells.

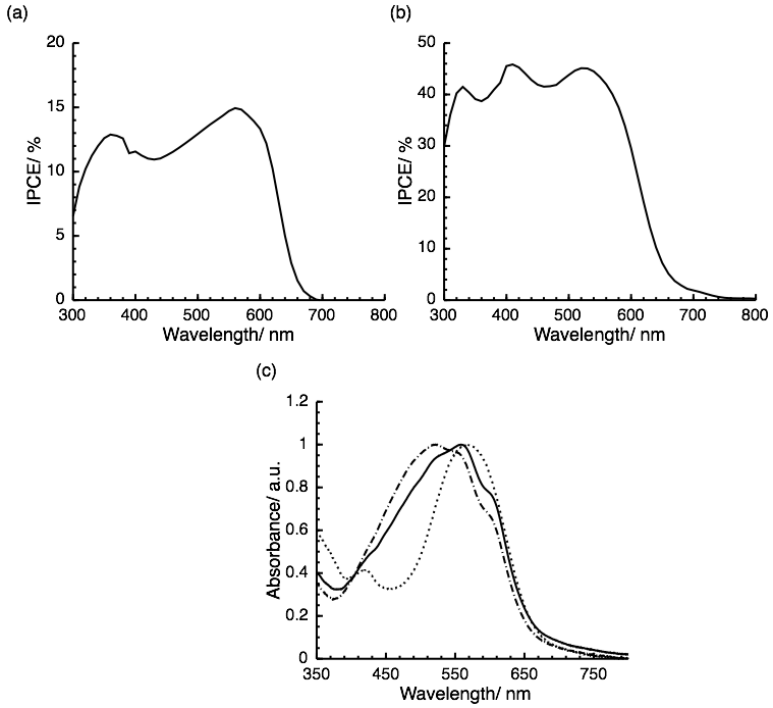

Figure 12. Incident photon-to-current conversion efficiency spectrum based on (a) **1**/ **PDITh** (2:1 w/w) with 0.6% DIO and (b) **1**/ **$PC_{61}BM$** (1:3 w/w) blended active layers. (c) Absorption spectra of **1** (dot-dash), PDITh (dotted) and **1**/**PDITh**(2:1) blended active layer with 0.6% of DIO (solid)

4-3 Conclusions

In conclusion, we demonstrated the fabrication of SM BHJ solar cells with non-fullerene PDI derivatives for the acceptor component. Introducing two thiophenes at the bay positions of perylene core changed their optical and redox properties as well as the molecular ordering in the solid state. The HOMO and LUMO energy levels of the twisted **PDITh** are adequate for the operation of BHJ solar cells. SM BHJ solar cells were fabricated by using a mixed solution of electron-donating **1** and electron-accepting **PDITh**. Optimizing the nanostructure in blended film by adding DIO greatly improved the PCE values from 0.16% to 0.73% while keeping high V_{oc} values above 1 V. The use of PDI derivatives leaded to an expansion of the light-harvesting area of SM BHJ solar cells. However, the PCEs of the **1**/**PDITh** cell were much lower compared with those of the **1**/$PC_{61}BM$ cell (Table 1).[8] The large series resistance of **1**/ PDIs devices is major reason for the low *FF*.[10b] This is mainly due to the low carrier mobility compare with the highly efficient SM BHJ solar cells using non-fullerene acceptors (>10^{-3} cm^2 V^{-1} s^{-1}).[16a] Investigations are underway to optimize the structure of PDI derivatives to improve the PCEs in SM BHJ solar cells.

4-4 Experimental Section

4-4-1 General

NMR spectra were recorded on a Bruker AVANCE 400 FT NMR spectrometer at 400.13 MHz and 100.61MHz for ^1H and ^{13}C in $CDCl_3$ solution. Chemical shifts are reported relative to internal TMS. UV-Vis spectra were measured on a JASCO V-650. MALDI-TOF mass spectra were obtained on a Bruker autoflex with dithranol as matrix. The XRD patterns were obtained with a Rigaku XRD-DSC with Cu Ka radiation. Atomic force microscopy images were acquired in tapping mode by a JEOL JSPM-5400 system. The samples for AFM were prepared by the spin-coating of $CHCl_3$ solutions on PEDOT: PSS coated quartz substrate. Cyclic voltammetric measurements were recorded on an ALS 700 potentiostat using a three cell electrode system with a Pt working electrode, a Pt counter electrode and an Ag/AgCl reference electrode. $TBAPF_6$ was used as the electrolyte.

4-4-2 Device Fabrications

Indium tin oxide (ITO) patterned glass substrates were cleaning with sonication in neutral detergent, distilled water, acetone and 2-propanol. The substrates were dried and apply UV-O_3 treatment for 30min. Electron blocking layer were prepared by spin-coated the PEDOT:PSS (H. C. Starck) with a thickness of 40 nm. The substrates were baked at 180˚C for 30 min. A solution containing a mixture of pyrene-cored donors and PDI derivatives as acceptor in chloroform were spin-coated onto the PEDOT: PSS layer, and apply thermal annealing treatment at f80˚C for 10min in the argon filled globe box. Titanium oxide solution was spin-coated onto the active layer then place in air for 30min. The counter electrode of aluminum was prepared by thermal deposition with a thickness of 100nm. Current density-voltage (*J-V*) characteristics were measured using a Keithley 2400 Source Measure Unit. Performance of BHJ solar cells devices was measured under one-sun conditions (AM 1.5, 100mW/cm^2) by a solar simulator (XES-151S, Sanei electric Inc.).

4-4-3 Hole and Electron Mobility Measurements

Hole-mobility of donor materials were carried out with the device structure of ITO/PEDOT:PSS/active layer/Au for hole and ITO/TIPD/Active layer/Al for electron by taking current-voltage curves in the range of 0-8V.[13] The hole-mobility was calculated using the space charge current limited (SCLC) method using the Mott-Gurney square law[14] (Eq. 1),

$$J = \frac{9}{8}\,\varepsilon_0 \varepsilon_r \mu \frac{V^2}{L^3} \qquad (1)$$

where J is the current density, ε_0 is the permittivity of free space (8.85×10^{-12} F m^{-1}), ε_r is the relative dielectric constant of the transport of medium (assumed to be 3), μis the hole mobility, V is the internal voltage in the device ($V = V_{appl} - V_r - V_{bi}$, where V_{appl} is the applied voltage in the device, V_r is voltage drop due to the contact resistance and V_{bi} is the built-in voltage due to relative work function difference

between the two electrodes. The V_{bi} can be determined from the transition between the Ohmic region and SCLC region and *L* is the thickness of film.

4-5 References

1 S. Günes, H. Neugebauer, N. S. Sariciftci, *Chem. Rev.,* **2007**, *107*, 1324.

2 A. J. Heeger, *Adv. Mater.,* **2014**, *26*, 10.

3 A. Mishra, P. Bäuerle, *Angew. Chem. Int. Ed.,* **2012**, *51*, 2020.

4 Y. He, Y. Li, *Phys. Chem. Chem. Phys*., **2011**, *13*, 1970.

5 a) A. F. Eftaiha, J-P. Sun, I. G. Hill, G. C. Welch, *J. Mater. Chem. A,* **2014**, **2**, 1201. b) Y. Lin, X. Zhan, *Mater. Horiz.*, **2014**, *1*, 470.

6 C. Huang, S. Barlow, S. R. Marder, *J. Org. Chem*., **2011**, *76*, 2386.

7 Y. Zhong, M. T. Trinh, R. Chen, W. Wang, P. P. Khlyabich, B. Kumar, Q. Xu, C.-Y. Nam, M. Y. Sfeir, C. Black, M. L. Steigerwald, Y-L. Loo, S. Xiao, F. Ng, X-Y. Zhu, C. Nuckolls, *J. Am. Chem, Soc*., **2014**, *136*, 15215.

8 K. Takemoto, M. Kimura, *RSC Advances*, **2014**, *4*, 64589.

9 a) Y. Zang, C.-Z. Li, C.-C. Chueh, S. T. Williams, W. Jiang, Z.-H. Wang, J.-S. Yu, A. K.-Y. Jen, *Adv. Mater*., **2014**, *26*, 5708. b) T. Earmme, Y. J. Hwang, S. Subramaniyan, S. A. Jenekhe, *Adv, Mater*., **2014**, *26*, 6080. c) D. Mori, H. Benten, I. Okada, H. Ohkita, S. Ito, *Energy. Environ. Sci*., **2014**, *7*, 2939. d) P. E. Hartnett, A. Timalsina, H. S. S. R. Matte, N. Zhou, X. Guo, W. Zhao, A. Facchetti, R. P. H. Chang, M. C. Hersam, M. R. Wasielewski, T. J. Marks, *J. Am. Chem. Soc*., **2014**, *136*, 16345.

10 a) A. Sharenko, D. Gehrig, F. Laquai, T.-Q. Nguyen, *Chem. Mater*., **2014**, *26*, 4109. b) Y. Chen, A. Tang, X. Zhang, Z. LU, J. Huang, C. Zhan, J. Yao, *J. Mater. Chem. A,* **2014**, *2*, 1869. c) J. D. Douglas, M. S. Chen, J. R. Niskala, O. P. Lee, A. T. Yiu, E. P. Young, J. M. J. Fréchet, *Adv. Mater*., **2014**, *26*, 4313.

11 a) S. Chen, Y. Liu, W. Qiu, X. Sun, Y. Ma, D. Zhu, *Chem. Mater*., **2005**, *17*, 2208. b) S. Vajiravelu, L. Ramunas, G. J. Vidas, G. Valentas, J. Vygintas, S. Valiyaveettil, *J. Mater. Chem*., **2009**, *19*, 4268.

12 a) Z. Chen, M. Debije, T. Debaerdemaker, P. Osswald, F. Wurthner, *ChemPhysChem*. **2004**, *5*, 137. b) C.-C. Chao, M.-k. Leung, *J. Org. Chem*., **2005**, *70*, 4323.

13 T. van der Boom, R. T. Hayes, Y. Zhao, P. J. Bushard, E. A. Weiss, M. R. Wasielewski, *J. Am. Chem. Soc*., **2002**, *124*, 9582.

14 A. Hayakawa, O. Yoshikawa, T. Fujieda, K. Uehara, S. Yoshikawa, *Appl. Phys. Lett*., **2007**, *90*, 163517.

15 a) Y. Sun, G. C. Welch, W. L. Leong, C. J. Takacs, G. C. Bazan, A. J. Heeger, *Nat. Mater*., **2012**, *11*, 44. b) J. Liu, Y .Sun, P. Moonsin, M. Luik, C. M. Proctor, J. Lin, Ben. B. Hsu, V. Promarak, A. J. Heeger, T.-Q. Nguyen, *Adv. Mater*., **2013**, *25*, 5898. c) H. Fan, H. Shang, Y. Li, X. Zhan, *Appl. Phys. Lett*., **2010**, *97*, 133302.

16 a) J. Huang, X. Wang, X. Zhang, Z. Niu, Z. Lu, B. Jiang, Y. Sun, C. Zhan, J. Yao, *ACS Appl. Mater. Interfaces,* **2014**, *6*, 3853. b) G. G. Malliaras, J. R. Salem, P. J. Brock, C. Scott, *Phys. Rev. B,* **1998**, *58*, R13411. c) C. Goh, R. J. Kline, M. D. McGehee, E. N. Kadnikova, J. M. J. Fréchet, *Appl. Phys. Lett.,* **2005**, *86*, 12110. d) Y. Liang, D. Feng, Y. Wu, S. –T. Tsai, G. Li, C. Ray, L. Yu, *J. Am. Chem. Soc.,* **2009**, *131*, 7792.

17 J. D. Servaites, M. A. Ratner, T. J. Marks, *Appl. Phys. Lett*., **2009**, *95*, 163302.

Chapter 5

Organic Sensitizers Including π-Conjugated Fluorene-Benzothiadiazole Bridge for Dye-sensitized Solar Cells

Abstract

A series of novel amphiphilic fluorene-benzothiadiazole-bridged organic sensitizer (coded as MR dyes) were designed for dye-sensitized solar cells (DSSCs). The DSSCs based on **MR-2** and **MR-3** exhibited power conversion efficiencies of 3.7% and 4.0% under one-sun condition.

5-1 Introduction

Dye-sensitized solar cells (DSSCs) based on nanocrystalline TiO_2 offer a low-cost and scalable route to develop highly efficient photovoltaic cells.[1] Typical DCCSs consist of a porous TiO_2 semiconductor electrode adsorbed with light-harvesting sensitizers, a Pt counter electrode, and a redox electrolyte containing redox shuttles. Much effort has been devoted to de developing efficient materials and optimizing device structure to enhance the overall power conversion efficiency of DSSCs.[2] At present, the conversion efficiency of state-of-art DSSCs based on panchromatic ruthenium (II) polypyridyl complexes approaches above 11% under standard illumination.[3] Cosensitization of TiO_2 by sensitizers has been demonstrated to broaden the spectral response of DSSCs in visible portion of the solar spectrum. Many sensitizers have been designed and synthesized to enhance the cell performance.[4] Since the first report on metal-free sensitizers in DSSCs by Hara et al.,[5] metal-free organic sensitizers have attracted much attension.[6] The organic sensitizers possess the following advantages: 1) higher molar extinction coefficients than ruthenium dyes, 2) easy molecular design for rational electron and hole transport at the interface between TiO_2 and the redox electrolyte, and 3) lower-cost materials than ruthenium complexes. General design of organic sensitizers for DSSCs consists of a donor-acceptor substituted π-conjugated bridge where the acceptor side is attached to the TiO_2 surface. Considerable progress has been made in recent years, and metal-free sensitizers with conversion efficiencies in the range of 8 to 9% in DSSCs have been reported.[6]

Enhancement of the conversion efficiency of DSSCs requires the expansion of the absorption region of organic sensitizers. π-conjugated oligomers composed of thienyl or vinyl units have been used as the π-conjugated bridge of organic sensitizers.[6] These bridges can expand the absorption region as π-conjugation increases. However, open-circuit voltages (V_{oc}) of these organic sensitizers that have a π-conjugated bridge were lower than those of ruthenium complexes due to the enhanced charge recombination. In this chapter, π-conjugated bridged need to be

explored further.[7] Poly(9,9-dioctylfluorene-*co*-benzothiadiazole) (F8BT) has been widely used as a highly efficient green-light-emitting material in organic light-emitting diodes and organic-based photovoltaic cells.[8] In these devices, F8BT plays the role of the electron-transport agent. Recently, benzothiadiazole units have also been used as a molecular unit of low-band-gap polymers for thin-film transistors and bulk-heterojunction photovoltaic cells with fullerenes.[9] In this study, we focused on the repeating unit in F8BT, and we synthesized a series of new organic sensitizers **MR-1**, **MR-2**, and **MR-3**, in which donor and acceptor units were bridged with a fluorene-benzothiadiazole unit. Lin et al. reported the performances of DSSCs using organic sensitizers containing benzothiadiazole units in theπ-conjugated bridge.[10] They also demonstrated a highly efficient vacuum-deposited organic solar cells using a low-energy-gap organic dye including benzothiadiazole units combined with C_{70}.[11] However, the fluorine-benzothiadiazole unit has not been exploited as a π-conjugated bridge in the organic sensitizers of DSSCs. The fluorene-benzothidiazole bridge would affect the photoinduced charge separation and migration processes in DSSC systems.

5-2 Results and Discussion

5-2-1 Synthesis of MR dyes

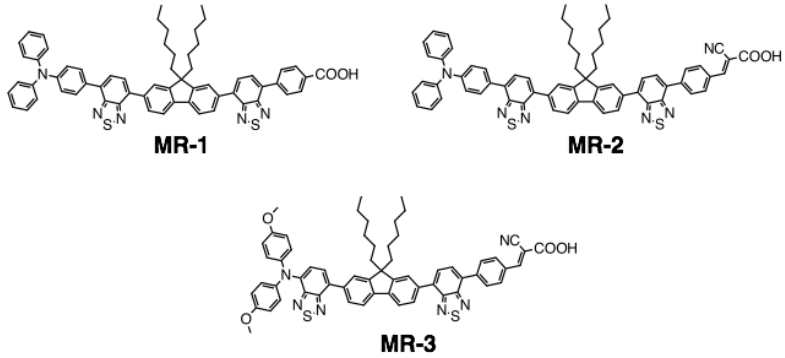

Chart 1.

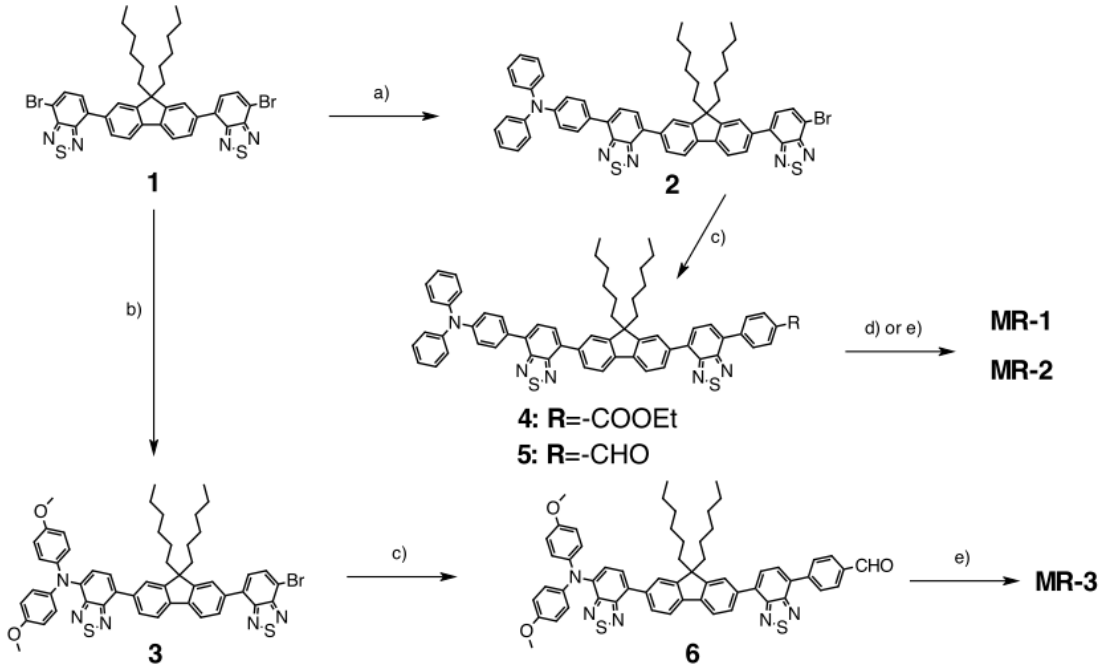

Scheme 1. a) 4-(diphenylamino)phenylboronic acid, $[Pd(PPh_3)_4]$, K_2CO_3, toluene/ THF; b) bis(4-methoxyphenyl)amine, $[Pd_2(dba)_3]$, P(*t*-Bu)$_3$, *t*-BuONa, toluene; c) 4-ethoxycarbonylphenylboronic acid or 4-formylphenylboronic acid, $[Pd(PPh_3)_4]$, K_2CO_3, toluene/ THF; d) NaOH(aq) and HCl; e) $CNCH_2COOH$, piperidine, MeCN.

We synthesized three metal-free sensitizers **MR-1**, **MR-2**, and **MR-3** (Chart 1) to investigate the structural dependence of sensitizers on the performance of DSSCs (Scheme 1). The Suzuki coupling reaction of 9,9-dihexylfluorene-2,7-diboronic acid with three equivalents of 4,7-dibromobenzothiadiazole yielded a π-conjugated bridge **1** of **MR-1**, **MR-2**, and **MR-3**. One bromide in **1** was coupled with 4-(diphenylamino)phenylboronic acid or bis(4-methoxyphenyl)amine in the presence of palladium catalysts to give **2** and **3**.[12] The other bromide in **2** or **3** was reacted with 4-ethoxycarbonylphenylboronic acid or 4-formylphenylboronic acid. The target compounds **MR-1**, **MR-2**, and **MR-3** containing the fluorine-benzothiadiazole bridge were obtained from **4** and **5** through several steps. The terminal aldehyde in **5** reacted with cyanoacetic acid to form 2-cyanoacrylic acid as the acceptor. All compounds were fully characterized by ^1H and ^{13}C NMR, FT-IR, and MALDI-TOF-MS.

5-2-2 Optical and Electrochemical Properties

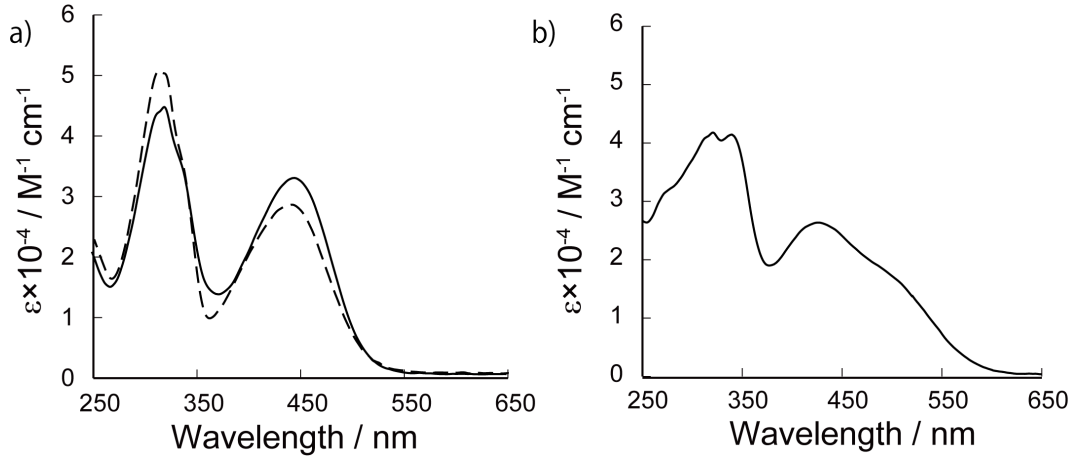

Figure 1. Absorption spectra of a) **MR-1** (dotted line) and **MR-2** (solid line), and b) **MR-3** in CH_2Cl_2.

Table 1. Optical and electrochemical properties of MR dyes

Dye	λ_{abs}/ nm[a]	Log ε[b]	$E_{0\text{-}0}$[c]/ eV	E_{ox}[d]/V	E_{ox}^{*}[e]/V
MR-1	313, 445	4.70, 4.46	2.32	1.16	-1.16
MR-2	320, 445	4.65, 4.52	2.35	1.16	-1.19
MR-3	339, 427, 500 (s)	4.61, 4.42, 4.30	2.14	0.97	-1.17

[a] Maximum of the absorption band in CH_2Cl_2. [b] Extinction coefficient of the absorption band in CH_2Cl_2. [c] Estimated from the onset of the absorption spectra in CH_2Cl_2. [d] Oxidation potentials measured vs. Fc/ Fc^+ in degassed CH_2Cl_2 containing 0.1M TBAP were converted to normal hydrogen electrode (NHE) by addition of +0.63V. [e] Energy of LUMO were estimated by E_{ox} - $E_{0\text{-}0}$.

The absorption maxima (λ) and absorption extinction coefficients (ε) of **MR-1**, **MR-2**, and **MR-3** are listed in Table 1. **MR-1** and **MR-2** exhibited a main absorption peak at 445 nm, which is attributable to π-π* transitions of the conjugated systems (Figure 1).[10] Whereas the position of these absorption bands are almost the same, the absorption extinction coefficient at 445 nm of **MR-2** having the electron-accepting cyanovinyl moiety is higher than that of **MR-1**. **MR-1** and **MR-2** emitted a fluorescence peak at 626nm by the excitation at the absorption maxima.

Fluorescence quantum yield (Φ_F) of MR-2 (Φ_F = 1 %) was significantly lower than that of **MR-1** (Φ_F = 38 %) due to an intermolecular energy transfer.

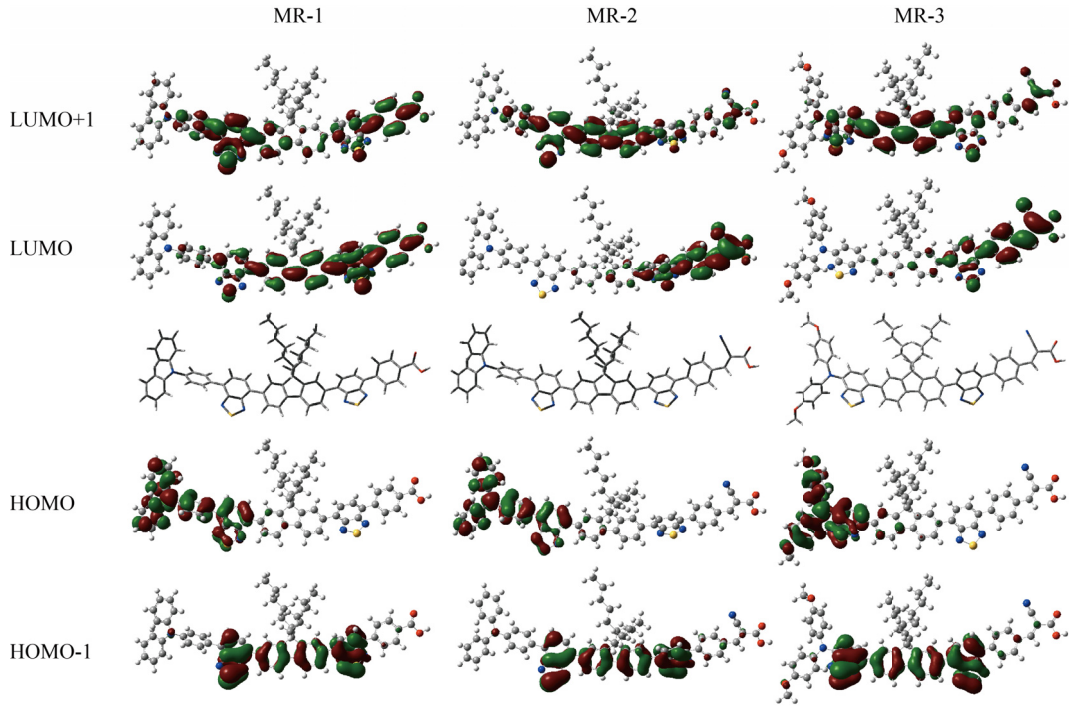

Figure 2. Molecular orbital diagrams for **MR-1**, **MR-2**, and **MR-3** obtained by DFT calculation with B3LYP/6-31G*.

Density functional theory (DFT) calculations were conducted for the compounds to gain insight into the equilibrium geometry and electronic structures for the frontier orbitals of the compounds. The dihedral angels between aromatic segments in the calculated structure of **MR-1** and **MR-2** are found to be 34-37˚. The large twisted angles of fluorine-benzthiadiazole bridges in **MR-1** and **MR-2** do not induce red-shifting and broadening of the absorption spectra.[13] The electron density distributions of the highest occupied molecular orbital levels (HOMOs) of **MR-1** and **MR-2** are mainly populated over the triphenylamine and benzothiadiazole block (Figure 2). The lowest unoccupied molecular orbital level (LUMO) of **MR-2** is delocalized on the side of the cyanoacrylic acid terminate without overlapping the HOMO, which illustrates that the HOMO and LUMO are completely separated in **MR-2**. On the other hand, the LUMO of MR-1 partially overlaps with the HOMO. The HOMO-LUMO excitation in **MR-2** would shift the electron density distribution

from thetriohenylamine unit to the cyanoacrylic acid moiety, which facilitates an efficient electron injection from the exited dyes to the TiO_2 electrode.

To determine the first oxidation potentials (E_{ox}) of **MR-1** and **MR-2** in solutions, cyclic voltammetry measurements were performed in dry dimethylformamide (DMF) containing 0.1M TBAP as asupporting electrolyte. The cyclic voltammograms of **MR-1** and **MR-2** reveal a reversible one-electron oxidation at +1.16V vs. NHE attributable to oxidation of the triphenylamine unit.[6] The E_{ox} of **MR-2** agrees with that of **MR-1**, indicating that the electron-accepting cyanovinyl moiety does not affect the potential of the triphenylamine unit through the twisted conjugated bridge. Changing the donor unit in the organic sensitizer can also tune the wavelength range, absorption capability, and other characteristics required for DSSCs.[6] The dye **MR-3**, in which the bis(4-methoxyphenyl)amine unit was directly attached to the fluorine-benzothiadiazole bridge, shows a red-shifted absorption maxima compared to that of **MR-2** (Table 1, Figure 1) and does not emit a fluorescence peak by the excitation at the absorption maximum of **MR-3**. The E_{ox} of **MR-3** shifts negatively by 90 mV more than that of **MR-2**, demonstrating the extent of destabilization of HOMO caused by the bis(4-methoxyphenyl)amine unit. This indicates that the arylamine unit in **MR-3** could be easily oxidized into its radical cation. The red-shifted absorption to thestrong electron-donating nature of the bis(4-methoxyphenyl)amine unit in **MR-3**.

5-2-3 Photovoltaic Properties

MR dyes were adsorbed onto the surface of nanocrystalline TiO_2 through theformation of bonds between the carboxylic acid and the TiO_2 surface. The TiO_2 electrodes (4.9 μm thick) were immersed in toluene solution of dye (0.3mM) for 12h to achieve the dye-stained TiO_2 electrodes. The photovoltaic performance of MR dyes as the sensitizers in DSSCs were evaluated with a sandwich DSSC cell using the redox electrolyte. The current-voltage (*I-V*) characteristics were measured under simulated solar irradiation (one sun =100mW cm^{-2} 1.5 air mass global) and the device performance containing N719 adsorbed TiO_2 electrode is provided as a benchmark.

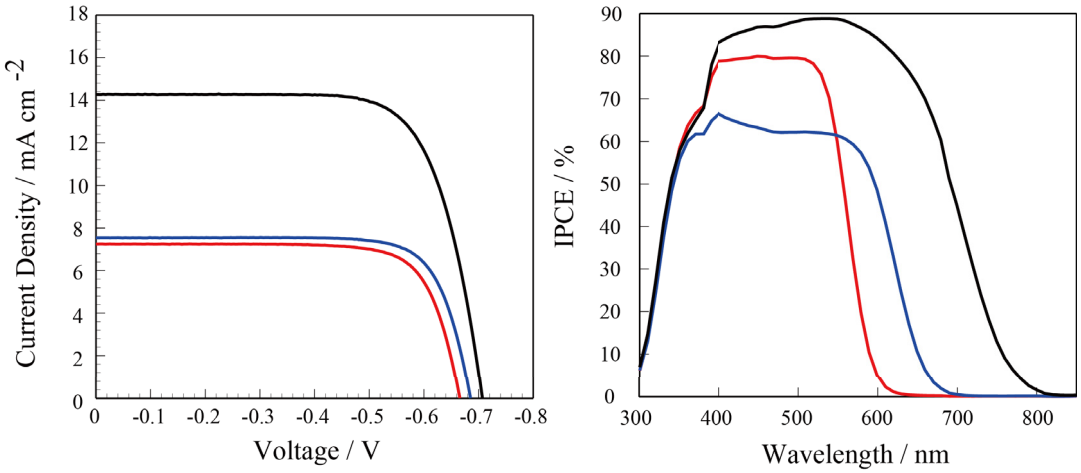

Figure 3. a) Current-voltage characteristics and b) IPCE spectra of **MR-2** cell (red), **MR-3** cell (blue), and **N719** (black) cell. Thickness of TiO_2 electrode on FTO is 8.0 + 4.0 um.

Table 2. DSSCs performance of MR dyes.

Dye	$\Gamma^a/\times10^{-10}$ mol cm^{-2}	TiO_2[b]	J_{sc}/mA cm^{-2}	V_{oc}/ V	FF[c]	η / %
MR-1	65	4 + 0	3.9	0.65	0.71	1.8
MR-2	70	4 + 0	4.9	0.66	0.74	2.4
	70	8 + 4	7.1	0.67	0.76	3.7
MR-3	70	4 + 0	5.2	0.65	0.71	2.4
	70	8 + 4	7.8	0.68	0.77	4.0
N719	70	8 + 4	14.3	0.71	0.73	7.3

[a] Absorption densities (Γ) of dyes on TiO_2 were determined by measuring the absorbance of dyes that were dissolved from the dye-strained TiO_2 electrode into alkaline solution. [b] The first and second digits indicated the thickness of 20 and 400 nm nanoporous TiO_2 layer in um, respectively. [c] FF = fill factor.

The **MR-2**-sensitizers cell gave the short-circuit photocurrent density (J_{sc}) of 4.9 mA cm^{-2}, V_{oc} of 0.66 V, and fill factor (FF) of 0.74, corresponding to an overall efficiency (PCE) of 2.4 %. The **MR-1**-sensitized cell shows relatively lower J_{sc}, leading to an inferior PCE value of 1.8%. These PCE values are lower than that of N719-sensitized cell under the same conditions. The incident monochromatic photon-to-current conversion efficiency (IPCE) spectra of the **MR-1** and **MR-2** cells followed the absorption features of dyes adsorbed on TiO_2 electrode. The IPCE values of **MR-1** and **MR-2** cells increased steeply from 600 nm and reached a maximum value 50 and 65 %, respectively at 480 nm. The higher IPCE of the **MR-2** cell than that of the **MR-1** call can be ascribed to the efficient electron injection from excited dyes to the TiO_2 electrode. The IPCE spectra of the **MR-1**- and **MR-2**-sensitized cells are narrower that that of the N719 cell, resulting in lower overall efficiencies due to their spectra; limitations. When the TiO_2 thickenss increases to 8.0 μm with 4.0 μm scattering layer, the **MR-2** cell revealed the highest IPCE of 78 % at 480 nm and the PCE of 3.7 % (Figure 3). The comparison of photovoltaic performances between **MR-1** and **MR-2** showed that the electron-accepting cyanoacrylic acid moiety is superior to the carboxylic acid moiety as the absorption site in the fluorine-benzothiadiazole bridge dyes. This is in agreement with the results on the molecular design of dye molecules for the high performance of organic dye-sensitized solar cells.[6]

The **MR-3**-sensitized call appears to have a higher PCE value (4.0 %) than the **MR-2** cell fabricated and measured under the same conditions (Table 2). The V_{oc} of the **MR-2** cell was almost identical to that of the **MR-2** cell. The IPCE spectrum of **MR-3** cell was broader that that of the **MR-2** cells, suggesting a better light-harvesting ability of the **MR-3** (Figure 1). However, the maximum IPCE value of the **MR-3** call was lower than that of the **MR-2** cell. From the DFT calculation of **MR-3** (Figure 3), the electron density of the absorption site in the LUMO was lower than **MR-2** owing to the direct attachment of the bis(4-methoxyphenyl)amine unit into the fluorene-benzothiadiazole bridge. The low electron density of the absorption site of **MR-3** resulted in the low electron injection efficiency in the **MR-3** cell. To

enhance the electron injection efficiency requires the introduction of other electron-accepting units in the absorption sites attached to the π-system.

5-3 Conclusions

We have designed and synthesized a series of MR dyes, in which the electron-donating unit and the electron-accepting absorption site were connected with the low-band-gap fluorene-benzothiadiazole bridge, to investigate the structure-performance relationship in these fluorene-benzothiadiazole-brodged dyes. The attachment of donating and accepting units with the twisted bridge can be tune the optical and electrochemical properties of the dye molecules. The DSSCs with the dye **MR-3** have reached a PCE of 4.0%, which is 55% of the Ru dye N719 cell fabricated under the same conditions. **MR-2** and **MR-3** cells have a V_{oc} and FF comparable to those of N719, but their J_{sc} are lower than that for N719 owing to their narrow light-harvesting are and lower electron injection efficiency. To obtain better solar cell performance of fluorene-benzothiadiazole-bridged dyes, further molecular design is needed to overcome several drawbacks in MR dyes as pointed out in this study.

5-4 Experimental Section

5-4-1 General

NMR spectra were recorded on a Bruker AVANCE 400 FT NMR spectrometer at 400.13 MHz and 100.61MHz for ^{1}H and ^{13}C in $CDCl_3$ solution. Chemical shifts are reported relative to internal TMS. UV-Vis spectra were measured on a JASCO V-650. MALDI-TOF mass spectra were obtained on a Bruker autoflex with dithranol as matrix. Cyclic voltammetric measurements were recorded on an ALS 700 potentiostat using a three cell electrode system with a Pt working electrode, a Pt counter electrode and an Ag/AgCl reference electrode. TBAP was used as the electrolyte.

5-4-2 Materials

Detailed synthetic procedures and characterization of MR dyes

1: A Schlenk flask was charged with 4,7-diboromo-2,1,3-benzothiazole (1.8 g, 6.1 mmol) and $Pd(PPh_3)_4$ (40 mg, 34 μmol) under an Ar atmosphere. Solution of 9,9'-dihexylfluorene-2,7-diboronic acid (0.8g, 1.9 mmol) in THF (14 ml), toluene (12 ml) and 2.0 M K_2CO_3 aqueous solution (11 ml) were prepared and deoxygenated with a steam of Ar, and the mixture was refluxed under Ar for 48 h. The reaction mixture was poured into a mixture of H_2O and CH_2Cl_2. The crude product was purified using column chromatography on silica gel by eluting with CH_2Cl_2 and n-hexane (CH_2Cl_2: n-hexane = 1:1 v/v) and preparative HPLC to give **1** with a yield of 63%. ^{1}H NMR ($CDCl_3$, 400.13 MHz): δ (ppm) = 7.90-7.96 (m, 8H, Ar*H*), 7.67 (d, *J* = 7.6 Hz, 2H, Ar*H*), 2.06-2.10 (m, 4H, Ar-C*H*$_2$-), 0.86-1.12 (m, 16H, -C*H*$_2$-), 0.76 (t, *J* = 7.2 Hz, 6H, -C*H*$_3$). ^{13}C NMR ($CDCl_3$, 100.61 MHz): δ (ppm) = 154.2, 153.4, 151.8, 141.1, 135.7, 134.5, 132.3, 128.3, 128.1, 124.0, 120.2, 112.9, 55.5, 40.2, 31.5, 30.0, 24.0, 22.6, 14.1. MALDI-TOF-Ms: *m/z* = 761 (M+H), Calcd for $C_{37}H_{36}Br_2N_4S_2$.

2: 1 (0.3g, 0.39mmol) and 4-(diphenylamino)phenylboronic acid (0.095 g, 0.33 mmol) were dissolved in the mixed solvents of THF (5 ml), toluene (4 ml) and 2.0M K_2CO_3 aqueous solution (3ml) under N_2. $Pd(PPh_3)_4$ (2 mg, 1.7μmol) was added to this solution and refluxed for 48 hr under N_2. The reaction mixture was poured into a mixture of H_2O and CH_2Cl_2. The crude product was purified using column chromatography on silica gel by eluting with CH_2Cl_2 and n-hexane (CH_2Cl_2: n-hexane = 1:1 v/v) and preparative HPLC to give **2** with a yield of 53%. ^{1}H NMR ($CDCl_3$, 400.13 MHz): δ (ppm) = 7.93-8.04 (m, 9H, Ar*H*), 7.83 (2H, d, *J* = 7.6 Hz, Ar*H*), 7.67 (d, *J* = 7.6 Hz, 1H, Ar*H*), 7.30 (t, *J* = 7.2Hz, 4H, Ar*H*), 7.22 (t, *J* = 7.2 Hz, 6H, Ar*H*), 7.07 (t, *J* = 7.2 Hz, 2H, Ar*H*), 2.06-2.10 (m, 4H, Ar-C*H*$_2$-), 0.88-1.14 (m, 16H, -C*H*$_2$-), 0.77 (t, *J* = 7.2 Hz, 6H, -C*H*$_3$). ^{13}C NMR ($CDCl_3$, 100.61 MHz): δ (ppm) = 154.2, 153.4, 151.8, 142.4, 141.6, 140.5, 135.7, 134.5, 132.8, 131.0, 129.4, 128.7, 128.3, 124.4, 122.9, 122.0, 121.5, 112.9, 55.5, 40.2, 31.5, 30.5, 25.1, 22.6, 14.0. MALDI-TOF-Ms: *m/z* = 925 (M+H), Calcd for $C_{55}H_{50}BrN_5S_2$.

3: 1 (0.32g, 0.42mmol) and 4,4'-dimetoxydiphenylamine (0.074g, 0.32mmol), sodium *tert*-butoxide (0.062g, 0.65mmol) were dissolved in dry toluene (5 ml) and refluxed for 30 min under N_2. Palladium (II) acetate (3.6mg, 16.2 μmol) and tri-*tert*-butylphosphine (10.0 μl) were added to this solution and heated at 100 ˚C under N_2. The reaction mixture was poured into a mixture of H_2O and CH_2Cl_2. The crude product was purified using column chromatography on silica gel by eluting with CH_2Cl_2 and n-hexane (CH_2Cl_2: n-hexane = 2:1 v/v) and preparative HPLC to give **2** with a yield of 16%. ^{1}H NMR ($CDCl_3$, 400.13 MHz): δ (ppm) = 7.93-7.98 (m, 7H, Ar*H*), 7.65 (t, *J* = 6.8 Hz, 2H, Ar*H*), 7.09 (d, *J* = 7.6 Hz, 1H, Ar*H*), 7.05-7.08 (m, 4H, Ar*H*), 6.79-6.89 (m, 4H, Ar*H*), 3.81 (s, 6H, -OCH_3), 2.08 (t, *J* = 8.0 Hz, 4H, Ar-CH_2-), 0.88-1.14 (m, 16H, -C*H*2-), 0.76 (t, *J* = 7.2 Hz, 6H, -CH_3). ^{13}C NMR ($CDCl_3$, 100.61 MHz): δ (ppm) = 156.4, 154.2, 153.4, 151.8, 148.7, 142.4, 136.0, 135.4, 133.9, 133.6, 132.8, 130.1, 129.1, 128.7, 128.3, 127.8, 124.1, 122.5, 115.1, 58.0, 55.5, 40.2, 31.5, 30.5, 25.1, 22.6, 14.0. MALDI-TOF-Ms: *m/z* = 909 (M+H), Calcd for $C_{51}H_{50}BrN_5S_2O_2$.

4: 2 (0.1g, 0.10 mmol) and 4-ethoxycarbony phenylboronic acid (0.032 g, 0.16 mmol) were dissolved in the mixed solvents of THF (5 ml), toluene (4 ml) and 2.0M K_2CO_3 aqueous solution (3ml) under N_2. $Pd(PPh_3)_4$ (2 mg, 1.7μmol) was added to this solution and refluxed for 48 hr under N_2. The reaction mixture was poured into a mixture of H_2O and CH_2Cl_2. The crude product was purified using column chromatography on silica gel by eluting with CH_2Cl_2 and n- hexane (CH_2Cl_2: n-hexane = 1:1 v/v) and preparative HPLC to give **2** with a yield of 77%. FT-IR (ATR): 1734 cm^{-1} (-COOR). ^{1}H NMR ($CDCl_3$, 400.13 MHz): δ (ppm) = 8.23 (d, *J* = 8.4 Hz, 2H, Ar*H*), 7.99-8.05 (m, 6H, Ar*H*), 7.88-7.95 (m, 7H, Ar*H*), 7.80 (d, *J* = 7.6 Hz, 2H, Ar*H*), 7.31 (t, *J* = 7.6Hz, 4H, Ar*H*), 7.20-7.25 (m, 6H, Ar*H*), 7.07 (t, *J* = 7.6Hz, 2H, Ar*H*), 4.40 (q, *J* = 7.2 Hz, 2H, -OCH_2CH$_3$), 2.06-2.13 (m, 4H, Ar-CH_2-), 1.44 (t, *J* = 6.8 Hz, 3H, -OCH$_2$CH_3), 0.90-1.15 (m, 16H, -CH_2-), 0.77 (t, *J* = 7.2 Hz, 6H, -CH_3). ^{13}C NMR ($CDCl_3$, 100.61 MHz): δ (ppm) = 167.0, 154.2, 142.4, 141.6, 141.0, 140.5, 136.0, 135.4, 131.0, 130.1, 129.4, 128.7, 128.3, 127.8, 127.3, 125.2,

122.9, 122.0, 121.5, 59.1, 55.5, 42.9, 32.5, 30.5, 25.1, 22.6, 14.0, 13.6. MALDI-TOF-Ms: *m/z* = 994 (M+H), Calcd for $C_{64}H_{59}N_5O_2S_2$.

5: 5 was synthesized from **2** and 4-formyl phenylboronic acid according to the same procedure of **4** (Yield 97%). FT-IR (ATR): 1697 cm^{-1} (-CHO). ^1H NMR ($CDCl_3$, 400.13 MHz): δ (ppm) = 10.13 (s, 1H, -C*H*O), 8.20 (d, *J* = 8.4 Hz, 2H, Ar*H*), 7.95-8.07 (m, 6H, Ar*H*), 7.90-7.96 (m, 6H, Ar*H*), 7.88 (d, *J* = 7.2 Hz, 1H, Ar*H*), 7.81 (d, *J* = 7.2 Hz, 1H, Ar*H*), 7.28-7.33 (m, 4H, Ar*H*), 7.18-7.22 (m, 6H, Ar*H*), 7.08 (t, *J* = 7.2 Hz, 2H, Ar*H*), 2.08-2.13 (m, 4H, Ar-CH_2-), 0.88-1.14 (m, 16H, -CH_2-), 0.77 (t, *J* = 7.2 Hz, 6H, -CH_3). ^{13}C NMR ($CDCl_3$, 100.61 MHz): δ (ppm) = 187.0, 154.2, 142.4, 141.6, 141.0, 140.5, 136.1, 135.5, 131.0, 130.2, 129.4, 128.7, 128.3, 127.8, 127.3, 125.2, 122.9, 122.0, 121.5, 55.5, 42.9, 32.5, 30.5, 25.1, 22.6, 14.0. MALDI-TOF- Ms: *m/z* = 950 (M+H), Calcd for $C_{62}H_{55}N_5OS_2$.

6: 6 was synthesized from **2** and 4-formyl phenylboronic acid according to the same procedure of **4** (Yield 97%). FT-IR (ATR): 1698 cm^{-1} (-CHO). ^1H NMR ($CDCl_3$, 400.13 MHz): δ (ppm) = 10.12 (s, 1H, -C*H*O), 8.19 (d, *J* = 8.0 Hz, 2H, Ar*H*), 7.90-7.98 (m, 10H, Ar*H*), 7.65 (d, *J* = 8.0 Hz, 1H, Ar*H*), 7.10 (d, *J* = 7.6Hz, 1H, Ar*H*), 7.00-7.08 (m, 4H, Ar*H*), 6.80-6.91 (m, 4H, Ar*H*), 3.81 (s, 6H, -OCH_3), 2.06-2.10 (m, 4H, Ar-CH_2-), 0.88-1.15 (m, 16H, -CH_2-), 0.76 (t, *J* = 7.2 Hz, 6H, -CH_3). ^{13}C NMR ($CDCl_3$, 100.61 MHz): δ (ppm) =188.0, 156.4, 154.2, 153.4, 148.7, 142.4, 136.0, 135.6, 135.4, 133.9, 133.6, 130.1, 128.7, 128.3, 127.8, 125.4, 124.1, 122.5, 115.5, 58.0, 55.5, 42.9, 32.5, 30.5, 25.1, 22.6, 14.0. MALDI-TOF-Ms: *m/z* = 933 (M+H), Calcd for $C_{58}H_{55}N_5O_3S_2$.

MR-1: An aqueous solution of NaOH (3.0 M, 0.5 ml) was added to the solution of **4** (83 mg, 83.5 μmol) in THF (2 ml). The mixture was stirred at 70 ˚C for 24 hr. The solvent was removed in vacuo and the residue was dissolved in methanol (3 ml) and THF (3ml). The mixture was refluxed for 2 hr. The resulting solution was filtered and neutralized with acetic acid. The precipitate was collected by filtration, washed with water, and dried in vacuo (Yield 92%). FT-IR (ATR): 1716 cm-1 (-COOH). ^1H NMR ($CDCl_3$, 400.13 MHz): δ (ppm) = 8.23 (d, *J* = 8.4 Hz, 2H, Ar*H*), 7.99-8.05 (m, 6H,

Ar*H*), 7.88-7.95 (m, 7H, Ar*H*), 7.80 (d, *J* = 7.6 Hz, 2H, Ar*H*), 7.31 (t, *J* = 7.6Hz, 4H, Ar*H*), 7.20-7.25 (m, 6H, Ar*H*), 7.07 (t, *J* = 7.6Hz, 2H, Ar*H*), 2.06-2.13 (m, 4H, Ar-CH_2-), 0.90-1.15 (m, 16H, -CH_2-), 0.77 (t, *J* = 7.2 Hz, 6H, -CH_3). ^{13}C NMR ($CDCl_3$, 100.61 MHz): δ (ppm) = 172.0, 154.6, 142.4, 141.7, 141.3, 140.5, 136.0, 135.4, 131.0, 130.5, 129.5, 128.6, 128.4, 127.8, 127.3, 125.2, 122.9, 122.0, 121.5, 45.5, 42.9, 32.5, 30.5, 25.1, 23.0, 14.0. MALDI-TOF-Ms: *m/z* = 994 (M+H), Calcd for $C_{64}H_{59}N_5O_2S_2$. Anal. Calcd for $C_{62}H_{55}N_5O_2S_2$: C, 77.07; H, 5.74; N, 7.25. Found: C, 77.0; H, 5.6; N, 7.3. Calcd for $C_{62}H_{55}N_5O_2S_2$. Purity (HPLC) > 98%.

MR-2: A 1 ml acetonitrile solution of **5** (80 mg, 84.2 μmol), cyanoacetic acid (14 mg, 0.17 mmol) and piperidine (0.5 ml) was refluxed for 8 hr under N_2. The reaction mixture was poured into a mixture of H_2O and CH_2Cl_2 and the organic phase was washed with 0.1M HCl aqueous solution and water. The organic phase was collected and dried with $MgSO_4$. The crude product was purified using column chromatography on silica gel by eluting with CH_2Cl_2 and methanol (CH_2Cl_2 : methanol = 10 : 1 v/v) to give **MR-2** with a yield of 82%. FT-IR (ATR): 2231 (-CN) and 1708 (-COOH) cm^{-1}. ^{1}H NMR ($CDCl_3$, 400.13 MHz): δ (ppm) = 8.20 (d, *J* = 8.4 Hz, 2H, Ar*H*), 7.95-8.07 (m, 6H, Ar*H*), 7.90-7.96 (m, 6H, Ar*H*), 7.88 (d, *J* = 7.2Hz, 1H, Ar*H*), 7.81 (d, *J* = 7.2 Hz, 1H, Ar*H*), 7.28-7.33 (m, 4H, Ar*H*), 7.18-7.22 (m, 6H, Ar*H*), 7.08 (t, *J* = 7.2Hz, 2H, Ar*H*), 2.08-2.13 (m, 4H, Ar-CH_2-), 0.88-1.14 (m, 16H, -CH_2-), 0.77 (t, *J* = 7.2 Hz, 6H, -CH_3). ^{13}C NMR ($CDCl_3$, 100.61 MHz): δ (ppm) = 170.0, 159.8, 154.6, 142.4, 141.6, 140.5, 136.1, 135.8, 135.4, 133.8, 131.0, 130.2, 129.4, 128.7, 128.3, 127.8, 127.3, 126.7, 125.3, 122.9, 122.0, 121.5, 117.2, 99.8, 45.5, 42.9, 32.5, 30.5, 25.1, 22.6, 14.0. MALDI-TOF-Ms: *m/z* = 1018 (M+H), Calcd for $C_{65}H_{56}N_6O_2S_2$. Anal. Calcd for $C_{62}H_{55}N_5O_2S_2$: C, 76.74; H, 5.55; N, 8.26. Found: C, 76.5; H, 5.5; N, 8.2. Purity (HPLC) > 99%.

MR-3: MR-3 was synthesized from **6** and cyanoacetic acid by the same procedure of **MR-2** (Yield 54 %). FT-IR (ATR): 2231 (-CN) and 1708 (-COOH) cm^{-1}. ^{1}H NMR ($CDCl_3$, 400.13 MHz): δ (ppm) = 8.19 (d, *J* = 8.0 Hz, 2H, Ar*H*), 7.90-7.98 (m, 10H, Ar*H*), 7.65 (d, *J* = 8.0 Hz, 1H, Ar*H*), 7.10 (d, *J* = 7.6Hz, 1H, Ar*H*), 7.00-7.08 (m, 4H,

Ar*H*), 6.80-6.91 (m, 4H, Ar*H*), 3.81 (s, 6H, -OC*H*$_3$), 2.06-2.10 (m, 4H, Ar-C*H*$_2$-), 0.88-1.15 (m, 16H, -C*H*$_2$-), 0.76 (t, *J* = 7.2 Hz, 6H, -C*H*$_3$). ^{13}C NMR ($CDCl_3$, 100.61Hz): δ (ppm) = 170.1, 159.8, 156.4, 155.0, 154.5, 148.7, 142.4, 136.0, 135.7, 135.4, 133.9, 133.8, 133.6, 128.8, 128.4, 127.3, 126.7, 125.4, 124.1, 122.5, 117.2, 115.5, 99.8, 56.0, 45.5, 42.9, 32.5, 30.5, 25.1, 22.6, 14.0. MALDI-TOF-Ms: *m/z* = 1000 (M+H), Calcd for $C_{61}H_{56}N_6O_4S_2$. Anal. Calcd for $C_{62}H_{55}N_5O_2S_2$: C, 73.17; H, 5.64; N, 8.39. Found: C, 73.2; H, 5.6; N, 8.3. Purity (HPLC) > 98%.

5-5 References

1. B. O'Regan, M. Grätzel, *Nature*, **1991**, 353, 737.
2. A. Hagfeldt, G. Boschloo, L. Sun, L. Kloo, H. Pettersson, *Chem,. Rev*., **2010**, 110, 6595.
3. Y. Chiba, A. Islam, Y. Watanabe, R. Komiya, N. Koide, L. Han, *Jpn. J. Appl. Phys*., **2006**, 45, L638.
4. N. Robertson, *Angew. Chem. Int. Ed*., **2006**, 45, 2328.
5. K. Hara, T. Horihuchi, T. Kinoshita, K. Sayama, H. Arakawa, *Sol. Energy Mater. Sol. Cells*, **2001**, 70, 151.
6. A. Mishra, M. K. R. Fischer, P. Bäuerle, *Angew. Chem., Int. Ed.*, **2009**, 48, 2474.
7. G. Zhou, N. Pschier, J. C. Schöneboom, F. Erickmeyer, M. Baumgarten, K. Müllen, *Chem. Mater*., **2008**, 20, 1808.
8. C. L. Donley, J. Zaumseil, J. W. Andreasen, M. M. Nielsen, H. Sirringhaus, R. H. Friend, J.-S. Kim, L. Lu, P. Sreearunothai, A. Seeley, K.-H. Yim, A. Petrozza, C. E. Murphy, D. Beljonne, J. Cornil, R. H. Friend, *J. Am. Chem. Soc*., **2008**, 130, 13120; P.-L. T. Boudreault, A. Najari, M. Leclerc, *Chem. Mater*., **2011**, 23, 456.
9. P. M. Beaujuge, H. N. Tsao, M. R. Hansen, C. M. Amb, C. Eisko, J. Subbish, K. R. Choudhury, A. Mavrinskiy, W. Pisula, J.-L. Bredas, F. So, K. Müllen, J. R. Reynolds, *J. Am. Chem. Soc*., **2012**, 134, 8404.
10. M. Velusamy, K. R. J. Thomas, J. T. Lin, Y.-C. Hsu, K.-C. Ho, *Org. Lett*., 2005, 7, 1899; H.-H. Chou, Y.-C. Chen, H.-J. Huang, T.-H. Lee, J. T. Lin, C. Tsai, K. Chen, *J. Mater. Chem*., **2012**, 22, 10929.
11. L.-Y. Lin, Y. H. Chen, Z.-H. Chen, Z.-Y. Huang, H.-W. Lin, S.-H. Chou, F. Lin, C.-W. Chen, Y.-H. Liu, K.-T. Wong, *J. Am. Chem. Soc*., **2011**, 133, 15822.
12. F. Paul, J. Patt, J. F. Hartwig, *J. Am. Chem. Soc*., **1994**, 116, 5669.

13. J.-I. Nishida, T. Masuko, Y. Cui, K. Hara, H. Shibuya, M. Ihara, T. Hosoyama, R. Goto, S. Mori, Y. Yamashita, *J. Phys. Chem. C*, **2010**, 114, 17920.
14. D. P. Hagberg, J.-H. Yum, H. Lee, F. De Angelis, T. Marinado, K. M. Karlsson, R. Humphry-Baker, L. Sun, A. Hagfeldt, M. Grätzel, M. K. Nazeeruddin, *J. Am. Chem. Soc*., **2008**, 130, 6259.

Chapter 6

Summary and Conclusions

Since the first report of the conductive polymers, a number of organic semiconductors have been created from polymer to small molecules. Because of their unique structural and optical properties, small molecule-based organic semiconductors are promising candidates for optoelectronic devices such as OFETs, OLEDs, and OSCs. For enhancement of these device performances, organic semiconductor requires some properties such as high charge carrier mobility and excellent absorption properties. In this thesis, the author has investigated structure–property relationship between a series of organic semiconductors and OSCs properties.

This chapter highlights the topics obtained from the development of the organic semiconductors for OSCs. The disk-shaped molecules such as pyrene, triphenylene, and hexabenzocoronene are promissing building block for the organic semiconductors. A self-assembled 1D columnar structure of the disk-shaped molecules exhibited the high carrier mobilities. The variety of the substitution site of the pyrene that is four fused benzene rings are favorable for the tuning optical and electrochemical properties. In this thesis, the author has designed and synthesized pyrene-cored disk-shaped organic semiconductors for BHJ solar cells (**Chapter 2-4**). Metal-free organic dyes for DSSCs have been attracted the attentions due to low-cost and easily tuning their energy levels easily. The π-bridge of the organic dyes is important for the charge carrier transportation after the photoexitation. Benzothiadiazole-fulorene unit was used as the carrier transportation unit in the polymeric semiconductors in OLEDs. The author has designed and synthesized novel organic dyes having benzothidiazole-fluorene unit (**Chapter 5**).

Chapter 2 deals with the synthesis and investigation of BHJ solar cell properties of the disk-shaped molecules having pyrene core and oligothiophene side chains. It was found that the lowest unoccupied molecular orbital (LUMO) energy levels of the synthesized molecules were ideal for achieving efficient electron transfer to fullerene derivatives $PC_{61}BM$ and $PC_{71}BM$, and that the disk-shaped molecules can function as electron donor components in solution-processed BHJ solar cells. Disk-shaped molecules organized ordered structures through intermolecular π–π interactions as monitored by temperature-controlled polarized optical microscope (TPOM), differential scanning calorimetry (DSC), and powder X-ray diffraction (XRD). Solution-processed BHJ solar cells using disk-shaped donor and fullerene derivatives as acceptor materials were fabricated and investigated. The oligothiophene lengths were reflected in the performance characteristics of solar cell devices fabricated using disk-shaped donors. A 2.6% of Power conversion efficiency (PCE) was achieved for small-molecule BHJ solar cells containing self-organized crystals of disk-shaped molecules in the active layer under one sun condition.

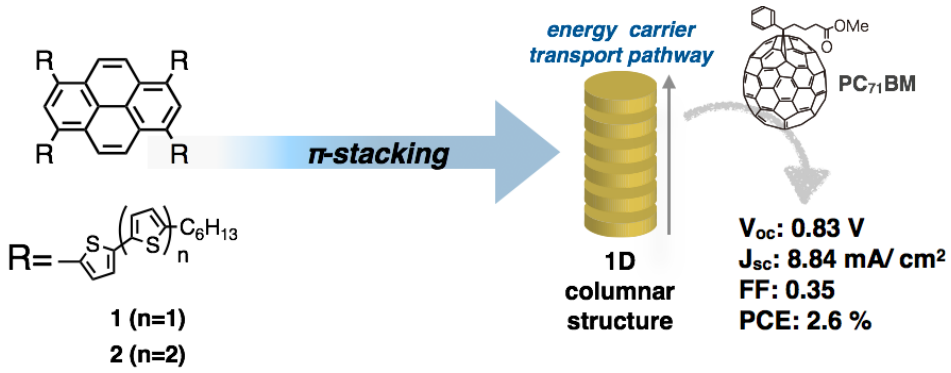

Chart 1.

Chapter 3 described low band gap disk-shaped donors having acceptor terminal unit. Disk-shaped donors composed of a pyrene core, dithiophene linkers and rhodanine terminates were synthesized. The introduction of rhodanine terminal units into the pyrene-cored donors could effectively broaden the absorption spectrum and improve the molar absorption coefficient. The positions of dithiophene linkers in the pyrene core affected to their optical and electrochemical properties as well as the

molecular ordering and carrier transport properties in solid state. In addition, length of peripheral alkyl chains in dithiophene linkers changed molecular ordering and carrier transport properties in solid state. The HOMO and LUMO energy levels of these materials were suitable for the donor component in BHJ solar cells with fullerene acceptor. The BHJ solar cells were fabricated by the solution process using mixed solutions of pyrene-cored donors with fullerene acceptors. The PCE values strongly depended on the structure of the donor. In addition, the shortening of the peripheral alkyl chain length in the dithiophene linkers improved the PCE due to its better hole-mobility in the film. The highest PCE was achieved 3.7% of an overall power conversion efficiency with 8.4mA/cm^2 of short-circuit current density, 1.09V of open-circuit voltage, and 41% of fill factor under one sun condition.

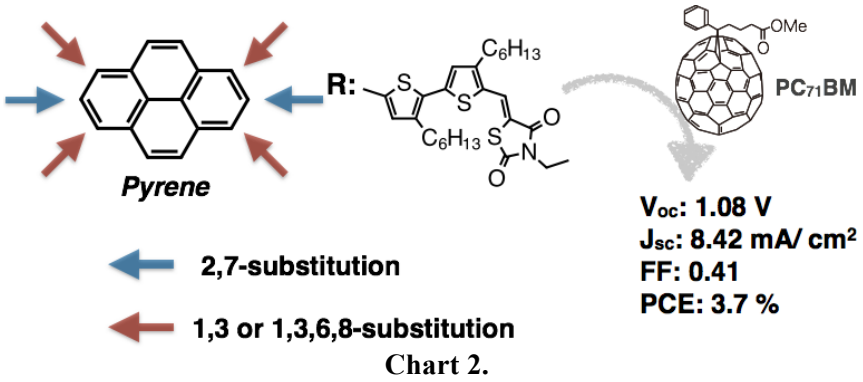

Chart 2.

In **chapter 4**, non-fullerene BHJ solar cells based on two disk-shaped molecules were fabricated and investigated their properties. Perylene diimide (PDI) derivatives were used as electron donor component in solution-processed BHJ solar cells. The introduction of the thiophene in the bay position of PDI can be tuned their optical and redox properties as well as molecular ordering in the solid state. The HOMO and LUMO energy levels of the PDI derivatives are suitable for the energy transfer to the disk-shaped donor. The BHJ solar cells were fabricated by solution process using mixed solution of disk-shaped donor and PDI derivatives as acceptor. The performances of BHJ solar cells were influenced by the molecular structure of PDI derivatives. Optimizations of the nano-structure in blended film by adding 1,8-diiodeoctane have greatly improved the PCE of BHJ solar cells. The highest PCE

of two disk-shaped donor and acceptor based BHJ solar cell was achieved 0.7% of PCE with V_{oc} of over 1V under one sun condition.

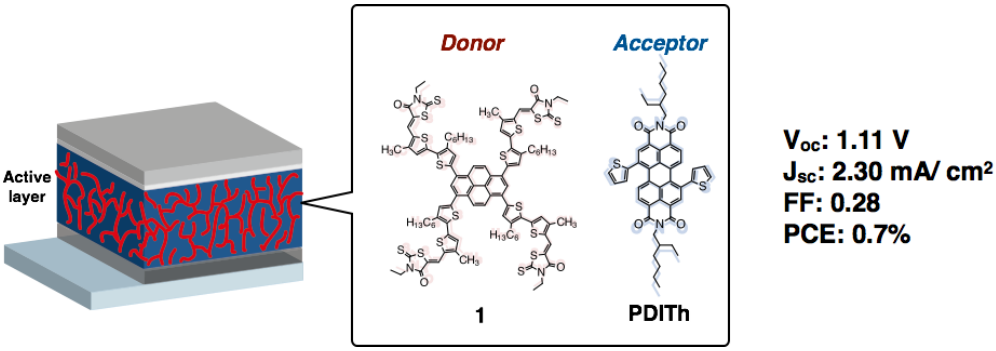

Chart 3.

Chapter 5 described development of organic dyes containing fluorene-benzothiadiazole unit for DSSCs sensitizers (Chart 4). The introduction of different electron donating and electron accepting unit into the fluorene-benzothiadiazole bridge was achieved the tuning optical and electrochemical properties. DFT calculations of **MR-2** and **MR-3** showed completely separated the HOMO and LUMO electron density distributions. The DSSCs using **MR-3** exhibited 4.0% of PCE. **MR-3** cells have a high V_{oc} and FF compared with those of rhuthenium sensitizer (N719).

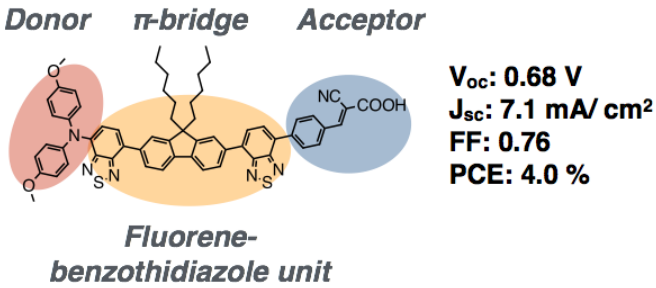

Chart 4.

In this thesis, structure–property relationship of small molecule organic semiconductors for OSCs were disclosed. The disk-shaped molecules are suitable for the central core of the donor materials in BHJ solar cells. Introducing of the functional side chain into the core influenced to their optical and electrochemical properties as

well as molecular ordering in solid state. The performance of the BHJ solar cells was achieved 3.7% of PCE with high V_{oc} of over 1V. The DSSCs sensitizer containing fluorene-benzothidiazole unit can tune optical and electrochemical properties by introducing electron donating and accepting units. The performance of the DSSCs was achieved 4.0% of PCE with high V_{oc} compared with ruthenium complex. However, toward the high performance OSCs of small molecule organic semiconductors, some challenges requires further enhancing both hole and electron mobilities, broader absorption properties, and better controlling the molecular packing, which call for the integrated consideration of both molecular and process engineering.

List of publication

Papers

1. Mutsumi Kimura, Masayoshi Karasawa, Naoki Sasagawa, Keisuke Takemoto, Ryota Goto and Shogo Mori, **Organic Sensitizers Including π-Conjugated Fluorene-benzothiadiazole Bridge for Dye-sensitized Solar Cells**, *Chemistry Letters*, **2012**, 41, 1613-1615.

2. Keisuke Takemoto, Masayoshi Karasawa, and Mutsumi Kimura, **Solution-Processed Bulk-Heterojunction Solar Cells containing Self-Organized Disk-Shaped Donors,** *ACS Appl. Mater. Interfaces*, **2012**, 4, 6289-6294.

3. Keisuke Takemoto and Mutsumi Kimura, **Low Band Gap Disk-shaped Donors for Solution-Processed Organic Solar Cells**, *RSC Advances*, **2014**, 4, 64589-64595.

4. Keisuke Takemoto and Mutsumi Kimura, **Small molecule Bulk-Heterojunction Solar Cells Composed of Two Discrete Organic Semiconductors**, *Chemistry Letters*, **2015**, 44, 315-371.

Presentations on international symposium

1. Keisuke Takemoto and Mutsumi Kimura, **Bulk-heterojunction Solar Cells composed of Semiconductive Disk-like Molecules**, IUMRS-International Conference on Electronic Materials 2012, Yokohama (Japan), September 2012.

2. Keisuke Takemoto and Mutsumi Kimura, **Bulk heterojunction solar cells using Disk-shaped donor having oligothiophene side chain**, HYBRID AND ORGANIC PHOTOVOLTAICS CONFERENCE (HOPV 2013), Seville (Spain), May 2013.

3. Keisuke Takemoto and Mutsumi Kimura, **Star-shaped donor materials for the solution-processed bulk-hetrojunction solar cells**, 2013 MRS Fall Meeting & Exhibit, Boston (USA), December 2013.

4. Keisuke Takemoto and Mutsumi Kimura, **Bulk-Heterojunction Solar Cells composed of Pyrene-cored Donors**, International Symposium on Fiber Science and Technology 2014 (ISF 2014), 2014, Tokyo (Japan), September 2014.

Presentations on Symposium

1. Keisuke Takemoto, Mutsumi Kimura and Hirohusa Shirai, **Fabrication of organic solar cells using disk-like molecules having oligothiophene side chain**, 90th Annual Meeting of Chemical Society of Japan, Osaka (Japan), March 2010.

2. Keisuke Takemoto, Mutsumi Kimura and Hirohusa Shirai, **Control of Self-assembled Structures made of Disk-like molecules bearing Conjugated Oligomers**, 59th SPSJ Annual Meeting, Kanagawa (Japan), May 2010.

3. Keisuke Takemoto, Tadashi Fukawa, Mutsumi Kimura and Hirohusa Shirai, **Bulk Hetero junction solar cells composed of self-organized columnar assemblies of disk-like molecules bearing conjugated oligomers**, 59th SPSJ Symposium on Macromolecules, Hokkaido (Japan), September 2010.

4. Keisuke Takemoto, Tadashi Fukawa, Mutsumi Kimura and Hirohusa Shirai, **Bulk heterojunction solar cells composed of disk-like molecules bearing peripheral oligothiophenes**, The Electrochemical Society of Japan 2010 Fall Meeting, Kanagawa (Japan), September 2010.

5. Keisuke Takemoto, Tadashi Fukawa, Mutsumi Kimura and Hirohusa Shirai, **Bulk heterojunction solar cells containing self-organized structures made of Disk-like molecules bearing conjugated side chain**, 91st Annual Meeting of Chemical Society of Japan, Kanagawa (Japan), March 2011.

6. Keisuke Takemoto, Tadashi Fukawa, Mutsumi Kimura and Hirohusa Shirai, **Bulk Heterojunction Solar Cells including Columnar Assemblies of Disk-like Molecules**, 60th SPSJ Annual Meeting, Osaka (Japan), May 2011.

7. Keisuke Takemoto, Tadashi Fukawa, Mutsumi Kimura and Hirohusa Shirai, **Bulk Heterojunction solar cells using self-organized columnar structure made of organic semiconductors**, 60th SPSJ Symposium on Macromolecules, Okayama (Japan), September 2011.

8. Keisuke Takemoto and Mutsumi Kimura, **Bulk heterojunction solar cells based one-dimenyonal columnar assemblies of Disk-like molecules**, 3rd Annual Meeting of the Nanofiber Society, Miyagi (Japan), October 2012.

9. Keisuke Takemoto and Mutsumi Kimura, **Bulk-heterojunction solar cells composed of disk-like molecules having oligo(thiophene) side chains**, 93rd Annual Meeting of Chemical Society of Japan, Shiga (Japan), March 2013.

10. Keisuke Takemoto and Mutsumi Kimura, **Star-shaped organic semiconductor for high performance Bulk-heterojunction solar cells**, The 62nd SPSJ Symposium on Macromolecules, Ishikawa (Japan), September 2013.

11. Keisuke Takemoto and Mutsumi Kimura, **Small molecule based Bulk-heterojunction solar cells using star-shaped organic semiconductor**, The 74th JSAP Autumn Meeting, Kyoto (Japan), September 2013.

12. Keisuke Takemoto and Mutsumi Kimura, **Pyrene cored organic semiconductors for solution processed bulk-heterojunction solar cells**, 94th Annual Meeting of Chemical Society of Japan, 2014, Nagoya (Japan), March 2014.

13. Keisuke Takemoto and Mutsumi Kimura, **Bulk-heterojunction Solar Cells Composed of Disk-shaped molecules having functional side chains**, 95th Annual Meeting of Chemical Society of Japan, 2015, Chiba (Japan), March 2015.

Award

1. Keisuke Takemoto received Chemical Society of Japan Student Presentation Award 2013 at 93rd Annual Meeting of Chemical Society of Japan.

Acknowledgement

Firstly and most importantly, I would like to express my deepest gratitude to my supervisor, Prof. Mutsumi Kimura, for his limitless patience, understanding and honest support. Without his guidance and persistent help this dissertation would not have been possible.

Prof. Shogo Mori gives me constructive comments and warm encouragement. Also I would like to extend my special thanks to Prof. Genichi Konishi of Tokyo Institute of Technology, Prof. Kazuchika Ohta, Prof. Yoshinori Nishii for reviewing my thesis. I would like to express great appreciation to Prof. Minoru Taya in University of Washington for giving me a chance to study abroad in the United States.

Advice and comments given by Dr. Takahiro Kono and Mr. Tadashi Fukawa have been a great help in my research. I am particularly grateful for the assistance given by Dr. Yoshie Shinohara, Ms. Junko Takizawa, Seiko Uda and Misato Takahashi. Many thanks to former member of Mr. Ryosuke Sakai, Shigenori Kamada, Kazumasa Yasuta, Satoshi Ohtsuji, Masayoshi Karawasa and Ms. Mei Yokokawa for their suggestions and advises. I would also like to thank Mr. Hiroyuki Suzuki, Junya Masuo, Satoshi Yamamoto, and other members of Kimura Lab. for the help and moral support.

Finally, I would like to express my gratitude to my family for their moral support and warm encouragements.

March 2015

Keisuke Takemoto